Cosmic Dust Detection by Antenna Instruments - Modeling and Laboratory Measurements

by

Ming-Hsueh (Mitchell) Shen

B.S., National Cheng Kung University, 2014

M.S., National Cheng Kung University, 2017

A thesis submitted to the

Faculty of the Graduate School of the

University of Colorado in partial fulfillment

of the requirements for the degree of

Doctor of Philosophy

Department of Aerospace Engineering Sciences

2021

Committee Members:
Zoltán Sternovsky
Mihály Horányi
David Malaspina
Robert Marshall
Scott Palo

Shen, Ming-Hsueh (Mitchell) (Ph.D., Aerospace Engineering Sciences)

Cosmic Dust Detection by Antenna Instruments -

Modeling and Laboratory Measurements

Thesis directed by Prof. Zoltán Sternovsky

Dust impacts on spacecraft are commonly detected by antenna instruments as transient voltage perturbations. The signal waveform is generated by the interaction between the impact-generated plasma cloud and the elements of the antenna – spacecraft system. A general electrostatic model is presented that includes the two key elements of the interaction, namely the charge recollected from the impact plasma by the spacecraft and the fraction of electrons and cations that escape to infinity. The clouds of escaping electrons and cations generate induced signals, and their vastly different escape speeds are responsible for the characteristic shape of the waveforms. The induced signals are modeled numerically for the geometry of the system and the location of the impact. The model employs a Maxwell capacitance matrix to keep track of the mutual interaction between the elements of the system. Two reduced-size model spacecraft are constructed for laboratory measurements using the dust accelerator facility. Each model spacecraft is equipped with multiple antennas, simultaneously operating in monopole and dipole modes. Submicron-sized dust particles are accelerated to hyperspeed and are used for test measurements, where the waveforms of each antenna are recorded. The electrostatic model provides a remarkably good fit to the data using only a handful of physical fitting parameters, such as the escape speeds of electrons and cations. The presented general model provides the framework for analyzing antenna waveforms and is applicable for a range of space missions investigating the distribution of dust particles in relevant environments.

Dedication

I dedicate this thesis to my parents 沈展源 and 温慧英, who always support me, and Leonard Nimoy (1931-2015), giving me a role model for becoming a scientist like Spock.

Acknowledgements

Time flies, three years have passed. It is a journey full of twists and turns but turns out to be a bowl of cherries. First of all, I'd like to thank my advisor, Zoltán Sternovsky, for his patience and guidance throughout my doctoral studies. I'd like to thank David Malaspina for brainstorming with me. I'd like to thank Bill Goode, who supported me through thick and thin in the face of adversity. Thanks to Sean Hsu for always discussing new ideas. My appreciation goes to Mihály Horányi for his suggestions in finding a postdoctoral position. For the introduction to the dust accelerator operation and supporting laboratory measurements, I'd like to thank John Fontanese and David James. I appreciate all my colleagues in the IMPACT dust lab and Alessandro Garzelli for his assistance while visiting our lab.

As for mentors in the Aerospace department, I appreciate Penny Axelrad, who advised me to think carefully, and act quickly. I'd like to thank Delores Knipp, Robert Marshall, and Scott Palo for their valuable discussions. In addition, I'm grateful for all the support of my mentors in Taiwan, Yei-Chin Chao, Charles Lin, Alfred Chen, Zic Li, and Loren Chang. Thanks, Matt Morley, for your effort correcting grammar and typos in this thesis. During the graduate student life, I'd like to thank Elise Su for her suggestions and contributions. And, thanks to Jamie Lin for her encouragement. Finally, I would like to sincerely thank my parents for raising me and appreciate all their selfless support. I love you both!

"Space, the final frontier. These are the voyages of the starship Mitchell Shen (沈明學). His three-year mission: to explore strange new worlds, to seek out new science and new conceptualizations, to boldly go where no man has gone before." Live long and prosper, dear friends.

Contents

Chapter

Tables

Table

Figures

Figure

Chapter 1

Introduction

1.1 Overview

Dust is abundant in our galaxy and solar system and it plays a vital role in their formation and evolution. The solar system resides in the Orion Arm of the Milky Way and travels through the Local Interstellar Cloud (LIC). Neutral gas molecules and dust particles larger than about 100 nm from the LIC can pass through the heliospheric boundary and start their journey across the solar system with an inflow direction (approximately 256° ecliptic longitude and +5° ecliptic latitude) and a characteristic speed of about 26 km/s. The micron and sub-micron sized interstellar dust (ISD) particles interact with the interplanetary magnetic field (Lorentz force), solar gravity, and radiation pressure. The flux and directionality of ISD grains are modulated by interactions with the interplanetary magnetic field periodically over the timescales of the solar cycle. Larger particles are delivered to Earth's orbit, where they can be detected and analyzed in situ. These ISD particles from the LIC are the closest representation of the building blocks that formed the solar system 4.5 billion years ago. Interplanetary dust particles (IDPs) bound to the solar system are continually generated, transported, and destroyed through a range of universal physical processes. Asteroids and comets are the primary sources that feed the interplanetary dust complex. The particles have a finite lifetime orbiting the Sun, as they slowly move inward due to the Poynting-Robertson drag. Mutual collisions, sputtering, and sublimation are the major loss processes of IDPs close to the Sun. These loss processes then locally generate atoms, molecules, nanometer-sized, and sub-micron sized dust particles. The former two become pickup ions and accelerate

outward by interacting with the solar wind (SW) magnetic field. There is a relatively narrow size range of sub-micron sized particles that become β-meteoroids; i.e., particles that are accelerated outward due to solar radiation pressure dominating over gravity. On smaller scales, dust particles exhibit interesting phenomena in some planetary systems (e.g., Saturn's E-ring) or can be actively or passively generated. Examples of the former are the volcanoes and cryo-volcanoes on Io and Enceladus, respectively. Airless bodies, such as moons and asteroids, eject dust particles due to the continual bombardment of their surfaces by IDPs and micrometeoroids. In summary, by detecting and analyzing dust particles, we can learn about the formation and evolution of the solar system, including the original and processed materials and the vast range of physical processes in action.

Before satellites, our understanding of cosmic dust was limited to optical observations. Interplanetary dust could be observed as the zodiacal light, for example. In situ dust detector instruments have been implemented from the very beginning of the space age. The Explorer 1 satellite carried an acoustic sensor for the detection of micrometeorite or cosmic dust impacts, for example (Dubin, 1960). Dust instruments have evolved significantly since then. They can be divided into two categories: Dust detectors typically measure the mass of individual particles and can be used to characterize the mass/size distributions of dust particles as well as determine the flux and directionality of the particles from the statistics of observations. On the other hand, dust analyzer instruments can also provide the composition of the dust particles using a physical phenomenon known as impact ionization. This thesis focuses only on dust detection.

Dedicated and well-calibrated dust instruments have been flown only on a handful of missions with interplanetary trajectories over the last decades (e.g., Galileo, Ulysses, Cassini). Heliophysics missions, however, often carry plasma wave instruments with antennas. It has been known that such instruments are sensitive to dust impacts ever since the Saturn flybys by the Voyager spacecraft. Dust detection by antennas is complementary to measurements by dedicated dust instruments, as they offer a much larger collection area (the full spacecraft surface), which makes it possible to characterize dust populations with lower fluxes. Antenna instruments thus often provide the only means of making dust measurements in previously unexplored environments (e.g., the FIELDS

instrument onboard the Parker Solar Probe mission). The utility of dust detection data by antenna instruments, however, has been limited due to the lack of detailed understandings of how dust impacts lead to the generation of measurable electrical signals. Specifically, the calculation of the mass of the impacting particle with useful certainty remained a difficult task. The impact of dust particles with speeds $\geq$ 1 km/s generate a small puff of plasma in a process known as impact ionization. It is the interaction of the impact plasma with spacecraft and the antenna that leads to the generation of measurable signals.

Recently, dust accelerators have enabled the study of the properties of dust impact plasmas and their interactions with antenna instruments in well-defined laboratory conditions. Collectively, these measurements lead to the understanding of (1) some key properties of dust impact plasmas and (2) the basic physical mechanism of how the voltage signal is generated on the antennas. The former includes the measurements of the impact charge yield for common spacecraft materials and the effective temperatures of the electrons and cations of the impact plasma. This thesis reports the development of the electrostatic antenna model based on first principles and provides a qualitative and quantitative understanding of the antenna waveforms recorded in laboratory conditions. The model is based on the different expansion speeds of electrons and ions during the expansion of the impact plasma cloud. The spacecraft floating potential determines the fraction of electrons and ions from the impact plasma that are collected by the spacecraft or are allowed to escape. A combination of the net collected charge and the induced charge from the escaping electron/ion populations is responsible for generating a voltage difference between the elements of the system. The charges are converted to voltages over the effective capacitance of the elements. Maxwell's capacitance matrix is employed in order to account for the coupling between the elements. The analytical model is also used to calculate the signal waveforms in realistic environments. These calculations indicate that the amplitudes of the impact signals can be significantly reduced due to discharging effects from the ambient plasma and mutual charging effects between elements due to their voltage differences. Recently, the model has been expanded to describe the antenna signals as a function of the dust impact location. Laboratory measurements reported that dust impacts occurring close

to one of the antennas register a larger signal amplitude than other antennas according to the induced charging. Hence, a geometry function has been introduced to describe the effect of charges escaping in space/time, thus inducing different voltage signals on different antennas. The validity of the electrostatic model is verified for laboratory dust impacts with ≥ 20 km/s. An experimental campaign has been carried out to investigate the effect of dust materials (iron versus aluminum), impact location, impact speed, and antenna mode of operation (monopole versus dipole).

The presented electrostatic model is intended to be used as the framework for the improved analysis of dust impact waveforms from a range of current and future missions. The fitting of the data by the model can provide the impact charge and the location of the impact on the spacecraft (SC). The impact charge is a measure of the dust particle's mass, and determining the impact location constrains the origin (and therefore velocity) of the dust particle. All prior studies used statistical guesses at the impact velocity and the origin of the particles and used simplified models for the capacitances of the spacecraft elements and their interactions.

The thesis is organized as follows. The next Section 1.2 provides a quick overview of the dust populations that can be observed in situ within the solar system, followed by the basic physical processes responsible for the evolution of the interplanetary dust complex. Instruments capable of detecting and analyzing dust particles and their history in prior missions are described in Section 1.3. Chapter 2 is an overview of antenna instruments, their characteristics, and operation principle. The impact ionization process is described in Chapter 3, along with its relevant properties for the work presented in this thesis. Chapter 4 presents the developed electrostatic model. The laboratory and measurement setup for validating the electrostatic model are presented in Chapter 5. Chapter 6 provides the details of the data analysis and interpretation. Finally, the summary and conclusions are provided in Chapter 7.

1.2 Dust in the Solar System

1.2.1 Dust Populations

Dust particles populating the interplanetary space can be identified based on their parent bodies and dynamical interactions that result in their orbital evolution. Interplanetary dust particles originate from the asteroid belt, Edgeworth-Kuiper objects, or comets (long-period Oort-cloud comets and Halley-type comets, as well as short-period Jupiter-family comets) (Poppe, 2016). In addition, a stream of interstellar particles passes through the solar system originating from the Local Interstellar Cloud (LIC) (Grün et al., 1993). On more localized scales, dust is present in planetary environments in the form of circumplanetary rings (e.g., Saturn), as populations of ejecta particles around airless bodies generated by the continual micrometeoroid bombardment of their surfaces (e.g., Moon, asteroids), or as the product of volcanic or cryovolcanic activity (e.g., Io, Enceladus) (Horányi, 1996, Burns et al., 2001, Szalay et al., 2018). The latter are the sources of high-speed, nanometer-sized dust particles, so-called "stream particles" accelerated to high velocities by electromagnetic forces and ejected from the Jovian or Saturnian systems (Grün et al., 1993, Kempf et al., 2005). Dust particles are continually generated and have finite lifetimes determined by gravitational force, solar radiation pressure, and electromagnetic forces. The processes taking place in the solar system are relevant to dust evolution in other planetary systems.

Interplanetary Dust Particles (IDPs) concentrated around the ecliptic plane can be observed with remote sensing techniques; for example, through the scattered sunlight known as the zodiacal light shown in Figure 1.1, as well as thermal infrared emission (Gustafson, 1994). IDPs are continuously supplied from the main asteroid belt ($\sim 2-4$ AU) and various comet populations. In the main asteroid belt, mutual collisions between objects and impact by meteoroids generate fragments with a broad size distribution. The estimated dust production rate from asteroids is on the order of 10^8 to 10^{10} kg/s (Mann et al., 1996, 2006). Comets are another source of dust in the inner solar system. Recent modeling work based on in situ measurements carried out by the New Horizons and Pioneer 10 missions indicated that the dust grains originate from Jupiter-family

comets, Oort-Cloud comets, and Edgeworth-Kuiper Belt objects are the dominant source of dust particles for heliocentric distances for ≤ 10 AU, $10 - 25$ AU, and ≥ 25 AU, respectively (Poppe, 2016).

To summarize, in the inner solar system within 5 AU, the major population of interplanetary dust is supplied by (1) catastrophic collisions that happened in the asteroid belt, (2) Jupiter-family comets in addition to (3) small contributions from Oort-Cloud comets (Nesvorný et al., 2010).

Figure 1.1: Zodiacal light (scattered light in the center of the image) and the Milky Way (arc), as seen from Western Australia. Image Credit: Michael Goh.

Cosmic dust is also found in planetary systems and around airless bodies, i.e., moons and asteroids. The main rings of Saturn that can be easily observed with telescopes from Earth consist of particles ranging from boulders to dust particles. Dusty rings are also found around Jupiter, Uranus, and Neptune. Airless bodies are continuously bombarded by meteoroids and produce ejecta particles, whose dynamics are determined by the size of the airless body (Szalay et al., 2018). The Moon, for example, is engulfed by a permanent dust cloud sustained by the meteoroid

bombardment, as characterized by the NASA Lunar Atmosphere Dust and Environment Explorer (LADEE) mission (Horányi et al., 2014, Szalay and Horányi, 2015, 2016). Active moons, including Io, Enceladus, and potentially Europa, are also known cosmic dust sources in the magnetospheres of gas giants.

In addition to the endogenous dust populations, there is an influx of dust particles from the Local Interstellar Cloud (LIC), including interstellar neutral gas and dust particles, traverses through the heliosphere with a relative speed of ≥ 26 km/s (Grün et al., 1993, Frisch et al., 1999). The submicron-sized interstellar dust particles (ISDs) (10^{-18} to 10^{-14} kg) were first measured in situ by the Ulysses spacecraft during its first Jupiter flyby in 1992 (Grün et al., 1993). The estimated mass flux is approximately 6×10^{-20} $\mathrm{kg\,m^{-2}\,s^{-1}}$, which is much less than that of IDPs (Grün et al., 1993). The ISDs show very different dynamical signatures compared to IDPs, including high relative speeds and more homogeneous spatial distribution across the heliospheric latitude ranges.

1.2.2 Dust Dynamics

Another interesting aspect of cosmic dust is that their dynamical evolution is affected by various perturbation forces, such as the Lorentz forces and radiation pressure effects, which vary with particle size. After generation, the orbits of interplanetary dust particles start to evolve differently from their parent bodies. Figure 1.2 shows the production and loss mechanisms as well as the dominating dynamical processes of dust particles in the solar system as a function of dust size and heliocentric distance. For grains larger than 100 microns ($> 10^{-8}$ kg), their dynamics are dominated by gravity, and collision is the primary loss process. With decreasing sizes, radiation pressure and electromagnetic forces become more important in shaping the orbital evolution of IDPs.

For smaller grains in the $1 - 100$ micron size range ($\sim 10^{-8} - 10^{-14}$ kg in mass), dynamical effects caused by the solar radiation pressure start to govern their long-term evolution. This can be understood as the radiation pressure is proportional to the surface area, i.e., $F_{rad} \propto a^2$ where a is grain radius. On the other hand, the momentum of a dust grain is linearly proportional to its

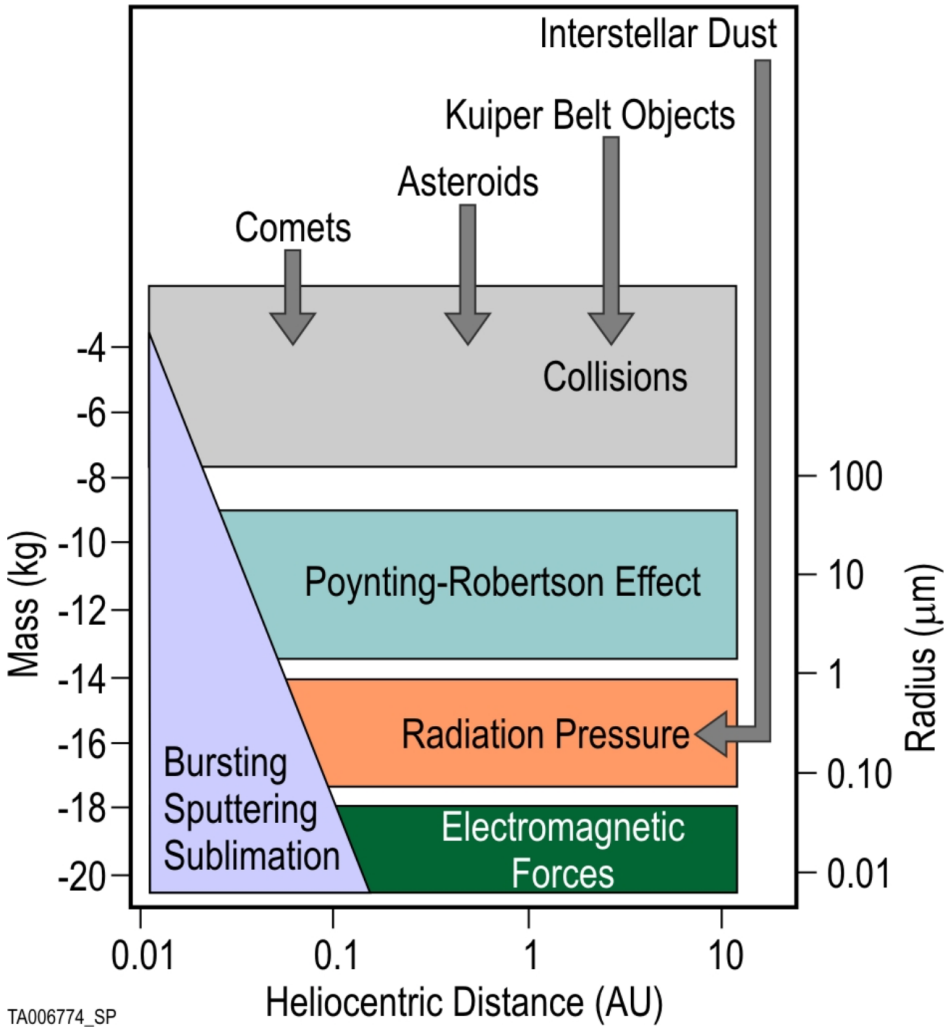

Figure 1.2: Drawing of dust in different mass/sizes corresponds to dominant forces and effects in the solar system. Image Credit: Mihaly Horanyi adapted from Morfill et al. (1986).

mass, or $\propto a^3$. Thus, for smaller grains, the radiation pressure becomes increasingly significant. Next, considering the directionality of solar photons and thermal emission from the dust particles, small IDPs experience an inward migration towards the Sun because of the Poynting-Robertson (P-R) drag. The P-R drag can be understood as the following: photons from solar radiation are absorbed from the direction of the Sun. However, the thermal emission from small dust grains can be considered isotropic. According to momentum conservation, the P-R drag effectively reduces

the dust grain's angular momentum and results in an inward spiral towards the Sun.

For even smaller grains, in the sub-micron range ($\sim 10^{-14} - 10^{-18}$ kg in mass), radiation pressure dominates over gravity, and these particles can be expelled from the solar system (Zook and Berg, 1975). These particles are known as β-meteoroids, and the term "β" is defined as the ratio between the radiation pressure and the gravitational force from the Sun. It is written as

$$\beta = \frac{F_{rad}}{F_{grav}} = \frac{L_* A \langle Q_{PR} \rangle}{4\pi G M_* mc}, \tag{1.1}$$

where L_* represents the stellar luminosity, A and m are the cross-section and mass of the dust grain, respectively. $\langle Q_{PR} \rangle$ represents the radiation pressure coefficient as a function of the spectrum of the incident light, G represents the gravitational constant, and M_* is the solar mass (Mann et al., 2006). β is mainly a function of $\frac{A}{m} \propto a^{-1}$, which is independent of the heliocentric distance (Zook and Berg, 1975). Note that the β value also depends on the optical properties of dust grains and would ultimately decrease with decreasing grain size (Burns et al., 1979).

Dust grains with radii smaller than about 1 micron are also sensitive to electromagnetic forces, as shown in Figure 1.2 (Mann et al., 2004, 2006). Grains smaller than 0.1 micron are conventionally called nano-dust ($\lesssim 10^{-18}$ kg in mass), and electromagnetic forces start dominating their dynamics. Once acquiring electric charges, the Lorentz force typically governs their motion because of the high charge-to-mass ratio. Thus, their dynamics are sensitive to the changing of the electromagnetic environment. High-speed nanodust stream particles from the Jovian and Saturnian systems have been detected by the Ulysses, Galileo, and Cassini missions (Grün et al., 1993, Horányi, 2000, Kempf et al., 2005). Once ejected from the planetary magnetosphere, their motion is coupled to the interplanetary magnetic field structure. The magnetic term in the Lorentz force equation is $F = q\vec{\mathbf{V}} \times \vec{\mathbf{B}}$, where $\vec{\mathbf{V}} = \vec{\mathbf{v}}_{dust} - \vec{\mathbf{v}}_{SW}$, and depends on the relative speed with respect to the solar wind. Hence, these particles can be accelerated to speeds comparable to that of the solar wind, i.e., hundreds of km/s.

Overall, following Figure 1.2, the journey of an IDP in the solar system primarily starts from collisions in the asteroid belt or as ejecta from comets. Through collisional fragmentation, IDPs keep

grinding down and simultaneously lose angular momentum due to the P-R drag. As moving closer to the Sun with a slow inward migration, the IDP number density and orbital speed increases with decreasing heliocentric distance. With the erosion continues (i.e., collision, bursting, sputtering, and sublimation), these IDPs eventually fall into the Sun or escape from the heliosphere into interstellar space. The balance between production and loss processes and the dynamical interactions within the environment determine the distributions of the cosmic dust populations observed today.

1.3 Dust Detection in Space

1.3.1 Detection Methods

The characterization of cosmic dust, including their size and spatial distributions, dynamical and compositional properties, enhances our understanding of the formation and evolution of celestial bodies as well as the solar system. The information about dust particles can be obtained through various detection methods, including the observation of scattered solar radiation, thermal emission, or in situ measurements. Figure 1.3 illustrates the applicable detection methods as a function of size and mass from nano-dust particles to small meteoroids.

Due to their low flux, larger particles ($\gtrsim 100$ μm) can be observed individually only through remote sensing observations, for example, by meteor radars, when the particles enter Earth's atmosphere. One of the observations of cosmic dust is the zodiacal light, i.e., sunlight scattered by IDPs ranging from $1 - 100$ μm in the inner heliosphere. Through photometry, polarization, and spectroscopic observations, we can learn about their size, density, and spatial distributions (Mann et al., 2006). For example, the IDP density from 1.0 to 0.3 AU is found to increase with decreasing heliocentric distance, $n(r) \sim r^{-1.3}$, based on photometric measurements from the Helios spacecraft (Leinert et al., 1981). Only micron and submicron-sized particles have sufficiently large fluxes for in situ detection using instruments deployed on space missions. The most sensitive detection method in this range is based on impact ionization. The impact ionization phenomenon, which will be discussed in detail in chapter 3, occurs during hyper-speed impacts ($\gtrsim 1$ km/s), where a fraction of

incident dust particle and target material is ionized, forming an impact plasma cloud (Auer, 2001). The generated impact plasma can be detected as transient voltage signals that are able to provide precise measurement of the amount of impact charge, which can be used to derive the properties of the incident dust particles (e.g., their mass).

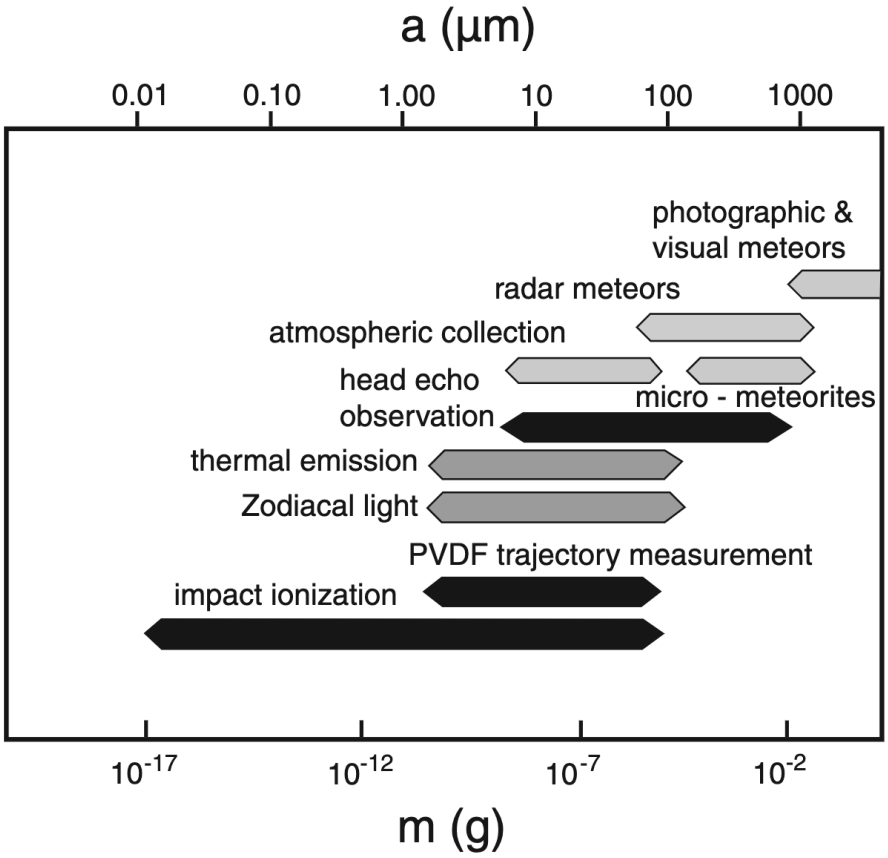

Figure 1.3: Applicable dust detection methods as a function of dust size or mass. Image Credit: Mann et al. (2006).

Compositional measurements inform the source bodies and the chemical evolution of cosmic dust particles in a solar system. Remote sensing methods only provide limited information on composition. Modern in situ cosmic dust analyzer instruments based on impact ionization, however, can provide the elemental and chemical makeup of dust particles by employing time-of-flight (TOF) mass spectroscopy techniques. For example, this had been demonstrated on the Cosmic Dust Analyser onboard the Cassini spacecraft (Srama et al., 2004).

1.3.2 Dedicated Dust Instruments

Several dedicated dust instruments have been flown on planetary and heliophysics missions since the beginning of the space era, including the Helios, Ulysses, Galileo, Cassini, LADEE (Lunar Atmosphere and Dust Environment Explorer), and New Horizons missions (Grün et al., 1985, 1993, Srama et al., 2004, Poppe et al., 2010, Horányi et al., 2014). There are two common types of detection mechanisms: impact ionization dust instruments and PVDF (Polyvinylidene fluoride) detectors.

Figure 1.4 shows the picture and a schematic diagram of the Dust Detection System onboard the Galileo spacecraft as an illustrative example of the operation principle of a dust detector. Once a dust particle passes through the entrance and charge grids, Q_p registers the charge signal due to induced charging. Upon impacting the instrument target, the incident dust particle and the instrument target close to the impact site are vaporized and partially ionized. The bias potentials on the target plate and ion collector grid are configured to collect the electrons (Q_E) and ions (Q_I) from the impact plasma cloud. Then Q_C represents the ion signal received at the channeltron. Combining these measured signals as coincidence detection allows for a reliable characterization of each dust impact event. This method can provide the properties of impacting dust particles, including their impact speed, mass, and grain charge.

Dust analyzers also provide compositional information of the incident dust particles by employing a time-of-flight mass spectrometer. In the following, the Cosmic Dust Analyzer (CDA) onboard the Cassini spacecraft offers an illustrative example. Cassini's CDA instrument detects dust particle impacts through the impact ionization detector (IID), while the chemical analyzer target (CAT) is dedicated to compositional analysis. The example signals are shown in the left and right of Figure 1.5 (Srama et al., 2004). The charge signal QP detected by two entrance grids provides information of the incident direction in two dimensions. During the detection, both QC and QT measure the induced charging by the escaping cations generated upon impact (signal goes negative), while QA and QI measure the charges induced by the cations passing through these grids

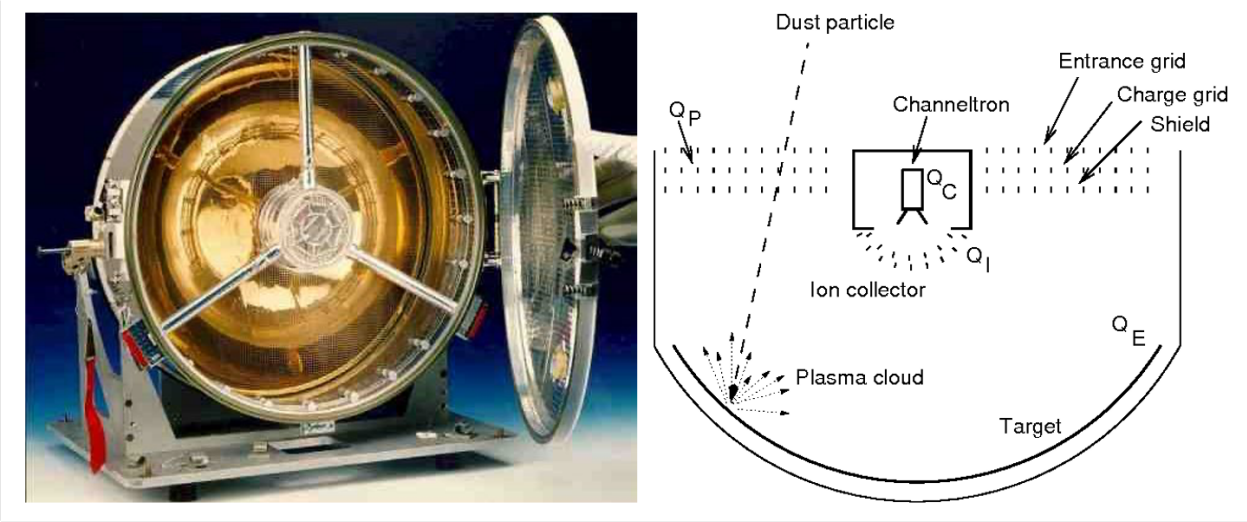

Figure 1.4: Picture and schematic diagram of Galileo Dust Detection System (DDS). The notation of Q_P, Q_E, Q_I, Q_C represents the charge signals detected by charge grid, target plate, ion collector, and the channeltron detector, respectively. Image Credit: ESA and Kruger et al. (1999).

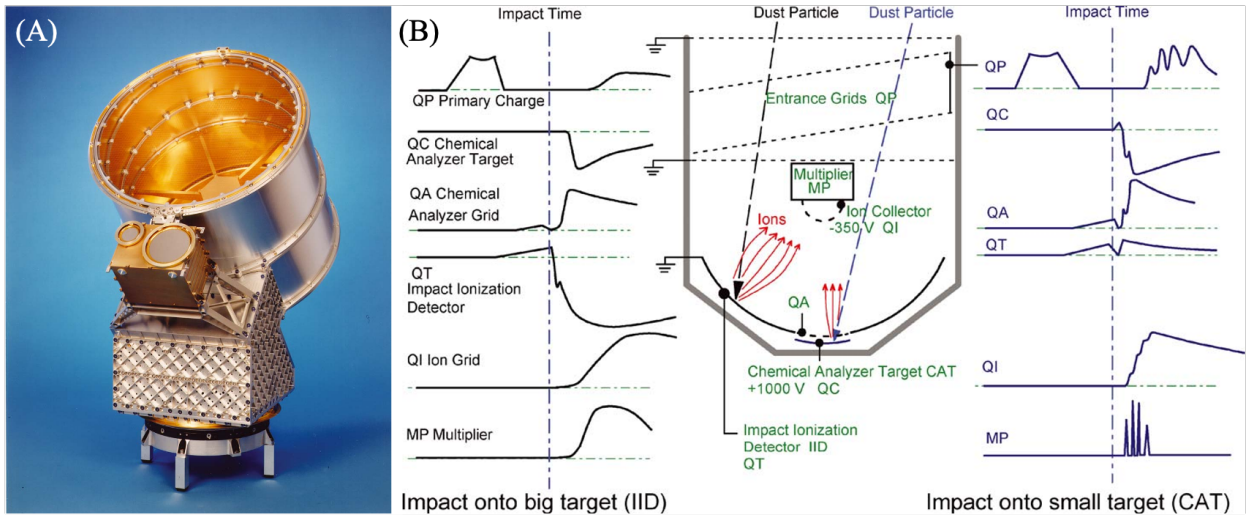

Figure 1.5: Left (A): Picture of the Cosmic Dust Analyzer (CDA) onboard Cassini. Right (B): Hyper-velocity dust impact signals collected by impact ionization detector (IID) or chemical analyzer target (CAT). Image Credit: Srama et al. (2004).

(signal goes positive). The major difference between the CAT and IID impacts is that the CAT target is biased at a high potential of +1000 V to accelerate the cations from the impact plasma towards the multiplier located in the center of the instrument. Since the time required to arrive at the multiplier depends on the mass-to-charge ratio of each cation species, the time sequence of the multiplier (MP) signal waveform is the time-of-flight mass spectrum of the impact generated cations, representing the grains' elemental composition. The bias potential on the CAT increased the mass resolution in the MP signal in comparison to the mixing MP waveforms obtained when impact occurred onto the IID target. The composition information has proven to be valuable for cosmic dust studies. Two of the dust instruments are currently under development: the SUrface Dust Analyzer (SUDA) onboard the NASA Europa Clipper mission and the Interstellar Dust EXplorer (IDEX) onboard the NASA Interstellar Mapping and Acceleration Probe (IMAP) mission. Both are capable of measuring the composition of incident dust particles with an optimized mass resolution.

Taking advantage of high-speed encounters, another type of dust instrument utilizes a thin film composed of Polyvinylidene Fluoride (PVDF), a polarized polymer, for dust detection. With a foil thickness of a few to tens of microns, high-speed dust particle impact will either (a) produce an impact crater or (b) penetrate the foil, thus altering the capacitance of PVDF foil to trigger a small charge pulse as registration of an impact event. Compared to dust detectors and analyzers discussed above, the advantages of the PVDF dust detectors include lower cost, lightweight composition, lower energy consumption, as well as a larger sensitive area. For example, PVDF detectors typically have an effective area of > 0.1 m^2, greater than that of dust instruments with the impact ionization method (Srama et al., 2004). Therefore, they are feasible and beneficial to measuring low dust density environments or focusing on larger grain populations. Several missions have carried PVDF detectors, for example, the Student Dust Counter (SDC) onboard the New Horizons mission (Szalay et al., 2013) and the Arrayed Large-Area Dust Detectors for INterplanetary cruising (ALADDIN) onboard the JAXA IKAROS mission (Hirai et al., 2017). For completeness, the former had a sensitive area of 0.125 m^2, and the latter had 0.54 m^2, compared

to the ~ 0.1 m^2 area of instruments carried by the Ulysses, Galileo, and Cassini missions (Srama et al. (2004) and references therein). The Cassini mission also utilized two PVDF sensors as high rate monitors to measure the flux in dust-rich environments as a part of its Cosmic Dust Analyzer (CDA) instrument. The PVDF detector is mainly employed for the detection of particle size $> 1\mu$m since it is more sensitive to noise related to mechanical agitation and thermal effects according to its piezoelectric and thermoelectric properties. It also provides no direct constraints on the impact velocity and compositional information of incident dust particles. Only the flux, and hence the density or size distributions, can be derived from the PVDF dust instrument data set, given that the impact speed is known.

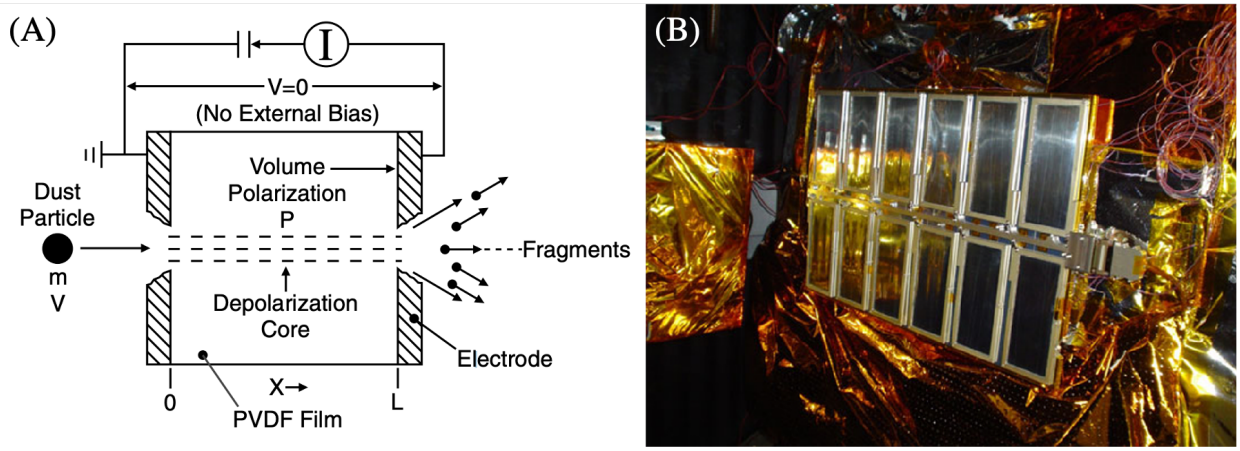

Figure 1.6: Left (A): Schematic of a polarized PVDF detecting impact signal from an incident dust particle penetration. Right (B): Picture of student dust counter carried by New Horizons mission. Image Credit: Srama et al. (2004) and Szalay et al. (2013).

To summarize, dedicated dust instruments flown on space missions can provide a detailed in situ characterization of the dust populations in the solar system, including their dynamical and compositional information, to study the microscopic solid particles that cannot be achieved otherwise. By analyzing the plasma produced from hyper-speed dust impacts, impact ionization dust analyzers provide the most comprehensive information, including grain composition, velocity, and mass. The PVDF detectors provide less information but can be used as a dust counter for various environments with lower costs.

1.3.3 Antenna Instruments

Antenna instruments on spacecraft are primarily designed to measure electric fields and plasma waves in planetary ionospheres and magnetospheres, or the interplanetary medium (Gurnett, 1998). Interestingly, antenna instruments are also sensitive to high-speed dust impacts. Several missions have demonstrated the capability of antenna dust detection, including the Voyager 1 and 2 (Gurnett et al., 1983, Meyer-Vernet et al., 1986, Gurnett et al., 1997), Wind (Malaspina et al., 2014, Kellogg et al., 2016), Cassini (Kurth et al., 2006, Meyer-Vernet et al., 2009, 2017, Ye et al., 2014, 2016a, 2018, 2019), STEREO (Solar TErrestrial RElations Observatory) (Thayer et al., 2016, Zaslavsky et al., 2012), Juno (Ye et al., 2020), MMS (Magnetospheric multiscale) (Vaverka et al., 2018, 2019), Parker Solar Probe (Malaspina et al., 2020, Szalay et al., 2020), among others.

Antenna instruments register dust particles through the transient electric signals associated with the plasma generated upon dust impacts. One major advantage of using antenna instruments for dust detection is that the corresponding sensitive area is large, i.e., the entire surface of the spacecraft. This allows the detection of larger particle populations or those in lower fluxes. The other benefit is that the registered signals provide information on impact plasma parameters and ambient plasma environment. However, the nature of the antenna dust impact signals has not been well understood, which complicates the interpretation of data. Given that antenna instruments are common on space missions, antenna dust detection provides unique and complementary data sets to dedicated dust instruments. This thesis aims to construct a detailed numerical model to interpret dust impact signals registered by antenna instruments. The goal is to (1) comprehensively understand the signal generation mechanisms and (2) quantitatively improve data interpretation of cosmic dust detection using antenna instruments.

Chapter 2

Antenna Instruments

Spaceborne antenna instruments have been developed to investigate electric and magnetic fields as well as plasma waves in space since the 1960s. For example, Alouette 1 was the first satellite carrying an electric dipole antenna into space to study natural and artificial very-low-frequency (VLF) signals propagating in the top of Earth's ionosphere (Barrington et al., 1963). As for dust detection, Voyager 2 was the first mission to collect both the voltage waveforms and intensive broadband noise in frequency spectra caused by dust particles (Gurnett et al., 1983). The main design parameters for antenna instruments are: (a) the number of orthogonal axes measured, (b) the desired frequency range, as well as (c) the sensitivity and dynamic range of the instruments. First, antennas measure the intensity of the electric field that can be coordinated with measurements from magnetometers to provide the directional energy flux, i.e., Poynting vector $\vec{S} = \vec{E} \times \vec{B}$. These parameters illustrate the propagation and interaction of fields and waves in space. Second, the desired frequency range may span from DC or just below the ion cyclotron frequency (few Hz) to higher than the electron plasma or cyclotron frequencies (tens of MHz). In detail, the number density of surrounding charged particles sets the plasma frequency, while the ambient magnetic field determines the cyclotron frequency. Thus, the frequency range is constrained by these parameters of the measured environment. Third, sensitivity and dynamic range describe the spectral intensity that an antenna instrument can detect. Overall, the large variety of measured plasma environments makes every antenna instrument customized to satisfy mission requirements. As for the complementary detection of dust particles, we will introduce the relevant characteristics, spatial

arrangements, and data products of antenna instruments in this chapter. Several representative missions are also discussed.

2.1 Antenna Characteristics

2.1.1 Physical Length

There are two dominant charging mechanisms in space: photoelectron emission and thermal electrons collection, which drive the spacecraft's potential positive or negative (relative to infinity). An equilibrium potential established on the spacecraft means that these two mechanisms are in balance. The Debye length of the ambient plasma is the characteristic length of electrostatic shielding. If it is desired to measure DC electric fields accurately, the antenna length should be longer than the Debye length in order to isolate the interference from the SC body. For instance, interplanetary space has a Debye length of ~ 10 m. A relatively dense plasma environment corresponds to a shorter Debye length; for example, $\lesssim 2$ m in the near-Sun environment (Bale et al., 2016). From the aspect of radio and plasma wave measurements, the plasma sheath effect is no longer an important issue. The antenna's physical length only determines the detectability of the frequency/wavelength range and the antenna capacitance. Overall, the antenna length is set by the desired frequency range and the parameters of the ambient plasma environment.

2.1.2 Measurement Configurations

In electric field and plasma wave measurements, antenna instruments are operated either in monopole or dipole modes. The former measures the potential difference between the antenna and spacecraft ($V_{meas} = V_{ANT} - V_{SC}$), while the latter measures the potential difference between two antennas ($V_{meas} = V_{ANT,1} - V_{ANT,2}$). Monopole mode treats the spacecraft body as electric ground; however, it may be susceptible to noise generated by onboard electronics. On the other hand, dipole mode eliminates the spacecraft influences, thus allowing more precise field and wave measurements. Dipole configuration is the common choice for space plasma measurements.

Dust detection by antenna instruments relies on the effective area to register transient voltage perturbations upon impact. The monopole configuration usually has a larger effective area than that of the dipole. Note that this does not imply that the dipole configuration is insensitive or inappropriate for dust detection. Both configurations can perform dust detection but have different effective areas and specific advantages. The analysis and interpretation of monopole versus dipole detection will be discussed in Section 6.4.

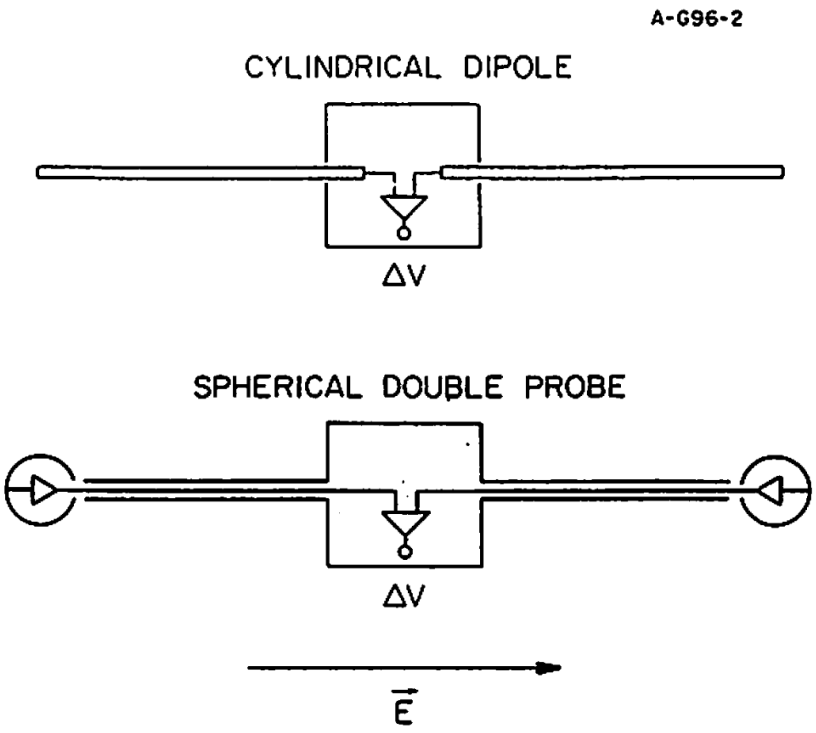

Figure 2.1: The geometry of a cylindrical dipole antenna and a spherical double probe. The differential amplifier provides the ΔV voltage outputs are denoted. Image Credit: Gurnett (1998).

In traditional dipole configuration, the two types of geometries are cylindrical dipole antennas and spherical double probes, as shown in Figure 2.1. The main difference is due to their sensitive area. For a cylindrical dipole antenna, the entire antenna body takes measurements in space plasma, and the preamps are integrated at the stub of the cylinders near the SC body. For spherical double probes, the sensitive elements are only the tips, and the preamps are integrated locally, while the

supporting booms are held at the SC potential (Gurnett, 1998). The former refers to missions carrying stacer booms (e.g., STEREO) or whip antennas (e.g., PSP), while the latter corresponds to the MMS mission, as introduced in the next section.

2.1.3 Capacitance and Capacitive Coupling

Antenna capacitance in different geometries can be estimated through the equations provided below. For the cylindrical shape (the top panel in Figure 2.1), the antenna capacitance relative to infinity can be approximated as:

$$C_{A,cylinder} = \frac{2\pi\epsilon_0(L)}{ln(\frac{L}{a}) - 1}, \tag{2.1}$$

where L and a are the length and radius of the cylindrical element, respectively, followed by the vacuum permittivity ϵ_0 (Jordan, 1951, Gurnett, 1998, Gurnett et al., 2004). On the other hand, a spherical probe (the bottom panel in Figure 2.1) is much simpler and given by

$$C_{A,sphere} = 4\pi\epsilon_0\, a, \tag{2.2}$$

where a is the radius of the spherical probe.

Antenna instruments in arbitrary spacecraft−antenna systems have capacitive coupling effects that reduce the signal amplitude of measurements in certain frequency range. An "antenna gain" is introduced to describe the ratio of output voltage against the input one given by the capacitive divider,

$$G_A = \frac{\Delta V_{out}}{\Delta V_{in}} = \frac{C_A}{C_A + C_x}, \tag{2.3}$$

where C_A represents the antenna's physical capacitance to infinity and C_x is the mutual coupling capacitance between the antenna and the SC. The C_x includes the capacitance of base, cables, preamps, and geometry of the SC−antenna system (Gurnett, 1998, Bale et al., 2008, Shen et al., 2021b). These capacitance values can be measured in the laboratory. In order to achieve an ideal voltmeter and reduce the coupling effect, it is better to make $C_A \gg C_x$. Comparing the capacitance of cylindrical and spherical geometry, we can find that the cylindrical one performs well through a larger value of C_A due to its aspect ratio of $L \gg a$ (Gurnett, 1998).

2.1.4 Front-End Electronics

The front-end electronics of antenna instruments requires high input impedance in order to avoid interfering with the voltage measurement. In addition, the bandwidth and rise time of the electronics determine the measured frequency range and how fast they can respond. The corresponding data volume and power budget are constrained by the mission design.

2.2 Antenna Categories and Arrangements

In this section, we will discuss the mechanical arrangements of antenna instruments, including the conical stacer, cylindrical whip, and spherical double probe.

2.2.0.1 Stacer Antenna

Several missions have applied the stacer antennas for plasma wave measurements; for example, Cassini (Gurnett et al., 2004) and STEREO (Bale et al., 2008). Figure 2.2 shows a stacer boom antenna on the STEREO mission (size not to scale). A stacer boom is made as a flat spring that is rolled with a constant helical pitch and fixed diameter. The deployed stacer antennas are thus conical in shape with typical lengths of $1 - 10$ meters, and the diameters of the tip are in sizes of $4 - 55$ mm (Bale et al., 2008). The spring element is usually made out of beryllium copper and may be painted dark to reduce intrusions upon optical measurements.

Figure 2.2: Photo of Beryllium copper stacer antenna used in the STEREO mission. The aspect ratio is exaggerated for display purposes and not to scale, meaning that it should be a narrower diameter in practice. Image Credit: Bale et al. (2008).

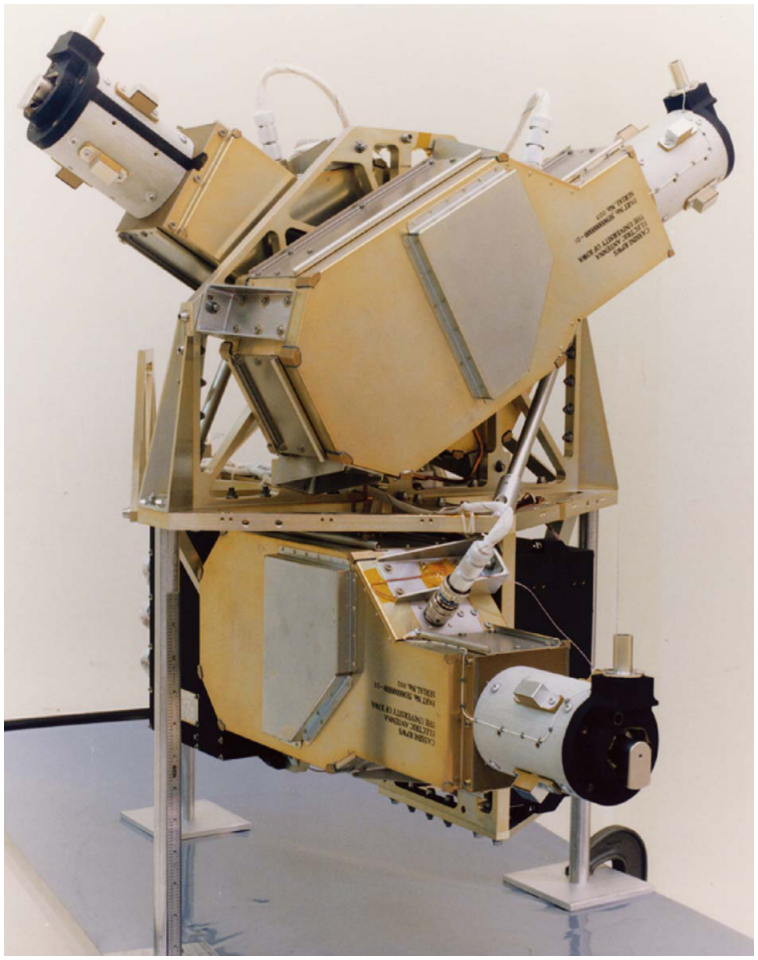

Figure 2.3: Photo of Radio and Plasma Wave System (RPWS) antenna assembly on Cassini spacecraft. The three deployment stubs are shown in the view and the rest are the integrated electronics housing inside the assembly. Image Credit: Gurnett et al. (2004).

Figure 2.3 displays a three-axis deployment device carried by the Cassini spacecraft. At deployment, each stub slowly releases the stored stacer and further extends it to the designated length. For instance, the full lengths of electric antennas equipped by Cassini and STEREO missions are 10 m and 6 m, respectively (Gurnett et al., 2004, Bale et al., 2008). Note that the deployment structures are installed close to one another in both the Cassini and STEREO missions (see Figure 2.3). Such spatial arrangement increases the capacitive coupling between antennas, thus altering the measurement characteristics (details in Section 5.4.2). In laboratory measurements, we have employed a reduced-size model of Cassini SC with the same spatial arrangement (see Figure 5.5).

2.2.0.2 Whip Antenna

The Parker Solar Probe (PSP) mission carries four whip electric antennas ($V1-V4$) mounted near the front heat shield, as shown in Figure 2.4. These antennas are 2 m in length and 3.2 mm in diameter, and made out of thin-walled Niobium tubes in order to withstand the thermal environment near the Sun. Each antenna can be operated as a monopole or in a dipole configuration. These PSP antennas can perform DC electric field measurements when operated as double probes

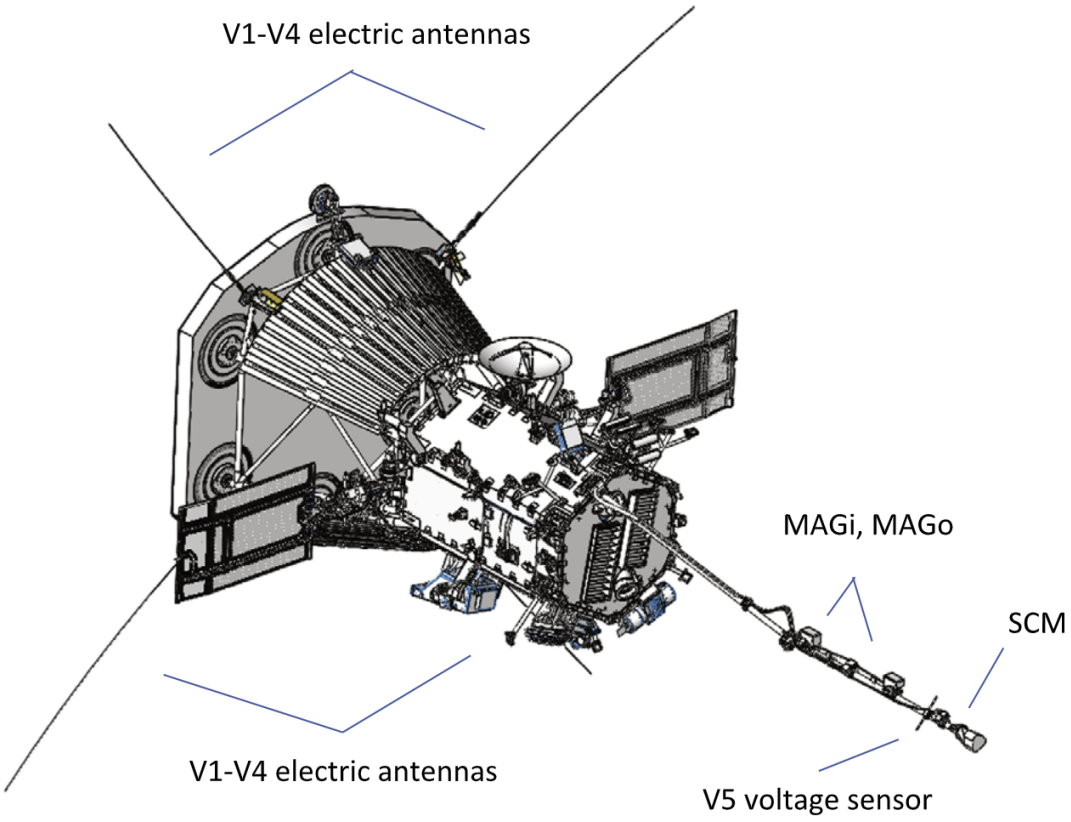

Figure 2.4: Photo of FIELDS instrument carried by Parker Solar Probe, including four electric antennas ($V1-V4$) and a voltage sensor ($V5$) along with three magnetic sensors (MAGi, MAGo, SCM) to measure electromagnetic field and waves in the near-Sun environment. Image Credit: Bale et al. (2016).

(Mozer, 2016), or make radio and plasma wave measurements from below the ion cyclotron to beyond the electron cyclotron frequency (Bale et al., 2016). Considering that the whip antennas

are not placed near each other, the capacitive coupling between antennas is small. It means the amplitude of signals is affected only by the coupling between antennas and the spacecraft. A simplified spherical SC built for laboratory measurements follows a similar arrangement of the antennas. It aims to characterize the signal coupling between monopole and dipole modes with respect to different impact locations (see SC model in Figure 5.5 and the analysis is provided in Section 6.4).

2.2.0.3 Double Probe

The MMS mission has a unique suite equipped with six voltage probes, three magnetometers, and an electron drift instrument to study the electromagnetic field and plasma waves in Earth's magnetosphere. Two probes are configured as axial double probes (ADP), and the remaining four as two pairs of spin-plane double probes (SDP) (Figure 2.5). Each dipole pair measures the voltage difference between two probes placed on the opposite side of the SC (180° apart). Figure 2.6 shows the schematic of one of the spin-plane double probe (SDP), where the spherical probe connects to the deployer through a long boom cable and a fine wire. In contrast to whip antennas that are fully exposed, the double probe has only the probe tips that take measurements. The rest of the supporting structures are electrically connected to the spacecraft chassis. Referring to the schematic presented in the bottom panel of Figure 2.1, the preamp is integrated near the sensing area (the probe and thin wire). Similarly, each side of the axial double probe (ADP) has a sensor of 1 m in length, extending $\sim$ 13 m away from the spacecraft body through a boom held at ground potential (Ergun et al., 2016).

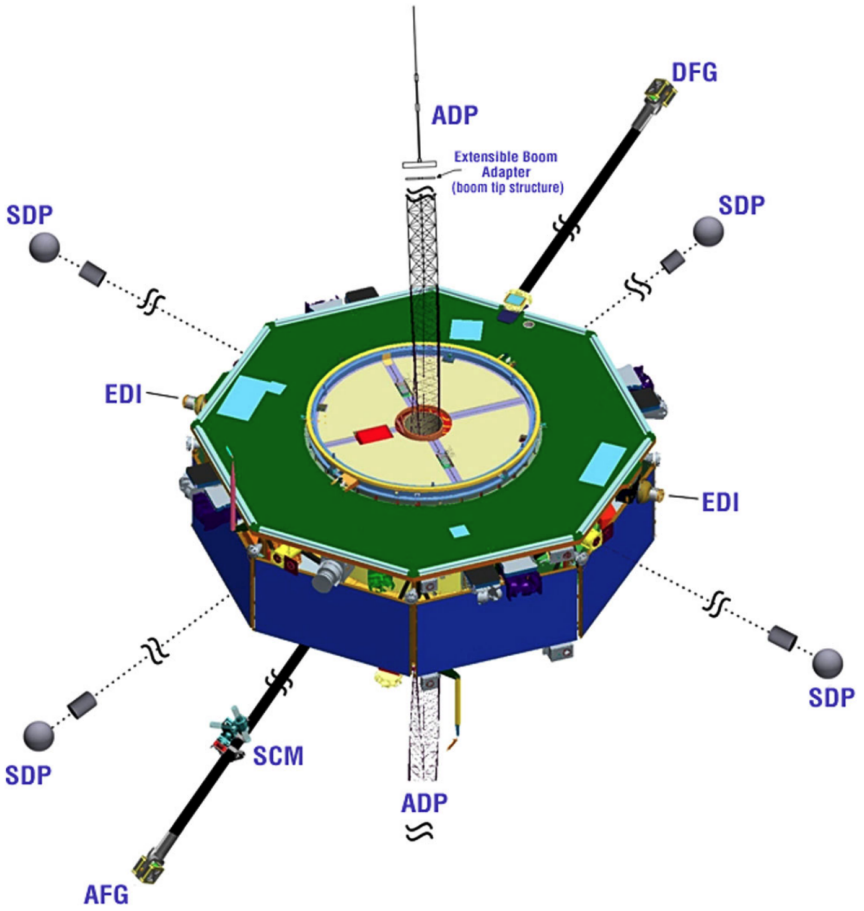

Figure 2.5: Photo of FIELDS instrument sute carried by the MMS, including a pair of axial double probe (ADP), two pairs of spin-plane double probe (SDP), an electron drift instrument (EDI), and three magnetometers (AFG, DFG, and SCM). Image Credit: Torbert et al. (2016).

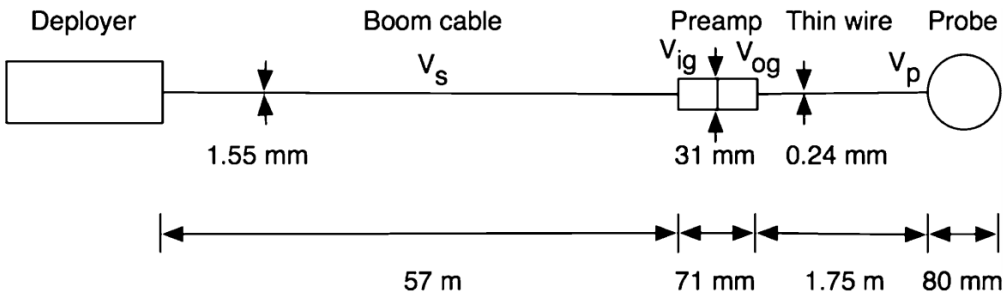

Figure 2.6: Schematic of the spin-plane double probe instrument, including a deployer, the boom cable, the preamp, a thin wire, and the probe. Those detected potentials at corresponding locations are indicated. Image Credit: Lindqvist et al. (2016).

2.3 Data Products

Considering the wide bandwidth spanning from few Hz to MHz and the dynamic range of the measurements, the data volumes generated by the antenna instrument can be substantial. Therefore, onboard processing is needed to optimize the data storage but should still satisfy scientific purposes. The integrated electronics include analog processing, digital processing, and the field-programmable gate array (FPGA) control unit (Bale et al., 2016). The analog processing performs signal separation (e.g., DC-coupled or AC-coupled), produces differential signals (i.e., monopole or dipole modes), applies anti-aliasing and amplifications. Digital processing is responsible for conditioning, filtering, digitization, and signal processing. The FPGA logic unit controls the data flow and acts as an interface between instruments and spacecraft subsystems. In addition, a time-domain sampler is usually applied to make rapid sampling and perform data acquisition, triggering, analysis as well as selection. It has the highest sampling rate to register burst events, which benefits the registration of transient voltage perturbations generated upon dust impacts. Primary data products include (1) time-domain voltage waveforms and (2) frequency spectra. The voltage waveforms are initially dedicated to electric field analysis through $E = -dV/dx$. When dust impact occurs, the voltage perturbations will interfere with or overwhelm the field and wave measurements, thus detecting a unique signal response to the expansion of impact-generated plasma. On the other hand, radio and plasma wave measurements utilize frequency spectra to characterize space plasma parameters and identify different modes of plasma waves. Dust impacts can also be detected as wideband noise in the antenna signals' power spectrum (Aubier et al., 1983, Meyer-Vernet et al., 2009). However, this provides limited information on dust particles.

Chapter 3

Impact Generated Plasma

Individual dust particles in space can be detected in situ by a variety of methods that were summarized by Auer (2001), and are illustrated in Figure 3.1. These include non-destructive methods, for example, the detection of the scattered light from a particle or the charge it carries. The impact of the dust particle on a solid target surface generates a number of physical phenomena that can be used for their detection and characterization. These include the perforation of thin foils, impact cratering of polarized material, impact momentum, the generation of impact light flash, or the impact ionization of the dust particle. The latter phenomenon provides the most sensitive detection method and has been employed in a range of dust instruments. In impact ionization, the initial kinetic energy of the particle is used for the heating, evaporation, and ionization of some fraction of the dust particle and the target material. Impact ionization may also be used to analyze dust particles, as the ion species generated in the process are characteristic of its composition. As mentioned earlier, impact ionization also makes antenna instruments sensitive to dust impacts. This chapter provides a brief review of impact ionization, the existing (and limited) models of this process, and the characteristics of the impact plasma determined from laboratory measurements. Section 3.3 is a description of new laboratory data, namely the measurements of the impact charge for heat shield material used on the Parker Solar Probe mission.

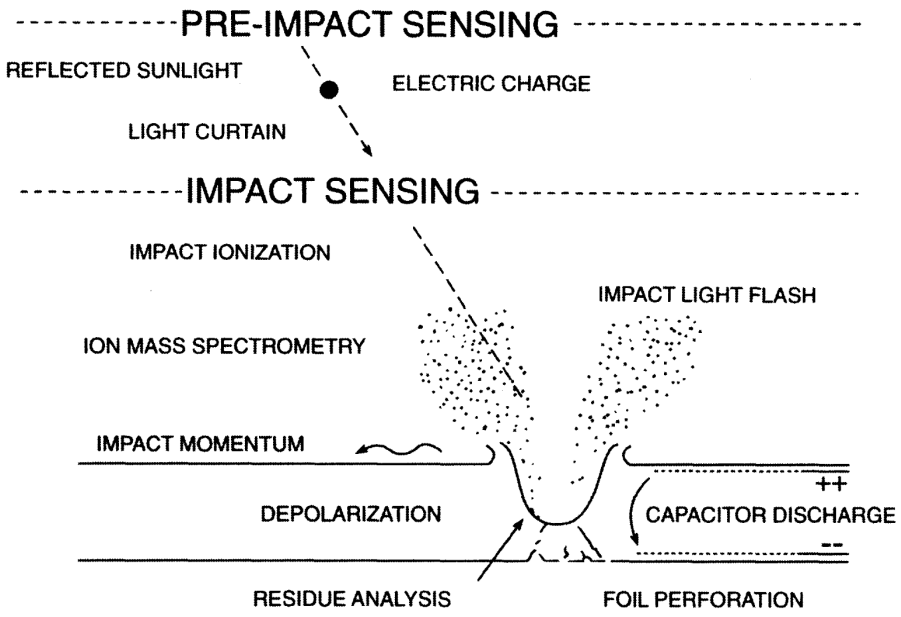

Figure 3.1: Illustration of in-situ detection methods of dust impacts. Image Credit: Auer (2001).

3.1 Impact Ionization

Several models have attempted to describe the process of impact ionization. Each of these models has demonstrated success in the qualitative description of certain aspects in space observations and laboratory measurements. However, to date, there is no model based on first principles that would provide comprehensive agreement with the observations. In the following, three models will be introduced.

The plasma ionization model presented by Drapatz and Michel (1974) assumes that the impact generates a shock wave that propagates through the material and reflects from the interfaces. The initial energy is dissipated into heat and results in a hot and dense plasma. The ionization probability for the atomic species scales with their ionization energy E_i in the form of a Boltzmann distribution, $exp(-E_i/kT)$, where kT is the thermal energy. In the model, the shock-wave ionization is followed by the adiabatic expansion of the impact plasma, where ion-molecular reactions may continue until the plasma becomes collisionless.

The desorption ionization model proposed by Kissel and Krueger (1987) and Krueger (1996) is a semi-empirical approach, where the ions are generated from the adsorbed layer on the particles. The impact provides the energy for the desorption of the molecules and the chemical cleavage forming the ions. In this model, ion production scales with the effective area of the impact and the dissipating energy density. However, this model cannot explain, for example, the presence of cluster ions that are frequently observed in the impact plasma plumes. In addition, it also cannot explain the substantial increase of impact charge generation with increasing impact speed; i.e., beyond the number of the adsorbed molecules.

Finally, the volume ionization model developed by Hornung and Kissel (1994), and Hornung et al. (1996) was aiming for high impact speeds ($v > 50$ km/s). The model employs a complex, multi-parametric function for the description of the ionization efficiencies of the species. Actual data of ion compositions are then used in an iterative procedure to derive the ionization efficiency function.

3.1.1 Ionization Process

In summary, impact ionization is a process of a dust particle evaporating and partially ionizing upon impacting a solid surface with velocities larger than about 1 km/s. Charged particles are released from the impact in the form of a plasma cloud, which allows dust compositions to be analyzed through a time-of-flight mass spectrometer. Both the dust and target materials contribute to the impact ionization process. Volume and surface ionization likely take place as parallel processes.

Mocker et al. (2013) measured the charge yield of iron (Fe) dust impacting the silver (Ag) target, and the results agree with the above description. In Figure 3.2, the relation between the charge yield and the impact speed indicates that two regimes of ionization correspond to the surface and volume ionization processes, occurring at low (≤ 10 km/s) and high impact speeds (≥ 20 km/s), respectively. At low impact speeds, only the outer part of the dust grain is affected by impacts, as the energy released is not sufficient enough to affect the entire dust grain. With increasing impact speeds, the increasing impact energy implies that the entire grain is eventually consumed by the

vaporization and ionization processes. Thus, the charge yield is proportional to the volume of the dust particles. Since the surface and volume of a dust particle can be approximated as a^2 and a^3 (assuming a spherical particle with a radius a), one can understand why the linear relation of impact speed in volume ionization has a steeper slope than that of surface ionization, as shown in the right panel of Figure 3.2.

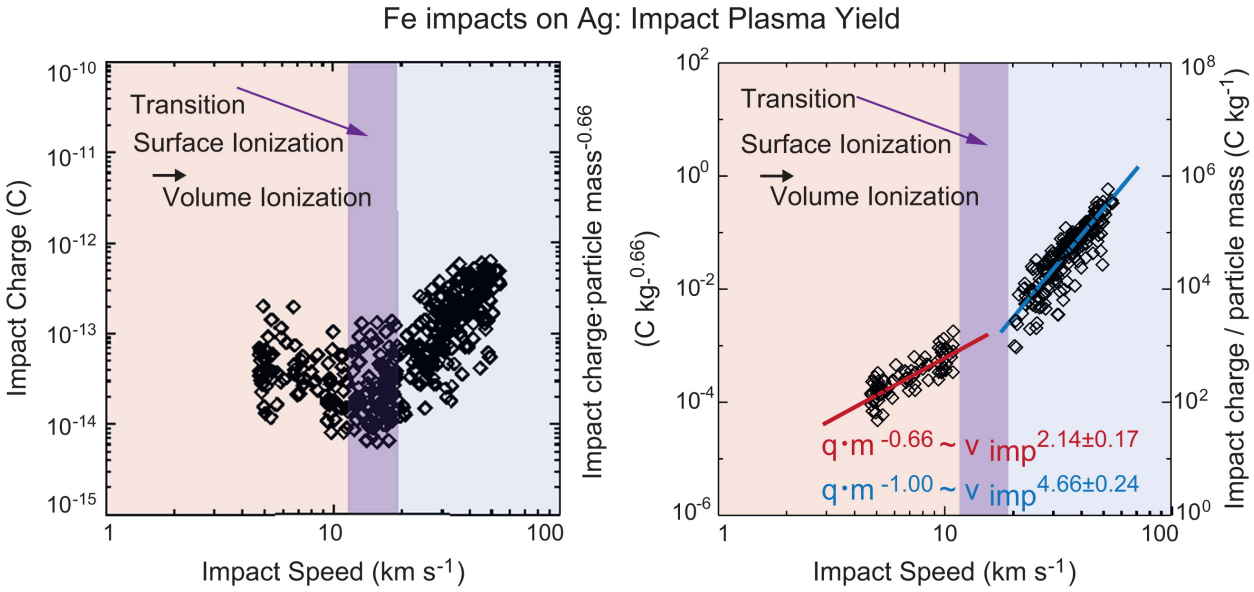

Figure 3.2: Impact charge yield of iron dust impacting the silver target. The impact charge yield depends on the impact speed. The areas colored red, purple, and blue denote the regimes of surface ionization, transition zone, and volume ionization, respectively. The relations of impact charge to dust's mass ratio versus impact speed are listed in the right panel, having different exponent coefficients. Image Credit: Mocker et al. (2013).

3.2 Impact Plasma Characteristics

3.2.1 Charge Yield (Q_{IMP})

An impact ionization plasma cloud generated from dust impacts consists of electrons and cations (assuming anions can be neglected for simplification). The total impact charge (Q_{IMP}) scales with the mass (m) and speed (v) of the impacting particle following a power law:

$$Q_{IMP} = Q_i = |Q_e| = \gamma\, m^{\alpha}\, v^{\beta}, \tag{3.1}$$

where parameters γ, α, and β can be determined from laboratory calibration measurements (e.g., Auer (2001), Collette et al. (2014), and Table 3.1). An assumption is made here that the total charges of positive (Q_i) and negative (Q_e) charge carriers are equal. In this equation, the generated impact charge (Q_{IMP}) is a linear function of the dust mass (i.e., $\alpha \simeq 1$) and a steep function of the impact speed with $\beta \simeq 3-6$. If the impact speed of particles on target surfaces can be determined from orbital mechanics or other detection methods, the mass of the dust particle can be derived from the amount of impact charge. This is provided that the measured impact charge yield through the detection process is thoroughly understood. The coefficients (e.g., γ and β in Equation 3.1) are mostly set by the target material and can be obtained from laboratory calibrations using a dust accelerator. Table 3.1 provides the scaling relations of common spacecraft materials.

Table 3.1: Impact charge yield relations reported in literature and this thesis.

Target Material	Scaling Relation[a]	Impact Speed (km/s)	Reference
Ag	$8.9 \times 10^{-3}\, mv^{3.9}$	$2-40$	Collette et al. (2014)
Al	$7.0 \times 10^{-1}\, m^{1.02} v^{3.48}$	$2-40$	McBride and McDonnell (1999)
Al	$1.4 \times 10^{-3}\, mv^{4.8}$	$8-46$	Grün (1984)
Au	$6.3 \times 10^{-4}\, mv^{5.6}$	$9-51$	Grün (1984)
Ag/BeCu (Antenna)	$5.0 \times 10^{-2}\, mv^{3.9}$	$3-40$	Grün et al. (2007)
BeCu	$1.2 \times 10^{-2}\, mv^{3.8}$	$2-30$	Collette et al. (2014)
Heat shield[b]	$4.3 \times 10^{-2}\, mv^{3.46}$	$16-40$	This thesis work, see Sec. 3.3
Kapton (Al coated)	$1.0 \times 10^{-2}\, mv^{4.6}$	$3-40$	Grün et al. (2007)
Kapton (Ge coated)	$2.5 \times 10^{-3}\, mv^{4.5}$	$2-40$	Collette et al. (2014)
MLI[c]	$1.7 \times 10^{-3}\, mv^{4.7}$	$2-40$	Collette et al. (2014)
PCB[d]-Z paint	$4.7 \times 10^{-3}\, mv^{4.1}$	$3-36$	Grün (1984)
Polyimide	$1.2 \times 10^{-1}\, mv^{3.3}$	$3-45$	Grün et al. (2007)
Solar cell	$4.7 \times 10^{-3}\, mv^{4.2}$	$2-40$	Collette et al. (2014)
W	$5.1 \times 10^{-1}\, mv^{3.5}$	$2-40$	Dietzel et al. (1973)

[a] The units in scaling relation are mass in kg and speed in km/s.

[b] Heat shield for Parker Solar Probe is made of Carbon-Carbon base with Alumina coated.

[c] MLI, Multi-layer insulation.

[d] PCB, Print citcuit board.

3.2.2 Effective Temperatures (T_e and T_i)

The effective temperatures of electrons and ions of an impact plasma cloud determine its electrodynamic effects, including the escape/recollection fraction from the charged target surface. The temperatures of impact plasma electrons (T_e) and ions (T_i) can be measured by laboratory impact experiments. The experiments measure the collected charges normalized to the dust's mass as a function of the bias potential on target. Several assumptions have to make here, which are: (1) both positive and negative charge carriers have equal quantities, (2) these charge carriers are singly charged, and (3) the escaping charges move away to infinity and leave behind the recollected ones. An equations is provided to fit the net charges (Q_{col}) recollected on target at various biased potentials (U_{bias}) to obtain the effective temperatures T_s for species s ($s = e$, i):

$$\frac{|Q_{col}|}{m} = \frac{Q_T}{m}\left(1 - e^{\frac{-|U_{bias}|}{T_s}}\right). \tag{3.2}$$

Note that Q_T represents the quantity when the produced charges upon impact are entirely collected at a high bias potential (i.e., $|U_{bias}| \to \infty$). Collette et al. (2015) performed experiments using iron dust particles as projectiles impacting on a tungsten (W) target. Results showed that $T_e \lesssim 5$ eV and T_e is independent of the impact speed within the range of $4 - 20$ km/s. On the other hand, T_i increases from 4 to 25 eV, corresponding to a low speed of 4 km/s to the hyperspeed 20 km/s, respectively. Nouzák et al. (2020) provided similar results with T_e on the order of 1 eV, and T_i ranges from 10 to 15 eV with the impact speed of ≥ 20 km/s using the same Fe-W dust-target combination. Another laboratory experiment performing olivine particles (with the same W target) showed that the $T_i \simeq 7$ eV and is independent of impact speeds ranging from 2 to 18 km/s. In contrast, T_e varies from $1 - 10$ eV. The authors suggest that this discrepancy may be caused by anions generated in the impact plasma cloud due to the organic coating of olivine particles (Kočiščák et al., 2020).

In addition, the proposed model in this thesis (details provided in Chapter 4) has recently been employed to obtain effective temperatures by fitting the model to the waveforms collected in laboratory measurements. The fitting results provided that $T_e = 6 - 9$ eV, and $T_i = 12 - 38$ eV

for impact speed ≥ 20 km/s (see Section 6.1), both are higher than the reported values. However, given the complex coupling between the fitting parameters in the model, these of the same order values are still in qualitative agreement with previous results. Nonetheless, this method discussed in Section 6.1 provides an alternative way to obtain effective temperatures.

3.2.3 Expansion Speeds (v_e and v_i)

The duration of the transient impact plasma cloud is determined by the expansion speeds of its constituents. As the cloud expands, the lighter and faster electrons move outward isotropically, leaving behind heavier and slower ions. Typically, the expansion speed of electrons and ions are on the order of 1,000 km/s and 10 km/s, respectively. Lee et al. (2012) reported the expansion speed of impact plasma ranges from 10 to 30 km/s depending on the combination of dust and target materials. The most recent analyses, as described in Section 6.1 and 6.2, obtained a similar ~ 10 km/s ion expansion speed through fitting the laboratory impact signal waveforms with the newly developed electrostatic model (Shen et al., 2021a,b).

3.2.4 Angular Distribution

In contrast to the isotropic expansion of electrons, the motion of ions has been considered a conical plume. For low-speed impacts ($1 - 4$ km/s), the only existing work was done by Abramov et al. (1991), who reported that the ion plume's half-opening-angle ranges from $5° - 65°$ with the most probable values around $16° - 36°$. Only until recently, constraints for high-speed impacts (≥ 20 km/s) have been derived. Based on our laboratory analysis of dust impact signals registered by the antenna instruments, the ion plume produced from high-speed impacts expands in the form of a divergent cone rather than a narrow beam, as discussed in Section 6.2. Further direct measurements are required to characterize the impact plasma expansion and to provide constraints on its dependence on the impact speeds and possibly dust-target material combinations.

3.3 Charge Yield Measurements of Parker Solar Probe's Heat Shield

A calibration measurement of the impact charge yield of the heat shield used on the Parker Solar Probe (PSP) was carried out using the dust accelerator facility. Parker Solar Probe is the first solar observation probe with the most adventurous orbit to closely approach the Sun, deeper into the solar atmosphere, with a record high speed at perihelions. In order to overcome the temperature threat, PSP carries a heat shield known as the Thermal Protection System designed by the Applied Physics Laboratory at Johns Hopkins University. The dimension is 2.4 meters in diameter and approximately 115 mm thick. It was built with multiple carbon layers consisting of a carbon composite foam interjacent between two carbon plates. The surface treatment is a layer of plasma-sprayed alumina (Al_2O_3) at the sun-facing side to reflect sunlight and reduce heat deposition. In a thermal vacuum test, the heat shield is demonstrated to hold up to 1650°C. In the shadow of the heat shield, the spacecraft body and instruments thus sit at a normal operating temperature at $\sim 30°C-70°C$.

Figure 3.3 shows the experimental setup for the impact charge yield measurements. A piece of heat shield material with 2.5 cm by 2.5 cm size is attached to an electrically isolated PEEK mount, as shown in the left panel. Note that only one side of this heat shield sample was covered with alumina and is non-conductive at room temperature. The surface on the opposite side is made of conductive carbon composition material. Since both sides are rough surfaces and are brittle for drilling, the experimental wiring is soldered on a copper slice attached to the target using conductive carbon tapes for charge measurements.

The right panel of Fig. 3.3 provides a schematic of the measurement setup, similar to that performed in other experiments (Kočiščák et al., 2020). An opening of 25 mm in diameter on the front plate at the right allows the incident dust beam ($\sim$ 1 mm diameter) to access the heat shield sample. Both the front plate and the gridded aperture are biased at $\pm$100 V for measuring negative and positive charge yields, respectively. These high bias potentials ($\pm$100 V) are applied to ensure obtaining the full amount of charges produced from impacts since the effective temperatures

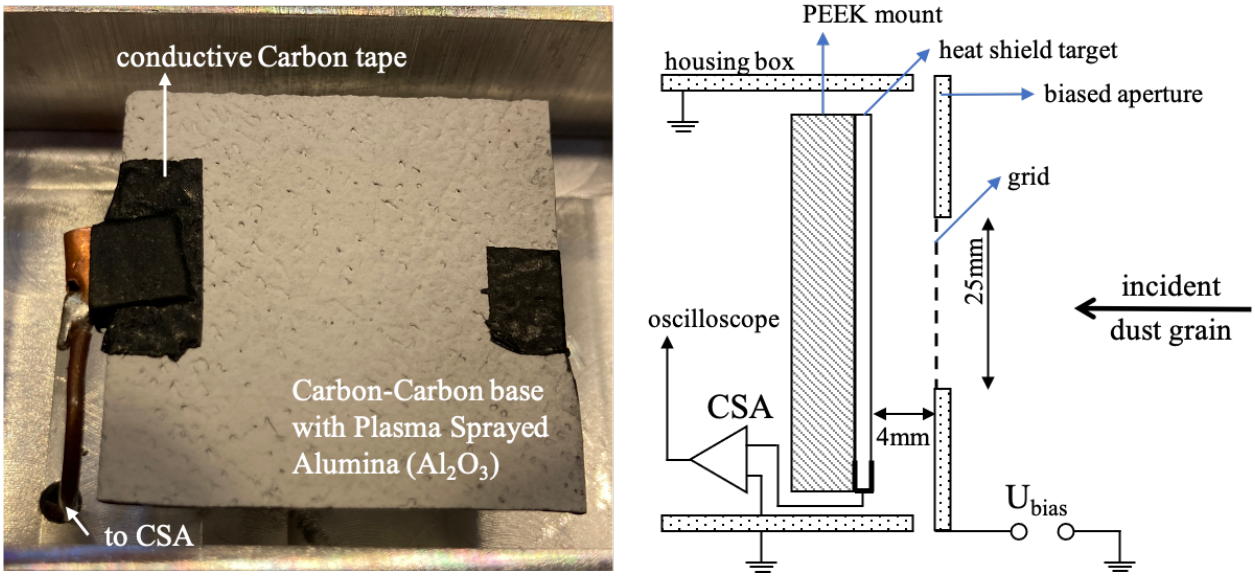

Figure 3.3: Impact charge yield measurement for iron dust impacting Parker Solar Probe's heat shield. The left panel shows the heat shield material with a rough surface sprayed by alumina, and the right panel illustrates the schematic diagram of the measurement setup.

are expected to be < 100 eV, as discussed. The rest of the aluminum housing box is grounded. The distance between the target surface to the biased grid is 4 mm, in order to provide a uniform electric field for the escaping charges generated upon impact. Because of the non-conductive alumina-sprayed surface, only the induced charges on the back conductive side of sample can be measured. In other words, there is no measurement of charges deposited on the alumina surface, and only the induced charges will be collected through a charge-sensitive amplifier (CSA). The signal caused by the induced current is integrated by the CSA, producing a voltage signal with an amplitude proportional to the incoming input charges. Due to the characteristics of charge to voltage conversion, the charge sensitivity of the CSA (Amptek A250) used in this measurement is 5.75×10^{12} V/C. The charge yield, $Q_{IMP} = Q_i = |Q_e|$, can thus be calculated by converting the voltage amplitude back to the amount of impact charges.

Preliminary results of the impact charge yield of the PSP heat shield target are presented in Figure 3.4. A total of 1,809 impact events have been registered in the speed range of $6 - 80$ km/s.

77 % of the events are recorded with impact speeds between $16 - 40$ km/s, and 21 % events for the range between $10 - 16$ km/s. In comparison, the relative impact speeds between IDPs in circular Keplerian orbits (i.e., α-particles) and the PSP are expected to be around $12 - 50$ km/s, which are within the range of this measurement. Note that impact events with speed ≥ 50 km/s, which are roughly the impact speed range of β-meteoroids (Szalay et al., 2020), are not well covered.

The results indicate two different scaling relations for two speed ranges, consistent with the surface versus volume ionization scenarios presented in Figure 3.2. In this measurement, events with impact speeds ≥ 16 km/s are considered to be in the volume ionization regime, while the rest of $10 - 16$ km/s may be under the transition or surface ionization regime. The former has a scaling relation of $4.3 \times 10^{-2}\, mv^{3.46}$, which is surprisingly comparable to metal targets, considering the impact-facing surface is non-conductive at room temperature. The latter, for completeness, requires more data points at low-speed ($1 - 10$ km/s). In addition, the measured charge yields are notably more scattered than those measurements with other materials commonly used on spacecraft (Collette et al., 2014). A hypothetical interpretation is that, due to the rough surface of the heat shield material, the impact ionization may be less uniform, so the assumption of $Q_i = |Q_e|$ may be invalid. For the purpose of PSP dust hazard investigation, more experiments in the hyper-speed impact regime are needed (e.g., impact speed ≥ 40 km/s).

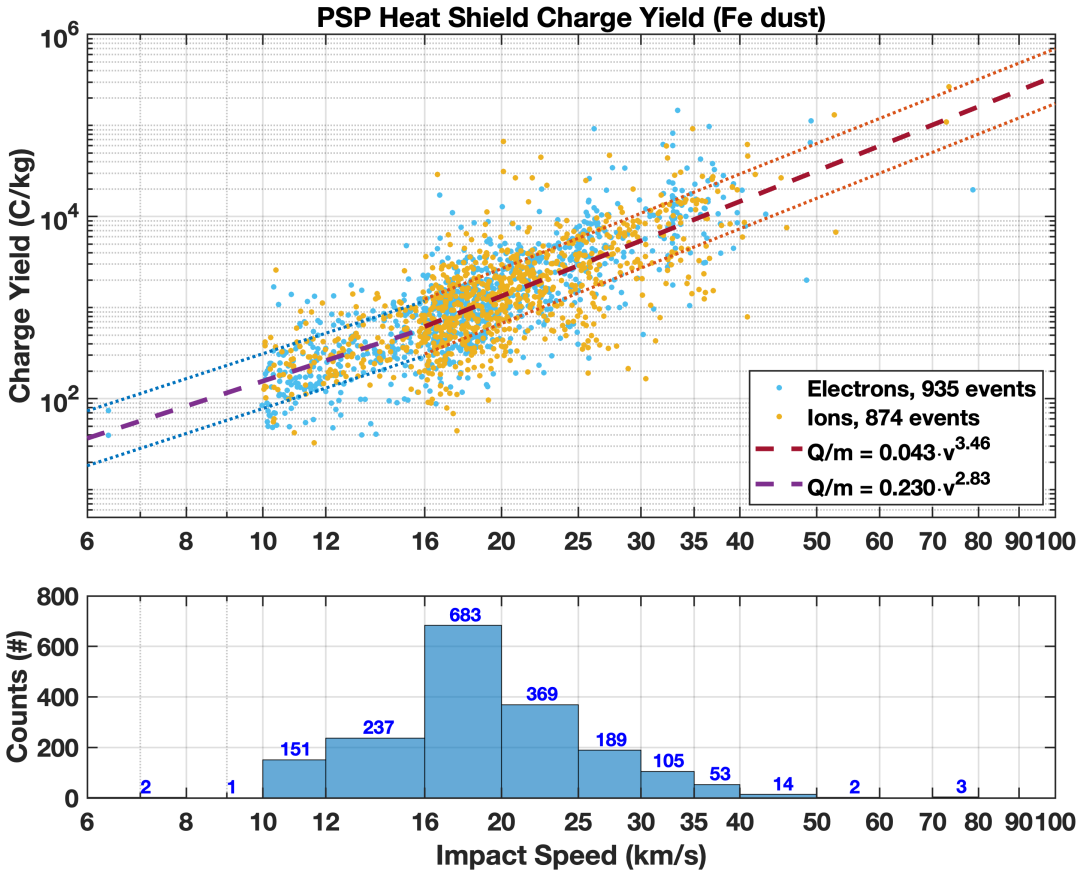

Figure 3.4: Impact charge yield measurement for iron dust impacting the heat shield sample designed for the *Parker Solar Probe*. The upper panel shows that the impact charge yield increases with impact speeds followed by two scaling relations, depending on the speed regimes. There are no significant differences between electron and ion charge yields, though both measurements show relatively large measurement deviations. The bottom panel shows the statistics of impact events, which mostly concentrate between $10 - 50$ km/s.

Chapter 4

Electrostatic Model

Dust impacts are detected as transient voltage signals generated by the expanding plasma cloud after impact ionization. These transient voltage signals (waveforms) measured by the antenna instruments can provide valuable information on dust particles. The antenna and SC acquire equilibrium potentials in space due to charging currents from photoelectron emission and the collection of electrons and ions from the ambient plasma. The equilibrium potential can be positive or negative (depending on the relative magnitude of the charging currents), and it will affect the expansion of the impact ionization plasma cloud. The dust impacts are registered as transient voltage perturbations imposed on top of the equilibrium potentials then relax back to the equilibrium values over timescales which are characteristic of the environment.

Having an appropriate generalized model to analyze and interpret these impact waveforms is crucial. The obtained parameters from fitting the model to measured waveforms can provide (1) information of dust particles, (2) characteristics of impact-generated plasma cloud, and (3) characteristics of ambient plasma environment. This chapter will first introduce the evolution of physical models and then provide our qualitative and quantitative model based on electrostatics. Note that the interpretation of waveforms in the following is limited to individual impact events.

4.1 Evolution of Antenna Detection Models

Several models have attempted to describe the physical mechanisms leading to the generation of voltage signals measured by antennas. Gurnett et al. (1983, 1987) assumed that a significant fraction (α) of the impact charge electrons is collected by the antennas with positive equilibrium potentials. As illustrated in Figure 4.1, the voltage measured by the antenna is then $V = Q \,/\, C_A$, where C_A is the capacitance of the antenna and the charge collected on antenna is $Q = \alpha\, Q_{IMP}$. In addition, Gurnett et al. (1987) considered the collection of the impact charge by the SC in the

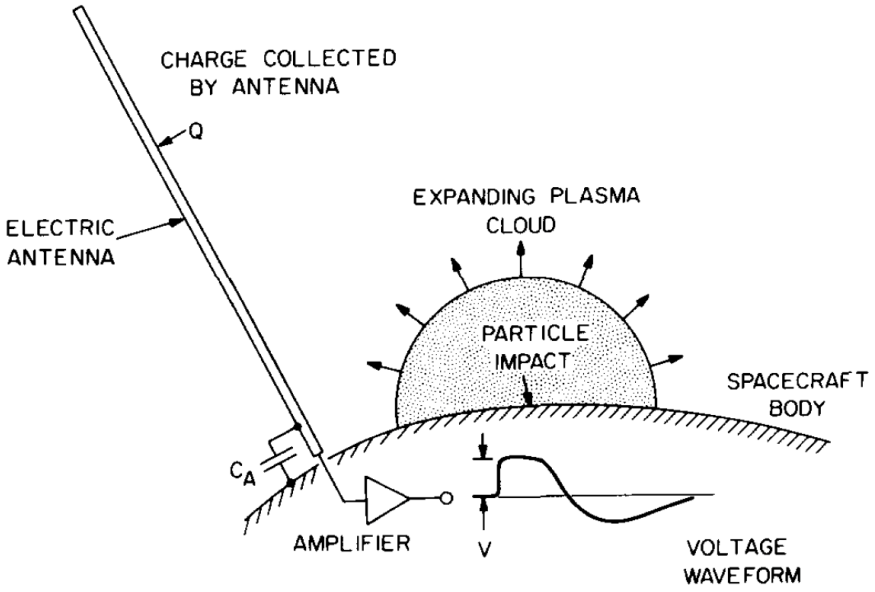

Figure 4.1: Schematic illustration of expanding plasma cloud generated upon dust impact, and the resulting charge Q collected by the electric antenna. Image Credit: Gurnett et al. (1983).

dipole mode, as the schematic provided in Figure 4.2. In this case, a small fraction of the SC voltage is measurable by the antennas, given as $V = \gamma\, Q_{IMP} \,/\, C_{SC}$, where C_{SC} is the SC capacitance, and γ is the common-mode rejection coefficient of the electronics.

In theoretical work, Oberc (1996) identified three mechanisms that can lead to the generation of voltage signals: (1) charging of the antenna, (2) charging of the SC, and (3) sensing of the charge separation electric field. The first two mechanisms are similar to the models described above. In

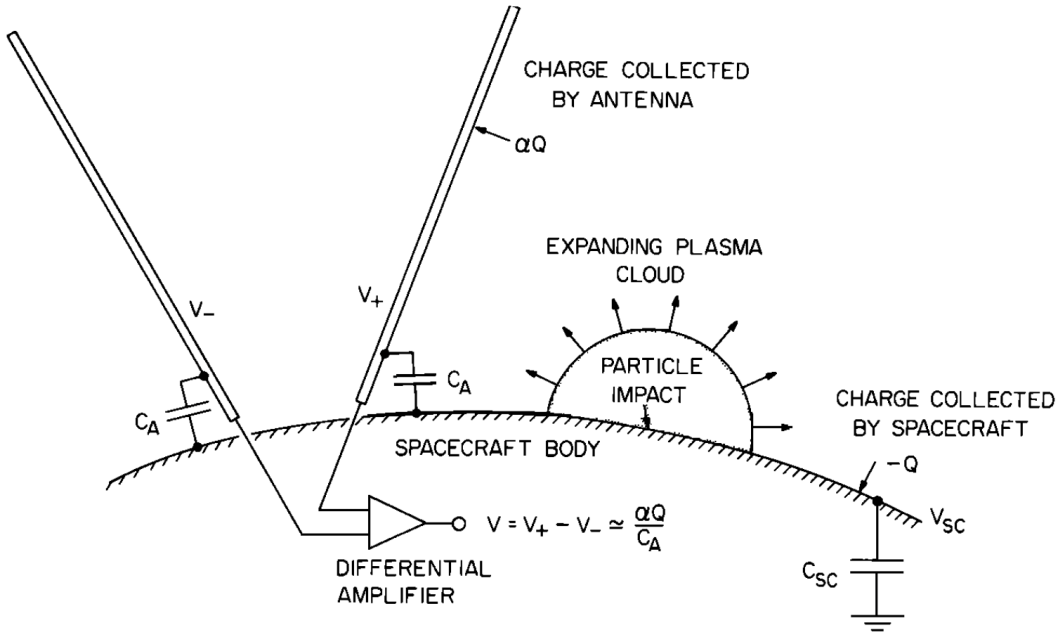

Figure 4.2: Schematic illustration of expanding plasma cloud generated upon impact detected by Voyager dipole antenna instrument. Image Credit: Gurnett et al. (1987).

the third one, the antennas are sensing the electric field of the ion cloud during the expansion of the impact plasma. The model assumes that the impact plasma is moving away from the impact location and simultaneously is expanding over time. At some point during the expansion, the electrons are decoupled from the plasma cloud, leaving behind the cloud of slower ions with a positive space charge potential on the order of the electron temperature expressed in the units of eV. The antennas then detect the separated electric field of the cloud. Oberc (1996) has pointed out that the measured signals generated by antenna charging would also strongly depend on the impact geometry, that is, the impact location relative to the geometry of the antennas and the SC. On the other hand, signals generated by spacecraft charging would be independent of the impact geometry. Oberc (1996) noted that for monopole antennas, the dominating mechanism is due to SC charging. For dipole antennas, the measured signals are from the differential charging of the two antennas and sensing the separated electric field. The relative importance between the latter two mechanisms depends on the physical characteristics of the antennas, such as their lengths.

Zaslavsky (2015) proposed the floating potential perturbation model for the data collected by the STEREO/WAVES instrument (Bale et al., 2008, Bougeret et al., 2008). This model assumes that both the SC and the antenna recollect some fraction of the impact plasma. The signal measured by the antenna is then the difference of the voltage perturbations on the antenna and the SC due to charge collection. The final characteristic shapes of the measured waveforms are set by the different discharge time-constants of the two elements through the ambient plasma. Meyer-Vernet et al. (2017) proposed an analytical model for calculating the risetime of antenna signals. This work pointed out several additional key aspects of the signal generation mechanisms. For example, the electrons in the impact plasma acquire an isotropic velocity distribution due to their high thermal speed; thus, half of the electrons move toward the spacecraft rather than away from it after charge separation. In addition, charge Q at a small distance from the surface of the SC will induce a potential with magnitude $\sim Q/C_{SC}$, i.e.; it has a similar effect as the same charge collected on the SC. Kellogg et al. (2018a,b) noted that there is capacitive coupling between the SC and the antenna elements. In addition, the base resistor installed in between these elements needs to be considered in determining the discharging time constant.

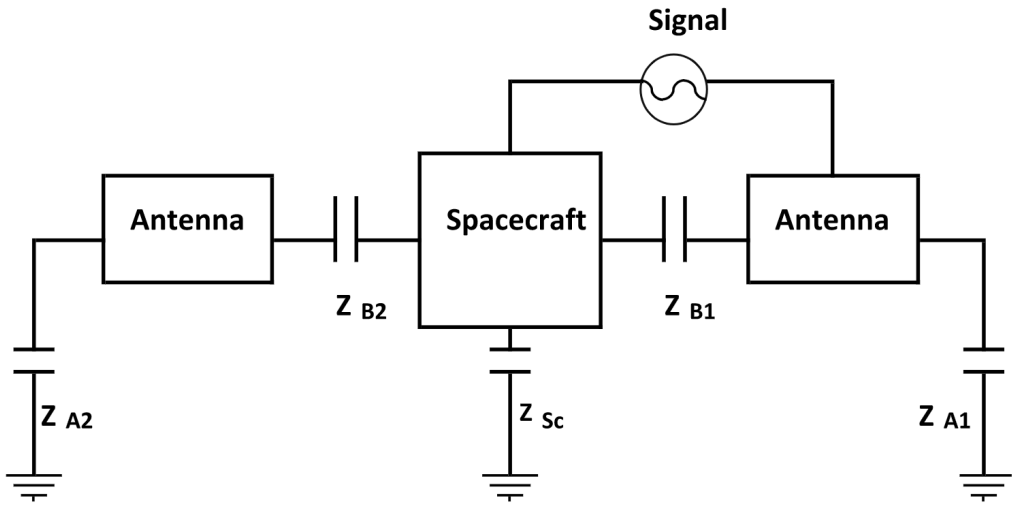

Figure 4.3: Schematic of time domain sampler circuit (denoted as "Signal") coupling to the spacecraft and antenna elements in impact signal detection. Image Credit: Kellogg et al. (2018b).

The investigation of the antenna signal generation processes in laboratory conditions was made possible by the dust accelerator facility at the University of Colorado (Shu et al., 2012). Using a simplified setup shown in Figure 4.4, Collette et al. (2015) identified three different signal generation mechanisms, namely (1) SC charging, (2) antenna charging, and (3) induced charging. The polarity of the SC and antenna charging signals can be reversed by changing the polarities of the applied bias voltages on the elements. Numerical analysis has later shown that charge

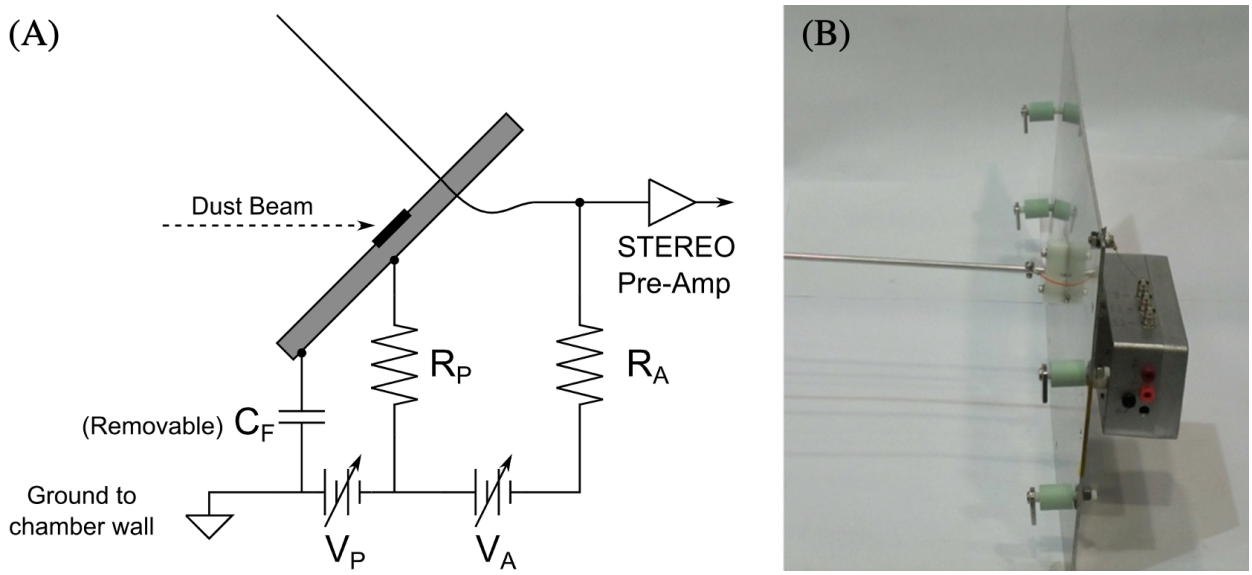

Figure 4.4: A simplified setup of antenna instrument for identifying signal generation mechanisms in laboratory conditions. In the left schematic panel, dust particles impact the tungsten target attached to the plate (simulated SC), generating an impact plasma. The right panel shows the picture. Image Credit: Collette et al. (2015).

collection by the antennas is effective only for dust impacts occurring in the close vicinity of the antenna base (O'Shea et al., 2017). For typical impacts analyzed for the STEREO SC and its antenna instruments, the collection efficiencies of the antenna themselves are only on the order of $0.1 - 1\%$. Nouzák et al. (2018, 2020) performed laboratory studies using a 20:1 scaled-down model of the Cassini SC and the Radio and Plasma Wave Science (RPWS) instrument, in both monopole and dipole modes (see Figure 5.5). The measured waveforms in the laboratory are in good qualitative agreement with those measured in space and demonstrated how the waveform

features vary with bias voltage on the SC. The measurements also confirmed that antennas in a dipole mode are relatively insensitive to dust impacts on the SC body (Ye et al., 2016b), and that of the magnetic field affects the recollection of electrons from the impact plasma considering the gyro motions (Ye et al., 2018).

The lab measurements collectively lead to a refined *qualitative* physical model for the generation of antenna signals that can be summarized as follows: The impact plasma, consisting of electrons and ions, can be divided into fractions recollected by the spacecraft or escape. The ratio of collected/escaping fractions of electrons and ions is determined by the SC potential and the effective temperatures of the respective species. The two main signal generation mechanisms are SC charging from the net recollected charge and induced charging from the escaping fraction. The characteristic waveforms are generated in four successive and somewhat overlapping steps. First, the fast escape of the electrons leaves behind a net positive charge on and near the SC, generating a steep, negative-going signal measured as $V_{ANT}(t) - V_{SC}(t)$. This feature is known as the 'preshoot,' which is commonly observed by antenna instruments that operate with sufficiently wide bandwidths and adequate sampling rates (e.g., O'Shea et al. (2017), Nouzák et al. (2018, 2020), Shen et al. (2021a,b)). Second, the escape of electrons is followed by that of ions, driving the signal more positive. Third, once the charge escape is completed, the SC is left with the net collected charge that is responsible for the main peak in the waveform. And fourth, the voltages on the SC and antennas relax back to their equilibrium values as the system is discharging through its ambient environment. This discharge process operates through the duration of the event and may significantly reduce the amplitude of the main peak (Shen et al., 2021a). The time constant of the discharge process is set by the magnitudes of charging currents from the environment (Zaslavsky, 2015). The description of the overall antenna signal generation processes is also provided in a review article by Mann et al. (2019).

In the following sections, we will introduce the *quantitative* analytical form of the model described above. It is first applied on a simplified system consisting of one antenna and a spherical SC (Section 4.3). The latter assumption allows expressing the induced charge on the SC in a simple

analytical form, $Q_{SC,ind}(t) = Q_{esc}\left(\frac{R_{SC}}{R_{SC}+r(t)}\right)$. Here, R_{SC} is the SC radius, $r(t) = vt$ is the radial distance of the charge escaping with velocity v, and the escaping charge Q_{esc} is approximated as a point charge moving radially outward (Jackson, 1999). The quantitative model provides good fits to the waveforms collected using a model SC. Several fundamental parameters of the impact plasma cloud are determined by fitting the model to the data, including the impact charge (Q_{IMP}), ion expansion speed, etc. Then, we expand this simplified model and generalize it for an arbitrary geometry of the SC−antenna system (Section 4.8). The model employs a capacitance matrix to calculate the voltages developed on the elements from the collected and induced charges. A new laboratory model SC has also been constructed to investigate the effects of the impact location on the waveforms. The model SC is spherical for simplicity and employs four antennas: two operated as monopoles and one dipole pair (Figure 5.5). The analysis of the dataset demonstrates that the electrostatic model can accurately describe waveforms measured in the laboratory using the dust accelerator (Chapter 6).

4.2 Collected and Escaping Charges

The generated impact charge is expressed as a power law of $Q_{IMP} = Q_i = |Q_e| = \gamma\, mv^{\beta}$, where m is the particle mass, and v represents impact speed. Parameters γ and β are characteristics of the target material, and their values can be determined from laboratory measurements, as listed in Table 3.1. In the first approximation, the impact plasma consists of electrons (Q_e) and cations (Q_i) in equal quantity. The next necessary assumption is that Q_{IMP} is reasonably small such that (a) it introduces only a relatively small perturbation to the equilibrium potential of the spacecraft (V_{SC}), and (b) the electrons and ions in the impact plasma decouple from one another (meaning that the electrons are no longer trapped by the positive space charge of the ion cloud) over a distance that is small compared to the characteristic size of the spacecraft (R_{SC}). The corresponding relations are $Q_{IMP} < C_{SC}V_{SC}$, and $Q_{IMP} < 4\pi\epsilon_0\frac{T_e}{e_0}R_{SC}$, respectively, where C_{SC} is the capacitance of the SC, T_e is the temperature of the electrons of the impact plasma (expressed in the units of eV), ϵ_0 is the permittivity of free space, and e_0 is the elementary charge. The faster electrons decouple from the

plasma soon as the space potential of the ion cloud drops below the electron temperature during the expansion. The corresponding assumption from above was derived by Meyer-Vernet et al. (2009) and O'Shea et al. (2017), and allows treating the ions and electrons independently (each expanding with their characteristic speed), as particles whose trajectories are mostly governed by the potential of the SC. For a typical SC operating near 1 AU in interplanetary space (e.g., Zaslavsky (2015)), and $T_e = 5$ eV, the above conditions are satisfied for impact charges $Q_{IMP} \lesssim 1 \times 10^{-9}$ C (Shen et al., 2021a).

The total impact charge, both the positive ion (i) and electron (e) parts, can be divided into fractions that are collected by the SC, and escaping from the SC, that is,

$$\begin{aligned} Q_i &= Q_{i,esc} + Q_{i,col} \\ Q_e &= Q_{e,esc} + Q_{e,col}. \end{aligned} \tag{4.1}$$

The collected and escaping fractions are determined by their effective temperatures (T_e and T_i in unit of eV), and the spacecraft potential. For $V_{SC} > 0$,

$$\begin{aligned} Q_{e,esc} &= -\kappa\, Q_{IMP}\, e^{\frac{-V_{SC}}{T_e}} \\ Q_{e,col} &= -Q_{IMP} - Q_{e,esc} \\ Q_{i,esc} &= Q_{IMP} \\ Q_{i,col} &= Q_{IMP} - Q_{i,esc} = 0. \end{aligned} \tag{4.2}$$

The third equation from 4.2 above expresses the assumption that ions are moving away from the impact location in form of a plume. On the other hand, the light and fast electrons acquire an isotropic velocity distribution through collisions during the early phases of the expansion. The geometric coefficient κ (with a value between 0 and 1) is introduced in order to account for the geometry of the SC body around the impact site. In an ideal case of a semi-infinite target and no obstructions in the field-of-view of the expansion, $\kappa = 1\,/\,2$ would account for the fact that half of the electrons are moving away from the SC and will be escaping, provided that it is energetically

feasible. For a negative spacecraft potential ($V_{SC} < 0$) the corresponding equations are:

$$\begin{aligned} Q_{e,esc} &= -\kappa\, Q_{IMP} \\ Q_{e,col} &= -Q_{IMP} - Q_{e,esc} \\ Q_{i,esc} &= Q_{IMP}\, e^{\frac{V_{SC}}{T_i}} \\ Q_{i,col} &= Q_{IMP} - Q_{i,esc}. \end{aligned} \tag{4.3}$$

The effective temperatures of the positive and negative charge carriers have been measured in laboratory conditions using a dust accelerator. The measurements by Collette et al. (2014), using iron (Fe) dust particles impacting onto a tungsten (W) target found that the effective temperatures of negative and positive charge carriers vary from $T_e = 1$ to 4 eV, and $T_i = 4$ to 20 eV, respectively, with increasing impact speed from 4 to 20 km/s. Nouzák et al. (2018) found T_e to be on the order of 1 eV, and T_i between $10 - 15$ eV for impact speed in the range of $20 - 25$ km/s using the same Fe/W dust-target material combination. In a more recent study by Kočiščák et al. (2020), using an organic-coated olivine dust sample impacting onto a W target, the authors found $T_i \approx 7$ eV over a wide impact speed range of $2 - 18$ km/s, while T_e varied between $1 - 10$ eV non-monotonically over the same impact velocity range. The authors suggested that the varying relative fraction of anions to free electrons is the reason for the significant variation observed for T_e. Olivine was selected for the study as a rock-forming mineral that is also common in meteorites, and the organic coating on the dust sample was applied in order to make the sample usable in the accelerator (Fielding et al., 2015).

The next step is to describe the temporal evolution of the antenna signal. We will first assume the simple case of a monopole configuration, where the antenna is far from the impact location and not in the way of the expanding plasma cloud. The antenna instrument measures the potential of the antenna with respect to the SC body. In space, both the antenna and the SC are at the equilibrium floating potentials, where the charging currents are in balance. The two dominant currents in interplanetary space are due to photoelectron emission and the collection of electrons from the ambient plasma (Zaslavsky, 2015), which result in floating potentials on the order of +5 V.

Since the electronics is AC-coupled, the monopole antenna measures the deviation in the potential differences due to the transient dust impact event, that is,

$$V_{meas}(t) = \delta V_{ANT}(t) - \delta V_{SC}(t). \tag{4.4}$$

4.3 Simplified Case Considering Spacecraft Charging Only

We will further assume a dust impact on the spacecraft body and that the antenna potential is not affected (see the Cassini SC model shown in Figure 5.5). In other words, the measured signal is simply the variation of the spacecraft potential, $V_{meas}(t) \cong -\delta V_{SC}(t)$. The spacecraft potential is related to charge on the spacecraft through its capacitance, that is, $\delta V_{SC}(t) = \delta Q_{SC}(t) \,/\, C_{SC}$. For completeness it is added that there is some capacitive coupling between the antenna and the SC. The consequence of such coupling is that the measured voltage is somewhat reduced, that is, $V_{meas}(t) \cong -\Gamma\, \delta Q_{SC}(t) \,/\, C_{SC}$, where Γ is known as a coupling parameter with a value between $0 - 1$. The extent of the capacitive coupling, however, has not been established experimentally for the simplified Cassini SC model setup, and for simplicity $\Gamma = 1$ is assumed.

The qualitative description of the spacecraft charging model is based on the works by Meyer-Vernet et al. (2017) and Nouzák et al. (2018, 2020), and its high-level description is also provided in Ye et al. (2019) and Mann et al. (2019). Briefly, a fraction of the electrons from the impact plasma (described in Equation 4.2 or Equation 4.3) escape quickly, resulting in a rapid positive charging of the spacecraft. The escape of the slower ions takes place simultaneously and it is charging the spacecraft negatively. Once the escape processes are completed, the spacecraft is left with the net collected charge of electrons and ions from the impact plasma. Throughout the process, the effect of the ambient plasma drives the spacecraft potential back to equilibrium. The following charging equation describes the transient event of a dust impact (occurring at time $t = 0$):

$$\delta Q_{SC}(t) = Q_{i,col} + Q_{e,col} + Q_{i,esc}\frac{R_{SC}}{R_{SC} + v_i t} + Q_{e,esc}\frac{R_{SC}}{R_{SC} + v_e t} + \int_0^t I_{dis}(\tau) d\tau. \tag{4.5}$$

This relation assumes that the generation of the impact charge is an instantaneous process. It is important to note that a small cloud of charge in the close vicinity of the SC has a similar

effect on its potential as the same charge collected on the SC. This is called induced charging. For this reason, the collection of the electron and ion charges by the SC ($Q_{e,col}$ and $Q_{i,col}$) can be considered to take place instantaneously, even though some of the electrons or ions are on ballistic orbits before returning to SC. For a spherical approximation of the spacecraft body (effective radius R_{SC}), the induced charges of the escaping fractions ($Q_{e,esc}$ and $Q_{i,esc}$) scale as $\sim 1\,/\,r$ with radial distance (Jackson, 1999), as expressed in the third and fourth terms on the right-hand-side of Equation 4.5. The characteristic expansion speeds of ions and electrons are v_i and v_e, respectively. The last term in Equation 4.5 accounts for discharging through the ambient plasma environment. Zaslavsky (2015) and O'Shea et al. (2017) derived the equations and the time constant of the discharge current for conditions, where the equilibrium spacecraft potential is maintained by the balance between photoelectron emission and electron collection from the ambient plasma environment (e.g., in interplanetary space). The corresponding discharge time-constant for an assumed spherical symmetry is

$$\tau_{dis} = \frac{1}{2}\frac{C_{SC}T_{ph}}{e_0 n_e w_e S_{SC}}, \tag{4.6}$$

where T_{ph} is the characteristic temperature of photoelectrons, n_e is the density of ambient plasma, S_{SC} is the surface area of the spacecraft, and $w_e = \sqrt{e_0 T_{e,ap}\,/\,2\pi m_e}$ is the electron thermal speed, with $T_{e,ap}$ and m_e being the temperature of the ambient plasma electrons and electron mass, respectively.

Differentiating Equation 4.5 and using Equation 4.1 we arrive to the transient charging equation in the following form:

$$\frac{d}{dt}(\delta Q_{SC}) = -Q_{i,esc}\frac{v_i R_{SC}}{(R_{SC}+v_i t)^2} - Q_{e,esc}\frac{v_e R_{SC}}{(R_{SC}+v_e t)^2} - \frac{Q_{SC}}{\tau_{dis}}. \tag{4.7}$$

This equation can be solved numerically.

4.4 Characteristics of Antenna Signals

4.4.1 Antenna Signals in Interplanetary Space

In this section, we illustrate the solution of the signal-generation model from above for an ideal spacecraft in interplanetary space. Specifically, we will consider the STEREO spacecraft at 1 AU and refer to the works by Zaslavsky (2015) and O'Shea et al. (2017). The relevant parameters considered are the following: The equilibrium floating potential of the spacecraft is $V_{SC} = 5.5$ V, the spacecraft capacitance is $C_{SC} = 200$ pF, the surface area is $S_{SC} = 10$ m^2, with an effective radius of $R_{SC} = 1$ m. The typical parameters of the plasma environment are $n_e = 5$ cm^{-3}, $T_{e,ap} = 8$ eV, and $T_{ph} = 2$ eV. For these condition $w_e = 0.47 \times 10^6$ m/s and $\tau_{dis} = 0.053$ ms. The following parameters are used to describe the impact plasma: $\kappa = 0.5$, $v_e = 10^6$ m/s, $v_i = 10^4$ m/s, $T_e = 7$ eV and $T_i = 25$ eV. The latter values will be justified in Section 6.1.

Figure 4.5 shows the antenna signal for a model spacecraft operating in interplanetary space near 1 AU by solving Equation 4.7. For simplicity, the impact charge is set to $Q_{IMP} = C_{SC}\,(1V) = 200$ pC. The sharp negative going feature is known as the "preshoot" and is generated by the rapid escape of free electrons from impact plasma, as it has been explained by Nouzák et al. (2018, 2020). The signal shape and characteristic time-constants are in good qualitative agreement with the "triple-hit" signals from the STEREO spacecraft described by Zaslavsky et al. (2012), Collette et al. (2015), or O'Shea et al. (2017).

A noteworthy observation in Figure 4.5 is that the amplitude of the signal is significantly lower than the $Q_{IMP}\,/\,C_{SC} = 1$ V value. Following Equation 4.2 and the parameters defined above, the escaping electron charge is $-0.23 \times Q_{IMP}$. However, the amplitude of the preshoot never reaches the full 0.23 V because the ions from the impact plasma are expanding simultaneously, albeit with a slower speed. Without discharge from the ambient plasma environment, the net collected charge on the SC after the plasma expansion is completed is $Q_{col} = Q_{e,col} + Q_{i,col} = -(Q_{e,esc} + Q_{i,esc}) = -0.77 \times Q_{IMP}$. Such collected charge would generate a signal with corresponding amplitude of 0.77 V. The actual amplitude, however, is significantly lower, only about 0.15 V. The reason for this

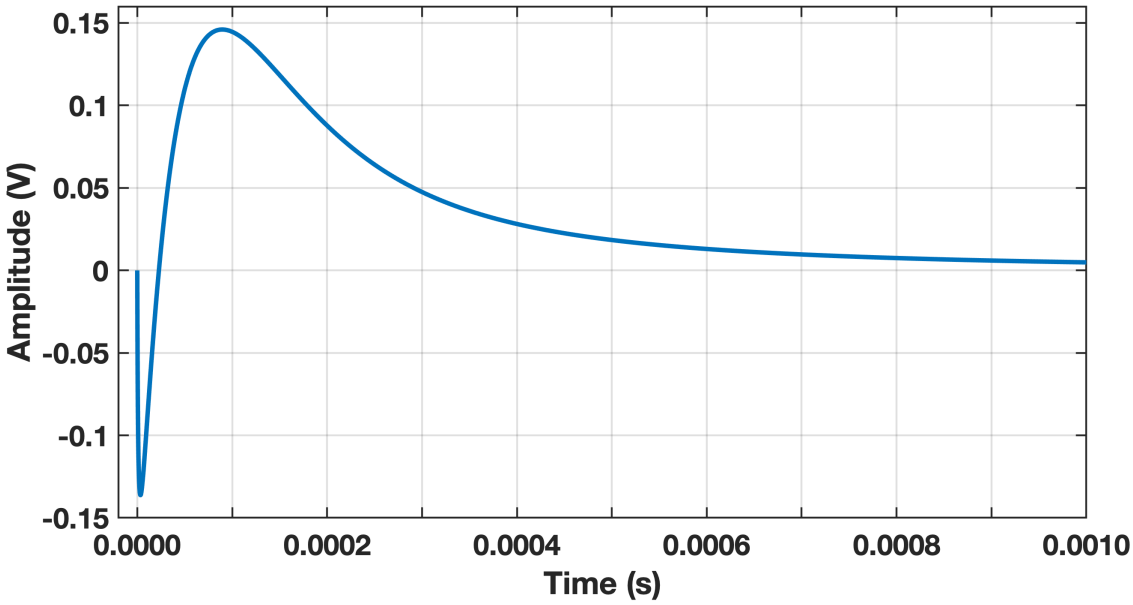

Figure 4.5: The antenna signal for a model spacecraft operating in interplanetary space near 1 AU. See text for more detail.

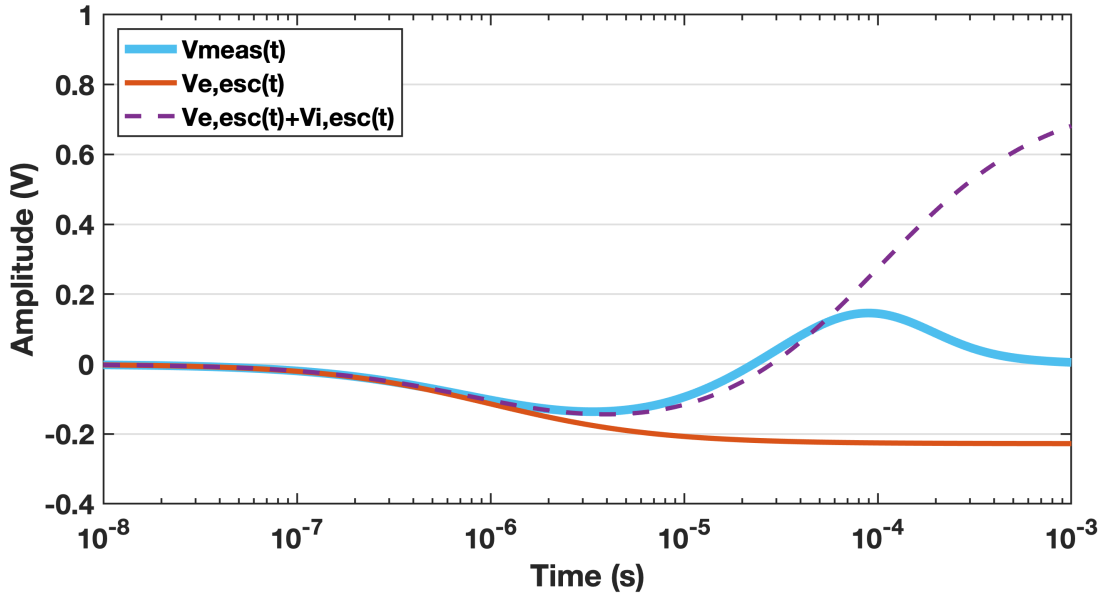

Figure 4.6: The antenna signal and contributions from selected terms on a logarithmic time scale. $V_{meas}(t)$ is the same as the measured signal shown in Figure 4.5. The red curve is the contribution from the escaping electrons, $V_{e,esc}(t)$ and the purple dashed curve represents the sum of signals from the escape of electrons and ions, $V_{e,esc}(t) + V_{i,esc}(t)$. The detailed list of parameters used for the calculations is shown in Table 4.1.

is the ongoing discharge from the ambient plasma, where the corresponding time-constant from Equation 4.6 is relatively short. Figure 4.6 shows the details of contributions from the escape of electrons ($V_{e,esc}(t)$) and ions ($V_{i,esc}(t)$) along with the measured voltage accounting for ambient discharging ($V_{meas}(t)$).

In summary, the simplified antenna signal model from Section 4.2 has three characteristic time constants: (1) electron escape is described by $\tau_{e,esc} = R_{SC} \,/\, v_e$, (2) ion escape by $\tau_{i,esc} = R_{SC} \,/\, v_i$, and (3) the plasma discharge time constant τ_{dis}. The amplitudes of the preshoot and the main signal are affected by the interplay between these competing effects. For the model case of a spacecraft in interplanetary space described above, the signal amplitude is significantly reduced compared to the theoretical maximum of $Q_{IMP} \,/\, C_{SC}$.

4.4.2 Antenna Signals in Laboratory Measurement

This section discusses the similarities and differences between the measurements in a controlled laboratory environment and those that can be expected in space. The discharge of the SC through the ambient plasma is modeled as a discharge through the biasing resistor (R_{BIAS}), as described by Nouzák et al. (2018). The corresponding discharge time constant, $R_{BIAS}\, C_{SC}$, is selected to be relatively long (a schematic of front-end electronic is provided in Figure 5.6), such that the amplitudes of the signals are not significantly affected, as demonstrated in Figure 4.7. Other than discharging, the ambient plasma has little effect on the expansion of the impact plasma and related charging processes. Provided that near 1 AU the Debye length of that ambient plasma is large compared to the characteristic size of the spacecraft, the potential profile around the spacecraft is not altered significantly by the plasma sheath.

The measurements and data analysis are limited to impact speeds $\geq$ 20 km/s (see Section 6.1), similarly to the work done by Nouzák et al. (2020). The goal is to demonstrate a simplified physical model from Section 4.3 can be used to explain the generated signal shapes. Generally, the parameters of the impact plasma, including ion composition, or the effective temperatures of positive and negative charge carriers, vary with impact speed. In particular, for $\geq$ 20 km/s volume

ionization is expected to dominate and the plasma consists mainly of electrons and atomic cations (Mocker et al., 2013, Hillier et al., 2014). In other words, the characteristics of the impact plasma from the described measurements are the closest to assumptions made for the signal generation model described above.

The laboratory measurements are performed using an Fe-W target-dust material combination such that the results are directly comparable to prior studies (Collette et al., 2015, 2016, Nouzák et al., 2018, 2020). The parameters determined from the experimental data described below may or may not be representative to cosmic dust particles with complex composition impacting onto spacecraft materials.

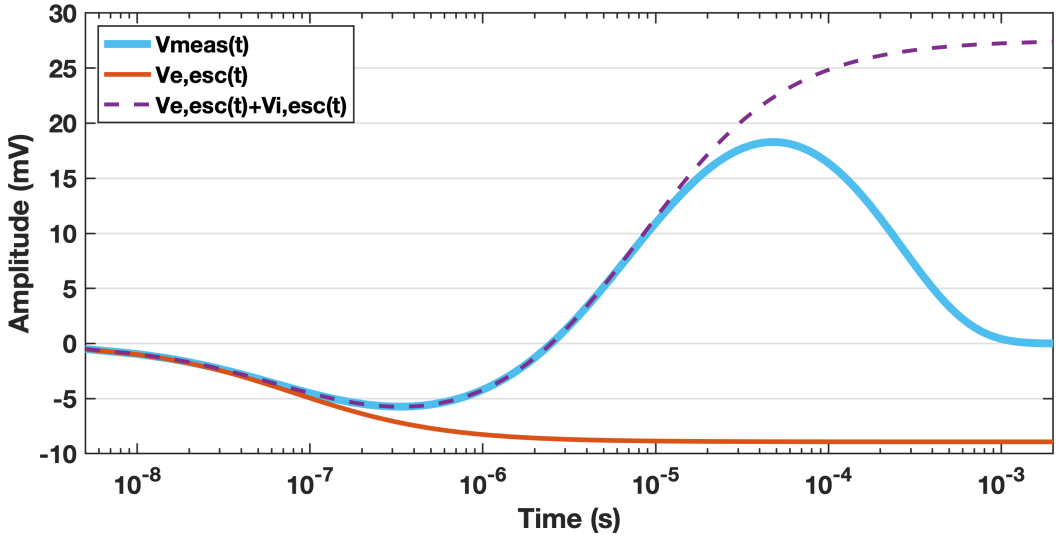

Figure 4.7: Same as Figure 4.6, except using the parameters of laboratory setup shown in Table 4.1.

Figure 4.7 shows the solution of Equation 4.7 for the parameters of the experimental setup and those determined from the lab measurements described below. Due to the smaller physical size of the model, both the preshoot and the main peak are shifted to earlier times. The amplitudes of the impact signals are also reduced due to the limited capabilities of the dust accelerator (Q_{IMP} is typically on the order of $10^{-14} - 10^{-15} C$). The comparison of typical values between a SC in interplanetary space and the laboratory model are presented in Table 4.1.

Table 4.1: The Parameter List of Calculated Antenna Signals Shown in Figures 4.6 and 4.7.

	Interplanetary space (Figure 4.6)	Laboratory model (Figure 4.7)
V_{SC}	$+5.5\,V$	$+5.0\,V$
Q_{IMP}	$2.0 \times 10^{-10}\,C$	$3.5 \times 10^{-14}\,C$
C_{SC}	200 pF	48 pF
R_{SC}	1.0 m	0.08 m
v_e	1,000 km/s	1,000 km/s
v_i	10 km/s	10 km/s
T_e	7 eV	7 eV
T_i	25 eV	25 eV
κ	0.50	0.50
τ_{dis}	$53\,\mu s\,(Equation\,4.6)$	$240\,\mu s = R_{BIAS}\,C_{SC}$
$\lvert Q_{e,esc}/Q_{IMP}\rvert$	0.23	0.24
$\lvert Q_{e,col}/Q_{IMP}\rvert$	0.77	0.76

4.5 Simplified Case Incorporating One Antenna

Here, the simplified yet illustrative example of a SC with one antenna is provided, considering only collected charges on one of the elements. Figure 4.8 depicts this case, where C_{SC} and C_{ANT} are the physical capacitances of the respective elements. The mutual capacitance, C_x, consists of several components. It includes the "base" capacitance (C_B), the capacitances of the cables and preamp input capacitance (C_{WP}), and the capacitance of the antenna to the SC body that is determined by the geometry of the system (C_G) (see, for example, Bale et al. (2008)). Since these three capacitances are effectively connected in parallel, $C_x = C_B + C_{WP} + C_G$.

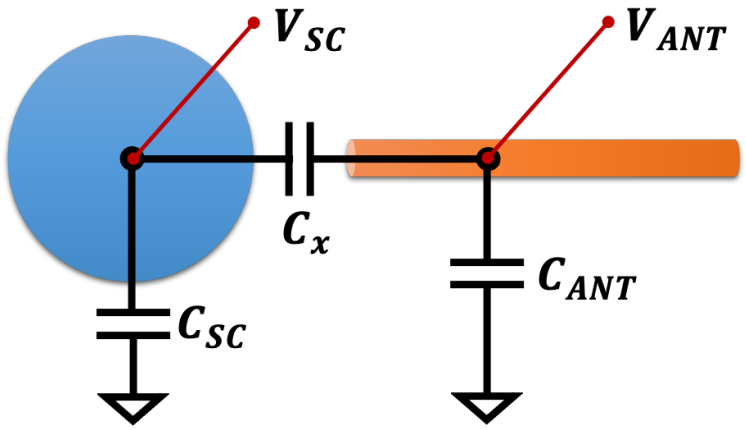

Figure 4.8: Schematics of the simple system consisting of a spacecraft (SC) and one antenna (ANT). See text for details.

The next step is considering that charge $\delta Q_{SC,col}$ is deposited onto the SC. The notation "δ" designates perturbation, that is, the deposited charge is in addition to that responsible for the development of the equilibrium potential. The voltage that develops on the SC is then given by $\delta V_{SC} = \delta Q_{SC,col} \,/\, C_{SC,eff}$, where $C_{SC,eff} = C_{SC} + \dfrac{C_x C_{ANT}}{C_x + C_{ANT}}$ is the effective capacitance of the SC that includes the contribution from C_{ANT} and C_x. Even though no charge is deposited onto the antenna, the voltage of these element is affected by the voltage on the SC. This voltage is given as $\delta V_{ANT} = \delta V_{SC}\,[C_x \,/\, (C_x + C_{ANT})]$, following the rule of capacitors connected in series. The voltage

measured between the antenna and the SC is then:

$$\delta V_{meas} = \delta V_{ANT} - \delta V_{SC} = -\frac{\delta Q_{SC,col}}{C_{SC,eff}} \frac{C_{ANT}}{C_x + C_{ANT}}. \tag{4.8}$$

The ratio at the end of Equation 4.8 is usually considered as the antenna gain, $G_A = C_{ANT} / (C_x + C_{ANT})$, corresponding to the description in Gurnett (1998) and Bale et al. (2008).

Similarly, for charge deposited on the antenna, the measured voltage is:

$$\delta V_{meas} = \delta V_{ANT} - \delta V_{SC} = \frac{\delta Q_{ANT,col}}{C_{ANT,eff}} \frac{C_{SC}}{C_x + C_{SC}}. \tag{4.9}$$

where $C_{ANT,eff} = C_{ANT} + \dfrac{C_x C_{SC}}{C_x + C_{SC}}$ is the effective capacitance of the antenna.

For the considered simplified cases, Equations 4.8 and 4.9 can be used to calculate the deposited charge from the amplitudes of the voltage signals. There are two noteworthy comments to make: One is that in the case of charge deposited onto the antenna, the antenna gain G_A is no longer applicable. The second is that contrary to common practice in previous studies, the effective values of the SC and antenna capacitances need to be used to convert charge to voltage and vice versa. When the SC−antenna system is immersed in plasma, the capacitances of the elements will increase. This effect is, however, negligible for conditions where the Debye length of the plasma is longer than the characteristic size of the SC, e.g., in interplanetary space near 1 AU.

4.6 The Matrix Form

The calculations of the effective capacitances and measured voltages increase complexity quickly with increasing the number of antennas. Fortunately, Maxwell's capacitance matrix can be employed to keep track of how the SC and the antenna elements interact (Maxwell, 1873). For n antennas, the matrix form can be written as

$$\begin{bmatrix} \delta V_{SC} \\ \vdots \\ \delta V_{ANT,n} \end{bmatrix} = \begin{bmatrix} a_{00} & \cdots & a_{0n} \\ \vdots & \ddots & \vdots \\ a_{n0} & \cdots & a_{nn} \end{bmatrix} \begin{bmatrix} \delta Q_{SC,col} \\ \vdots \\ \delta Q_{ANT,n,col} \end{bmatrix}, \tag{4.10}$$

which allows calculating the voltages on objects from known collected charges. In this form, $[\boldsymbol{a}]$ is the elastance matrix with $(n+1)^2$ elements. The inverse form to Equation 4.10 is $[\delta Q] = [\boldsymbol{b}]\,[\delta V]$,

where $[\boldsymbol{b}] = [\boldsymbol{a}]^{-1}$ is the Maxwell capacitance matrix (Maxwell, 1873, Di Lorenzo, 2011, de Queiroz, 2012). For the remainder of this section, it will be assumed that the elastance and capacitance matrices are known for the system. Section 5.4 below will provide the details of how the matrices can be calculated.

Here, we present illustrative exercise calculations for the simplest case of a SC with one antenna that demonstrates: (1) the capacitance matrix is properly tracking the effective capacitance of the system, and (2) the physical meaning of the elastance matrix. The potential of elements of the simple SC–antenna system is written using the elastance matrix $[\boldsymbol{a}]$:

$$\begin{bmatrix} \delta V_{SC} \\ \delta V_{ANT} \end{bmatrix} = \begin{bmatrix} a_{00} & a_{01} \\ a_{10} & a_{11} \end{bmatrix} \begin{bmatrix} \delta Q_{SC,col} \\ \delta Q_{ANT,col} \end{bmatrix}. \tag{4.11}$$

The charge can be calculated from the voltage using the inverse form,

$$\begin{bmatrix} \delta Q_{SC} \\ \delta Q_{ANT} \end{bmatrix} = \begin{bmatrix} b_{00} & b_{01} \\ b_{10} & b_{11} \end{bmatrix} \begin{bmatrix} \delta V_{SC} \\ \delta V_{ANT} \end{bmatrix} = \begin{bmatrix} C_{SC} + C_x & -C_x \\ -C_x & C_{ANT} + C_x \end{bmatrix} \begin{bmatrix} \delta V_{SC} \\ \delta V_{ANT} \end{bmatrix}, \tag{4.12}$$

where $[\boldsymbol{b}] = [\boldsymbol{a}]^{-1}$ is the capacitance matrix. The right-hand side of the equation above demonstrates the physical meaning of the elements (also see $[\boldsymbol{b}]$ in Section 5.4 and Equation 5.5). The charges on the SC and the antenna can be expressed as:

$$\begin{aligned} \delta Q_{SC} &= (b_{00} + b_{01})\delta V_{SC} + b_{01}(\delta V_{ANT} - \delta V_{SC}) \\ \delta Q_{ANT} &= b_{10}(\delta V_{SC} - \delta V_{ANT}) + (b_{11} + b_{10})\delta V_{ANT}, \end{aligned} \tag{4.13}$$

where the potential differences between the SC and antenna are introduced. By substituting for the physical meaning of the matrix elements from Equation 4.12, we obtain:

$$\begin{aligned} \delta Q_{SC} &= C_{SC}\,\delta V_{SC} + C_x(\delta V_{SC} - \delta V_{ANT}) \\ \delta Q_{ANT} &= C_x(\delta V_{ANT} - \delta V_{SC}) + C_{ANT}\,\delta V_{ANT}, \end{aligned} \tag{4.14}$$

This set of equations can be solved when the charge is deposited only onto the SC, i.e., $\delta Q_{ANT} = 0$. Expressing $\delta V_{ANT} = \delta V_{SC}\,[C_x\,/\,(C_x + C_{ANT})]$ from the second equation and substituting to the first, we obtain:

$$\delta Q_{SC} = C_{SC}\,\delta V_{SC} + C_x\left(\delta V_{SC} - \frac{C_x}{C_x + C_{ANT}}\delta V_{SC}\right). \tag{4.15}$$

And from here the effective capacitance is obtained as:

$$\frac{\delta Q_{SC}}{\delta V_{SC}} = C_{eff,SC} = C_{SC} + \frac{C_x C_{ANT}}{C_x + C_{ANT}}. \tag{4.16}$$

The effective capacitance of the antenna can be calculated similarly.

The last thing to demonstrate is the physical meaning of the diagonal terms of the elastance matrix. Following the rules of matrix transformation, we obtain from Equation 4.12:

$$[\boldsymbol{a}] = \frac{1}{(C_{SC} + C_x)(C_{ANT} + C_x) - C_x^2} \begin{bmatrix} C_{ANT} + C_x & C_x \\ C_x & C_{SC} + C_x \end{bmatrix}. \tag{4.17}$$

It can be shown easily from here that $a_{00}^{-1} = C_{eff,SC}$ and $a_{11}^{-1} = C_{eff,ANT}$, as those two effective capacitances described in previous Section 4.5. In other words, the diagonal elements conveniently provide effective capacitances for each element of the system.

4.7 Induced Charging and Geometric Function

Induced charging refers to the fact that a free charge in the vicinity of a conductive object will induce a potential on this object. An analytical solution for the established potential exists for the simple case of a spherical object, where the magnitude of the induced potential scales as $\sim 1/r$ with radial distance from the surface (see Section 4.3 and Jackson (1999)). We have presented the analytical solution for this simple case with the SC in the spherical approximation in Equation (4.5) and (4.7).

The general solution for induced charging for the SC and the antenna elements can be calculated numerically, provided that the geometry of the system and the charge distribution are known. In order to describe the fraction of the charge induced on the i-th element from a test point charge (Q_{test}) located at position $\vec{r}$, the *geometric function* is introduced. For the system of a SC and n antennas, the geometric functions are defined as:

$$\begin{aligned} g_{SC}(\vec{r}) &= \frac{Q_{SC,ind}(\vec{r})}{Q_{test}} \\ g_{ANT,n}(\vec{r}) &= \frac{Q_{ANT,n,ind}(\vec{r})}{Q_{test}}, \end{aligned} \tag{4.18}$$

where $Q_{SC,ind}(\vec{r})$, for example, is the charge induced on the SC, while the unit point charge is located at $\vec{r}$. The geometric functions provide unitless values and sum up to $g_{SC}(\vec{r}) + \sum_n g_{ANT,n}(\vec{r}) \leq 1$ for all locations. The value of the geometric function approaches unity for a point charge in the close proximity to one of the elements and diminishes with increasing distance.

The geometric functions can be calculated numerically using standard available electrostatic solver tools (e.g., commercial software like COMSOL Multiphysics, CST Studio Suite, or COULOMB). The geometry of the SC−antenna system is imported into the software, and each element of interest is treated as a conductive object that is electrically isolated from the rest of the system. The software also calculates the elastance and/or capacitance matrices. The values of the geometric functions can be calculated simply from the voltages established on each element using the following relation:

$$\begin{bmatrix} g_{SC}(\vec{r}) \\ \vdots \\ g_{ANT,n}(\vec{r}) \end{bmatrix} = \frac{1}{Q_{test}} \begin{bmatrix} b_{00} & \cdots & b_{0n} \\ \vdots & \ddots & \vdots \\ b_{n0} & \cdots & b_{nn} \end{bmatrix} \begin{bmatrix} V_{SC} \\ \vdots \\ V_{ANT,n} \end{bmatrix}, \tag{4.19}$$

The calculation of the geometric function can be performed for all locations of interest in the vicinity of the system. The capacitance matrix in the equation above can account only for the geometric coupling between the elements, i.e., $C_x = C_G$. The description of how to account for the additional contributions from C_B and C_{WP} is described in Section 5.4. Given the size and complexity of an actual SC−antenna system and the required resolution, the numerical calculations of the geometric function can be numerically demanding. However, these calculations have to be performed only once and then use standard numerical techniques, e.g., lookup tables combined with linear interpolation for determining the values for arbitrary positions.

Figure 4.9 shows the numerical calculations for a simplified case of a spherical model SC with one antenna. The dimensions of the system resemble those of the model used in the laboratory measurements described in Section 5.2. The SC radius is $R_{SC} = 7.62$ cm, and the antenna is 27 cm long and 1.6 mm in diameter. In the model setup, there is a 5 mm gap between the surface of the SC and the antenna, which limits their mutual coupling. The point charge is moving along a radial line that is offset 10° from the antenna, as illustrated in the insert of Figure 4.9. The

magnitude of the test point charge is $Q_{test} = 100$ pC. The left panel shows the potentials on each element, and their difference, $V_{meas} = V_{ANT} - V_{SC}$. When the test point charge is near the surface of the SC, the potentials are $V_{SC} \cong Q_{test}/C_{SC,eff} = 10.8$ V, where $C_{SC,eff} = 9.60$ pF is the effective SC capacitance, as calculated. This is close to the expected value of $C_{SC,eff} = C_{SC} + \dfrac{C_x C_{ANT}}{C_x + C_{ANT}} = 9.46$ pF, where $C_{SC} = 4\pi\varepsilon_0 R_{SC} = 8.47$ pF is the capacitance of the SC, and the values of $C_x = 1.43$ pF and $C_{ANT} = 1.84$ pF are also from the numerical calculations. With the point charge near the surface of the SC, the potential of the antenna is $V_{ANT} \approx 4.6$ V, which is close to the value calculated as $V_{ANT} = V_{SC}\,[C_x\,/\,(C_x + C_{ANT})] = 4.7$ V. The minor discrepancies in the calculated and theoretical values are likely due to numerical errors (e.g., grid or numerical setup in the software).

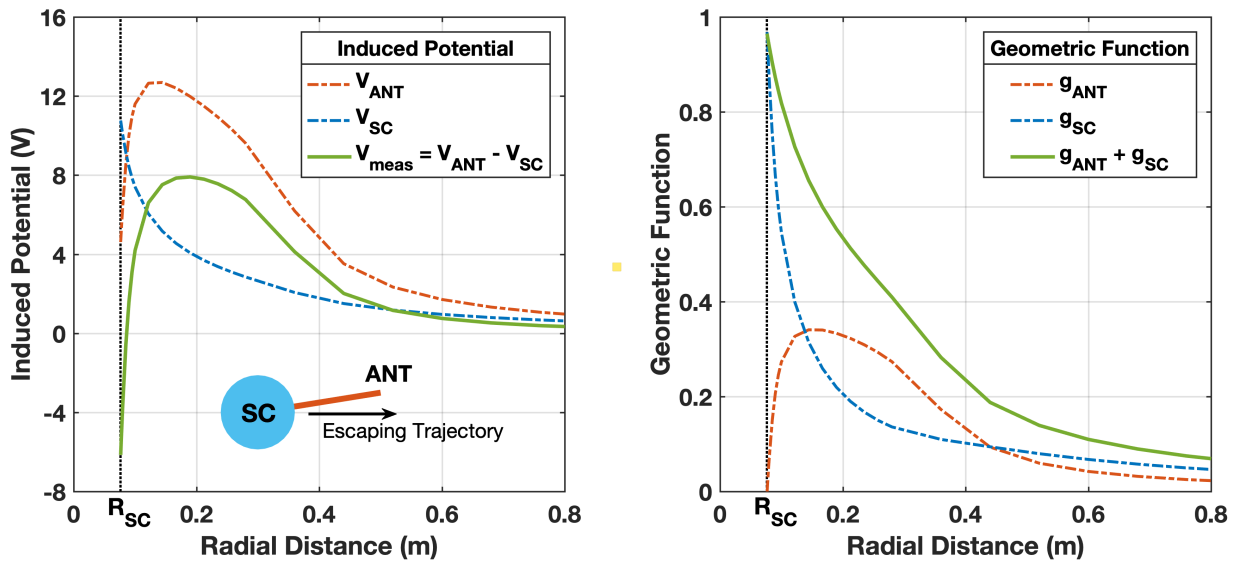

Figure 4.9: The induced potential (left panel) and the geometric function (right panel) for a simple case of a system consisting of a spherical SC and one antenna. The numerical calculations are for a test point charge ($Q_{test} = 100$ pF) moving radially outward on a trajectory offset by 10° from the antenna (see the illustration in the left panel).

The right panel in Figure 4.9 shows the variation of the values of the geometric function with radial distance. $g_{SC}(r)$ is close to unity for the point charge located near the surface and then drops quickly with increasing distance. In the case investigated, this drop is steeper than $1/r$ because of

the proximity of the antenna to the point charge since a significant fraction of the induced charge will occur on the antenna rather than the SC. The value of $g_{ANT}(r)$ increases quickly over a few mm distance as the point charge gets close to one end of the antenna. There is a noticeable drop in $g_{ANT}(r)$ at around radial distance $r = R_{SC} + 0.27 \cong 0.35$ m, where the antenna ends.

4.8 Full Model Expression for Arbitrary Spacecraft-Antennas System

The analytical model for a simplified case presented in Equation 4.5 calculated the time evolution of the charge on the SC in the form of

$$\delta Q_{SC}(t) = Q_{SC,col} + \sum_{s=e,i} Q_{esc,s}\left(\frac{R_{SC}}{R_{SC} + v_s t}\right) + \int_0^t I_{dis}(\tau)\, d\tau. \tag{4.20}$$

The collected charge is the sum of collected electrons and cations, $Q_{SC,col} = Q_{e,col} + Q_{i,col}$, using Equations 4.2 and 4.3. The second term accounts for the induced charging from the escaping fractions of electrons and ions from the impact plasma. The simplifying assumptions used here are the spherical approximation of the SC. The escape of the electrons and ions can be effectively approximated as a point charge moving radially outward with their respective characteristic escape speeds (v_s, $s = e, i$). The last term in Equation 4.20 accounts for the discharge current. The discharge current is due to the applied bias resistor for the case of the laboratory model and due to the charging environment for a SC operating in space. As the potential of the SC deviates from equilibrium due to charging from the dust impact plasma, the imbalance of the electron, ion, and photoelectron currents will drive the body back towards equilibrium (e.g., Zaslavsky (2015)). Once the charging of the SC is calculated, the potential perturbation from the dust impact plasma is obtained as $\delta V_{SC}(t) = \delta Q_{SC}(t) \,/\, C_{SC,eff}$.

Here we generalize the simplified analytical model from Equation 4.20 by employing the capacitance matrix and geometric functions introduced above. The fundamental property of the model is that recollected and induced charges can be treated similarly when it comes to calculating the potential on the elements. The voltage perturbations on the spacecraft and $n-$th antennas can

be calculated simultaneously in the following form:

$$\begin{bmatrix} \delta V_{SC}(t) \\ \vdots \\ \delta V_{ANT,n}(t) \end{bmatrix} = \begin{bmatrix} a_{00} & \cdots & a_{0n} \\ \vdots & \ddots & \vdots \\ a_{n0} & \cdots & a_{nn} \end{bmatrix} \begin{bmatrix} Q_{SC,col} + \int_V \rho_{esc}(\vec{r},t) g_{SC}(\vec{r})\, dV + \int_0^t I_{SC,dis}(\tau) d\tau + \sum_{n=1}^{n} \int_0^t \frac{\delta V_{ANT,n}(\tau) - \delta V_{SC}(\tau)}{R_{base}} d\tau \\ \vdots \\ Q_{ANT,n,col} + \int_V \rho_{esc}(\vec{r},t) g_{ANT,n}(\vec{r})\, dV + \int_0^t I_{ANT,n,dis}(\tau) d\tau - \int_0^t \frac{\delta V_{ANT,n}(\tau) - \delta V_{SC}(\tau)}{R_{base}} d\tau \end{bmatrix}. \tag{4.21}$$

The elements of the charge vector on the right-hand side are similar to those presented in Equation 4.20. The first term is the collected charge. The second term provides the induced charging from the escaping charges in form of a volume charge distributions, $\rho_{esc}(\vec{r},t) = \rho_{esc,e}(\vec{r},t) + \rho_{esc,i}(\vec{r},t)$, which accounts for both electrons and ions. This is the most general form that allows incorporating models of electrons and ion escaping, for example, by considering the initial velocity distributions and plume shapes of the respective species. The geometric functions in the integral enable considering the impact location with respect to the geometry of the SC and the antennas. The third term is the discharge from the ambient environment. A fourth term is introduced, recognizing that the antennas and the spacecraft are electrically connected through a base resistance, R_{base} (see, for example, Bale et al. (2008)). This connection allows a current to flow and reduce the potential difference between the SC and the antennas. This last term may or may not be significant in comparison to the discharge through the environment, depending on the value of R_{base} (typically on the order of $M\Omega$), the density of the ambient plasma, and the distance to the Sun, which would drive the photoelectron emission current.

Chapter 5

Experimental Facility and Measurement Setup

A linear electrostatic dust accelerator is a unique facility that can support various impact research activities and calibrate dust instruments for space applications. Micron and sub-micron dust particles of various materials can be accelerated to velocities in the range of $1 - 100$ km/s (Shu et al., 2012). Figure 5.1 shows the dust accelerator facility at the University of Colorado, and Figure 5.2 depicts the schematic diagram. The accelerator allows simulating the high-speed range of bound grains and beta-meteoroids in space but with smaller sizes. Other techniques, such as a light-gas gun or plasma drag accelerator, can provide impact measurement of micro-meteoroids and meteoroids but are constrained by the speed range of $\lesssim 15$ km/s (Auer, 2001). Section 5.1 introduces the characteristics and capability of the dust accelerator facility. Section 5.2 provides the descriptions of two SC models, including a scaled-down Cassini model and a spherical model. The integrated electronics and circuit performance are described in Section 5.3. Section 5.4 introduces how the specific capacitance matrices are constructed for laboratory conditions and space applications. Finally, a simulation of induced charging for the model spacecraft is provided as the dataset for (1) deriving geometric functions (introduced in Section 4.7) and (2) fitting the model to laboratory measurements (shown in Section 6.2).

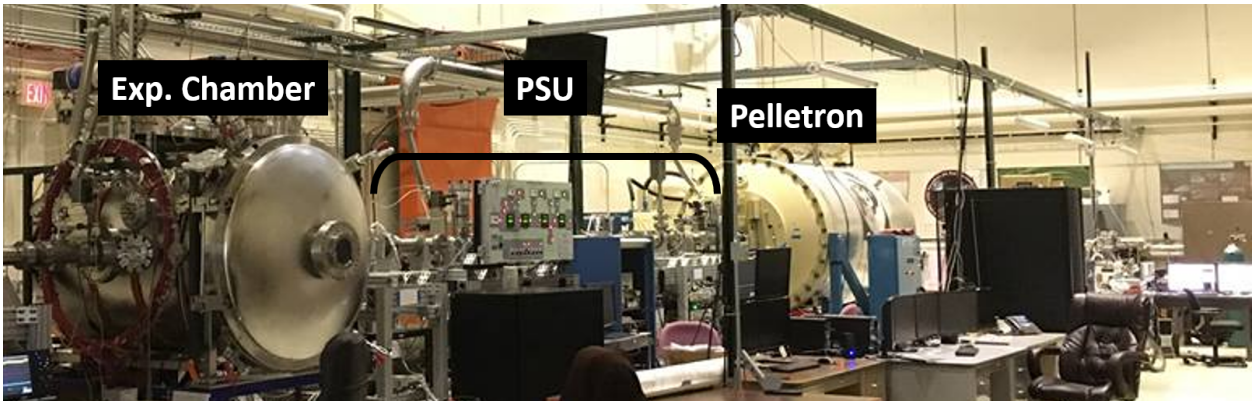

Figure 5.1: Picture of the dust accelerator facility at the University of Colorado Boulder. The dust grains launched from the pelletron and pass the gates of the particle selection unit (PSU) to the experimental chamber.

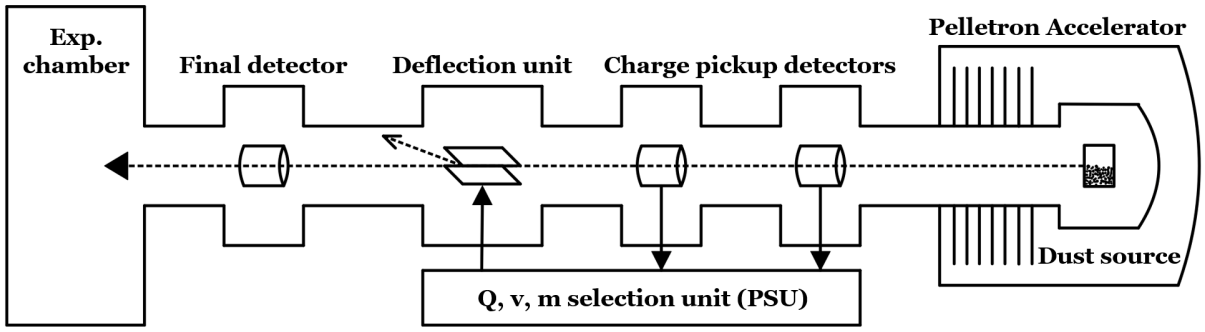

Figure 5.2: Schematic diagram of the dust accelerator facility. The orientation is consistent with Figure 5.1. The dust source is housed inside the pelletron dome. The particle selection unit (PSU) consists of a pair of pickup detectors and a deflection unit. See text for detail.

5.1 Dust Accelerator Facility

The schematic and photo of the pelletron accelerator are provided in Figures 5.2 and 5.3. High voltage pulses are generated in the dust source cavity, making the dust particles be levitated, charged, and ejected away from the source region (Shu et al., 2012, Mocker et al., 2013). Then, these dust particles will be accelerated to high speeds ($\geq$ 1 km/s) through the high electrostatic potential of $2-3$ MV produced by the pelletron.

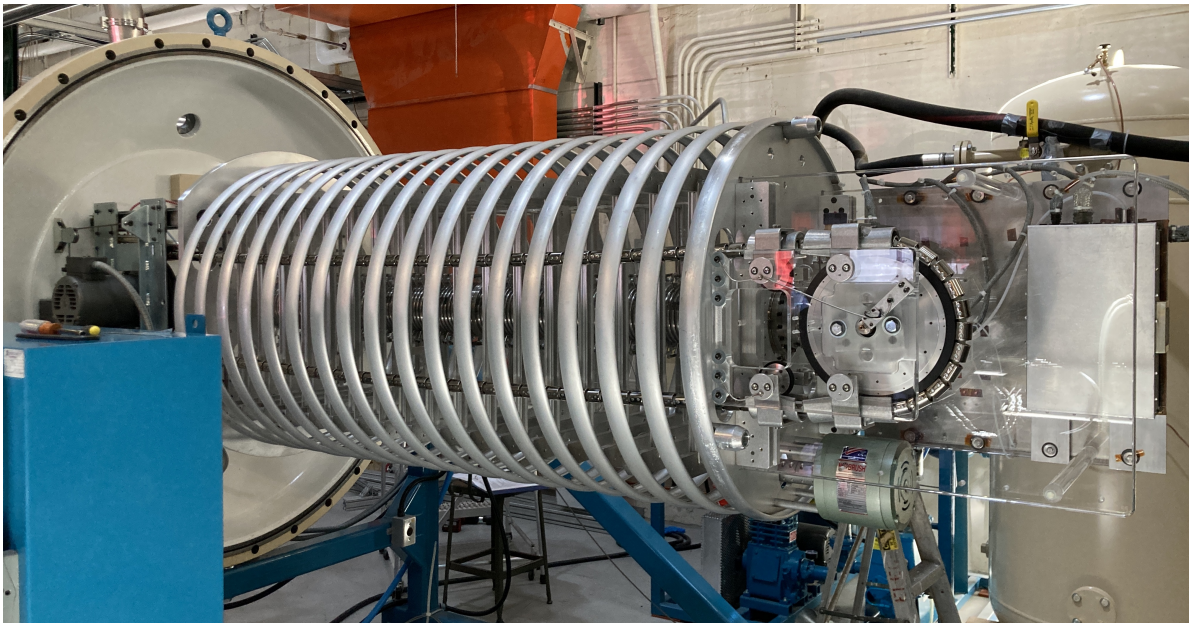

Figure 5.3: The pelletron is housed with a dust source (right-hand side) and acceleration regime (rings region).

A pair of charge pickup tube detectors is placed to measure the charge and velocity of individual dust particles (Figure 5.2). The dust charge is detected through its image charge on the pickup tube, while the velocity is calculated from the time of flight between the detectors. Combining with a deflection unit, the particle selection unit (PSU) allows dust particles within the desired range of velocity and charge to enter the experimental chamber. The experimental chamber is 1.2 m in diameter and 1.5 m long and is capable of evacuating to $< 10^{-6}$ Torr for the measurements.

The parameters of individual dust particles are determined when leaving the pelletron accelerator. The velocity of a dust particle (v_d) can be measured through PSU and follow the energy equation, expressed as

$$v_d = \sqrt{\frac{2\,Q_d\,U_p}{m_d}}, \tag{5.1}$$

where U_p is the electrostatic potential of the pelletron ($2-3$ MV), Q_d is the particle charge, and m_d is the particle mass. By rearranging Equation 5.1, the mass of the dust particle is then calculated through known values of Q_d and v_d:

$$m_d = \frac{2\,Q_d\,U_p}{v_d^2}. \tag{5.2}$$

In addition, the radius of a dust particle (R_d) can be estimated using a spherical approximation, written as

$$R_d = \sqrt[3]{\frac{3\,Q_d\,U_p}{2\pi\rho\,v_d^2}}, \tag{5.3}$$

where ρ is the particle mass density.

Following Equations (5.2) and (5.3), the mass and radius of the dust particles are proportional to ${v_d}^{-2}$ and ${v_d}^{-2/3}$, respectively. A distribution plot with mass, radius and velocity of dust particles in logarithmic scale is then provided in Figure 5.4. This plot demonstrates the experimental capability of the dust accelerator. The charging of a dust particle follows $Q_d \propto {R_d}^2$ while its mass follows $m_d \propto {R_d}^3$. Since the speed is a function of the charge to mass ratio of dust particles, the faster particles are the smallest size and mass (Shu et al., 2012). The equation is given as

$$v_d \propto \sqrt{\frac{Q_d}{m_d}} \propto {R_d}^{-\frac{1}{2}}. \tag{5.4}$$

The most common dust materials are spherical iron particles, ranging in size from ~ 30 nm $-$ 2 μm in radius. Alternative metallic particles such as aluminum and silver have also been applied in various experiments. Furthermore, insulating particles of olivine with surface coated by a thin layer of conductive organic polymer (Polypyrrole) have been performed for specific measurements (Kočiščák et al., 2020). In this thesis, impact events with iron and aluminum dust materials have been collected in laboratory measurements. The data analysis of signal variations of dust compositions is provided in Section 6.6.

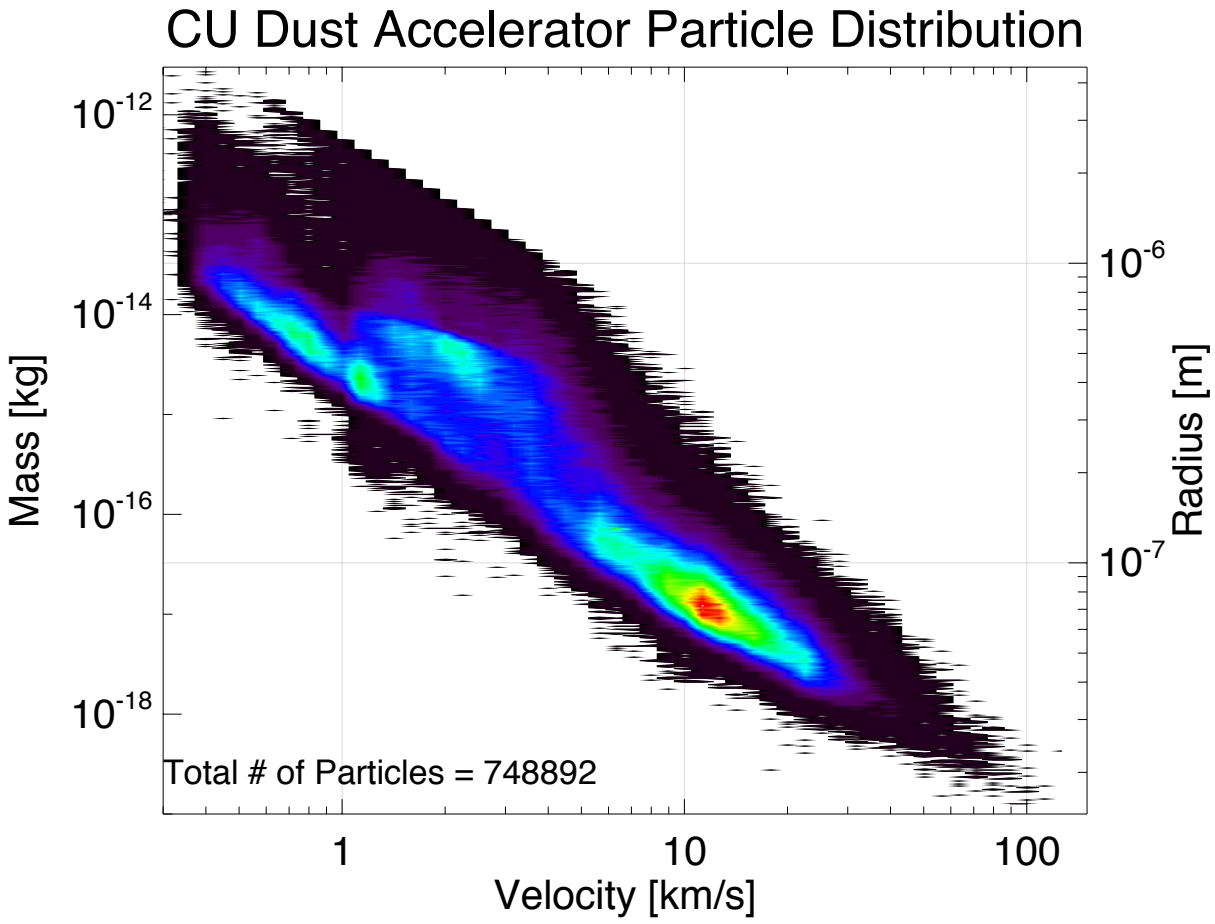

Figure 5.4: Density distribution of mass, radius, and velocity of dust accelerator facility at the University of Colorado. The dust velocity ranges from $\sim$ 300 m/s to about 100 km/s.

5.2 Model Spacecrafts for Laboratory Studies

5.2.1 Spacecraft Models

Two spacecraft models have been constructed for laboratory measurements: a scaled-down Cassini model and a spherical SC model.

The first measurements were performed using the reduced-size model of the Cassini spacecraft described in detail by Nouzák et al. (2018). Briefly, in Figure 5.5 (a), the simplified 20:1 scaled model consists of a cylindrical body, the high gain antenna (HGA), the magnetometer boom (MAG), and three orthogonal antennas, denoted as E_U, E_V, and E_W. The aluminum body is coated with graphite paint that provides a uniform surface potential (Robertson et al., 2004). The antennas are made from stainless steel rods. The dust beam is pointed at a 25×25 mm^2 tungsten (W) foil that is mounted near the edge of the HGA. The antennas and the W target are cleaned using organic solvents. The model is mounted in the middle of a large experimental vacuum chamber using electrically isolating brackets. Note that the antennas are relatively far from the location of dust impacts, and thus the expanding impact plasma. In this arrangement, the dominant signal generation mechanism comes from the charging of the spacecraft body.

A new model SC has been developed based on the experience from the previous laboratory studies (Nouzák et al., 2018, 2020, Shen et al., 2021a). In Figure 5.5 (b), the new model SC is a hollow sphere with a radius of $R_{SC} = 7.62$ cm, and is equipped with four antennas arranged into one plane and spaced 90° apart. Each antenna is a 27 cm long rod with a 1.6 mm diameter. The materials of both the SC and the antennas are stainless steel. The spherical SC is coated with graphite paint in order to provide it with a uniform surface potential (Robertson et al., 2004). The surfaces of the antennas were cleaned using organic solvents and are not coated. The circumference of the model SC is wrapped with a tungsten (W) foil in the plane of the antennas. The foil is approximately 1.5 cm wide and is attached to the sphere by spot-welding. The purpose of the W foil is to provide a target surface for the dust impacts, and thus making the measurements directly comparable to prior studies using the same material (Nouzák et al., 2018, 2020, Shen et al., 2021a).

The surface of the foil was also cleaned using organic solvents. The model SC is mounted onto the bottom end of a vertical shaft such that the antennas are in the horizontal plane. The shaft is connected to a rotary feedthrough that positions the model SC into the center of the large vacuum chamber. In this arrangement, we aim to characterize the signal variation associated with the impact locations (Shen et al., 2021b).

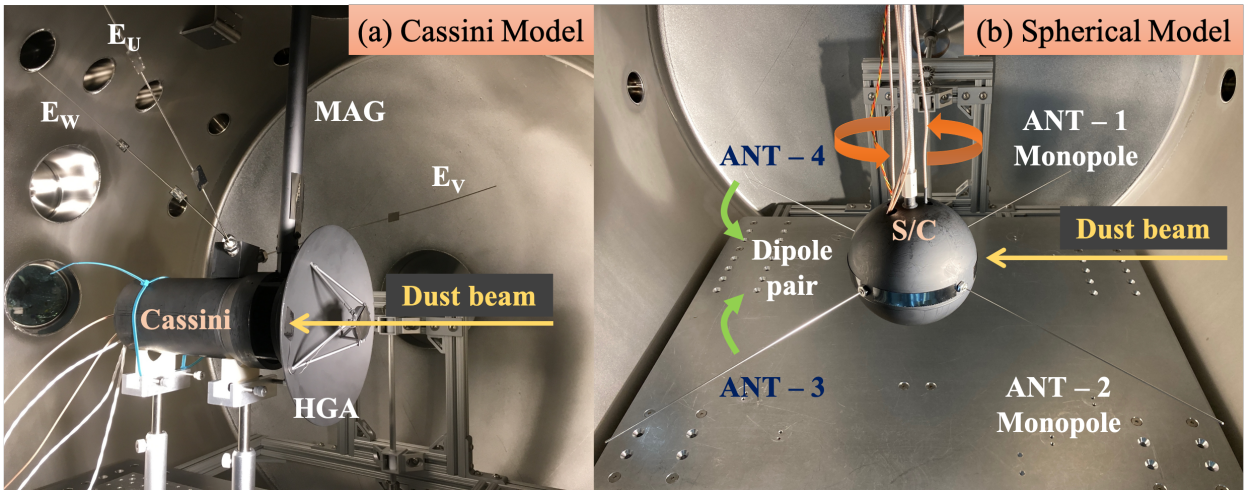

Figure 5.5: Two model spacecrafts shown when mounted inside the vacuum chamber. The dust beam is pointed at the W-foil attached (a) near the edge of HGA on the Cassini model and (b) the circumference of antenna plane of the spherical model, as the arrows indicated. See text for more detail.

The purpose of transiting from the Cassini model (*left*) to the spherical SC model (*right*) is to constrain the complexity of spacecraft geometry for characterizing the impact waveforms that respond to specific impact locations. When applying the Cassini SC model, the antenna E_W is considered not to interfere with the expanding plasma cloud generated upon the impact on HGA. Thus, the monopole measurements ($V_{meas} = \delta V_{E_W} - \delta V_{SC}$) allows characterizing the signal variation mainly due to the spacecraft charging. Next, a spherical model with a known spacecraft radius reduces the variables and is applicable to investigate the variation of signal waveforms due to the impact location (as the simulation shown in Figure 5.9 and data analysis provided in Section 6.2).

5.2.2 Measurement Conditions

Iron (Fe) dust particles are used in two sets of SC model experiments. The dust-target (Fe-W) combination is selected such that the results are directly comparable to prior studies (Collette et al., 2015, 2016, Nouzák et al., 2018, 2020). An additional aluminum (Al) dust campaign with the same W-target has been performed to identify the potential signal variations due to dust composition. The collected impact events are in the speed range of $20-40$ km/s. The typical mass and radius of these spherical impactors are about 10^{-18} kg and $40-50$ nm, respectively. In addition, a specific low-speed impact campaign ($\sim$ 5 km/s) has been performed, and the corresponding mass is on the order of 10^{-16} kg. In the experiments, the dust beam is pointed near the edge of HGA of the Cassini model and at the circumference of the spherical SC model, thus making the impacts occur in the normal direction to the W-target foil (i.e., arrows indicated in Figure 5.5).

5.3 Instrument Characteristics

5.3.1 Electronics

The front-end electronics are integrated into the cylindrical part of the Cassini SC model and the hollow body of the Spherical SC model (see Figure 5.5). As for the Cassini SC model, the measurement configurations were set for $E_U - E_V$ antennas in a dipole mode and $E_W - SC$ in a monopole mode. In comparison, the spherical SC model configures two antennas as monopoles ($V_{ANT-1} - V_{SC}$ and $V_{ANT-2} - V_{SC}$), and one pair operates in the dipole mode ($V_{ANT-3} - V_{ANT-4}$).

The previous measurements reported by Nouzák et al. (2018) indicated that some of the fine structures in the antenna signals were not fully resolved due to the limited bandwidth of the previous setup (50 Hz $-$ 400 kHz). The bandwidth of the electronics has been extended to 270 Hz $-$ 5 MHz, which resolves this issue. Figure 5.6 depicts the circuit diagram of front-end electronics. The instrumentation amplifier (INST Amp) measures the voltage difference between elements, followed by an operational amplifier (OP Amp) and a buffer amplifier. The total voltage gain of the electronics is $G = 50$. The upper limit of the bandwidth corresponds to a rise time

of about 70 ns, and the slew rate of the amplifiers is 35 V/μs, which does not introduce further limitations.

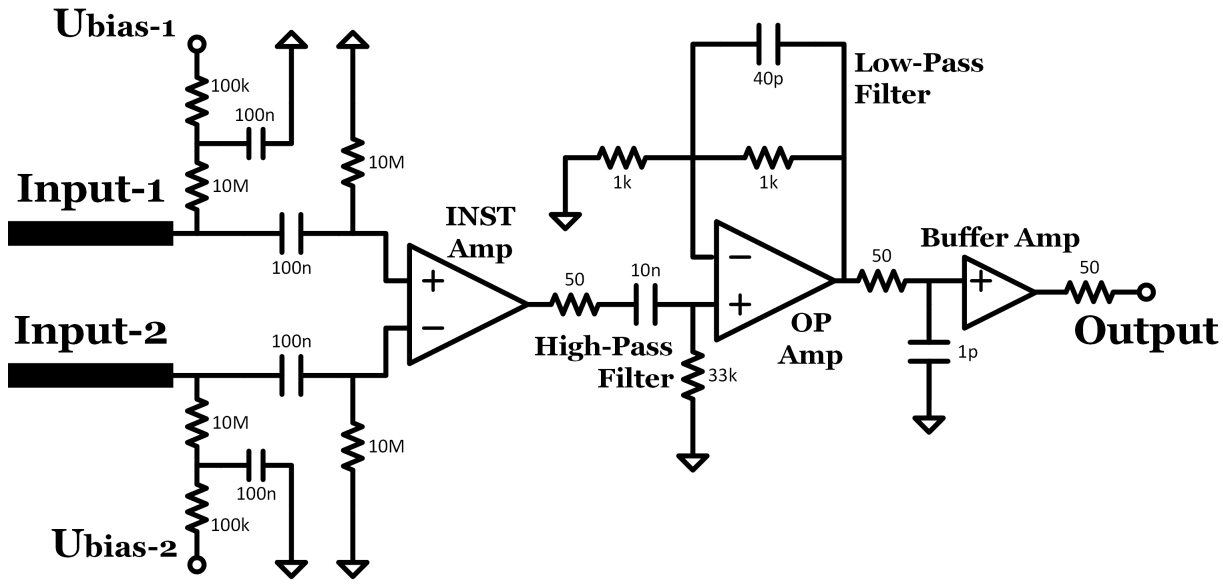

Figure 5.6: The schematic diagram of the front-end electronics used for the laboratory measurements. See text for more detail.

The circuits also allow the external biasing of the SC and antennas. The same bias voltage (U_{bias}) is applied to each of the SC and antenna elements through individual biasing resistors. Here we take the spherical SC as an example. The measurement configurations include two monopoles and a dipole pair. Hence, the effective values of these resistors are $R_{BIAS,A} \cong 5M\Omega$ resistors for each of the antennas, and $R_{BIAS,SC} \cong 2.5M\Omega$ for the SC. The bias resistor values are combined with the effective capacitances of the antennas and the SC, which provide the characteristic time constants for the elements; for example, $R_{BIAS,A}\, C_{ANT,eff}$ for each of the antennas and $R_{BIAS,SC}\, C_{SC,eff}$ for the model SC. The concepts of effective capacitances ($C_{ANT,eff}$ and $C_{SC,eff}$) have been described in Section 4.5. Finally, the measured waveforms are recorded using a fast-digitizing oscilloscope at a sampling rate of 200 MS/s.

5.3.2 Impulse response

The impulse response describes the characteristics of front-end electronics and can be simulated through a commercial SPICE (Simulation Program with Integrated Circuit Emphasis) software. Convolving the calculated voltages obtained from the matrix form (i.e., Equation 4.21) with the impulse response allows to properly restore the measured waveforms. Figure 5.7 shows the impulse response of front-end electronics followed by a decay time constant of approximately 330 μs.

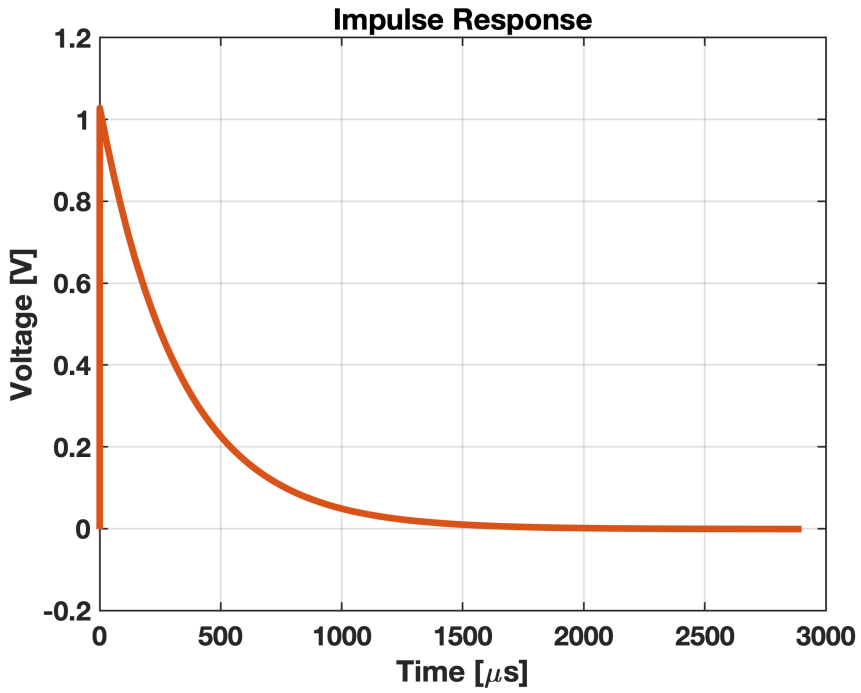

Figure 5.7: The impulse response of the electronics performed in laboratory measurements. It represents the circuit characteristics corresponding to the diagram displayed in Figure 5.6.

5.4 Capacitance Matrix

5.4.1 Constructing the Capacitance Matrix for Laboratory Spacecraft Model

The elastance matrix is a key element in implementing the electrostatic antenna signal generation model presented in Section 4.6. This section describes how to calculate this matrix for the model SC described above, how to calculate it for an actual SC, and the physical meaning of the elements. Section 4.6 provides the details for a SC with a single antenna.

The elastance matrix $[\boldsymbol{a}]$ is the inverse of the capacitance matrix, $[\boldsymbol{b}] = [\boldsymbol{a}]^{-1}$. The dimension of the matrices is $(n+1) \times (n+1)$, where n is the number of independent antennas in the system, and the $+1$ refers to the SC body. A diagonal element b_{ii} in $[\boldsymbol{b}]$ is called the self-capacitance and represents the capacitance of the i-th object in a configuration, where all other elements of the system are grounded (Jackson, 1999). For example, assuming that $i = 0$ refers to the SC, it follows that $b_{00} = C_{SC} + 4\,C_X$. Here C_{SC} is the physical capacitance of the SC body only (without the antennas), and an assumption has been made that the mutual capacitances between the SC and each of the antennas are equal. The non-diagonal elements b_{ij} represent the negative value of the mutual capacitances between elements i and j. For example, $b_{01} = -C_x$, which is the mutual capacitance between the SC and antenna #1. The matrix is symmetric, i.e., $b_{ij} = b_{ji}$ The capacitance matrix for the model SC used in the laboratory measurements can be written as:

$$
\begin{aligned}
[\boldsymbol{b}] &\cong \begin{bmatrix}
C_{SC}+4C_x & -C_x & -C_x & -C_x & -C_x \\
-C_x & C_{ANT,1}+C_x & 0 & 0 & 0 \\
-C_x & 0 & C_{ANT,2}+C_x & 0 & 0 \\
-C_x & 0 & 0 & C_{ANT,3}+C_x & 0 \\
-C_x & 0 & 0 & 0 & C_{ANT,4}+C_x
\end{bmatrix} \\
&\cong \begin{bmatrix}
52 & -6.5 & -6.5 & -6.5 & -6.5 \\
-6.5 & 16 & 0 & 0 & 0 \\
-6.5 & 0 & 17 & 0 & 0 \\
-6.5 & 0 & 0 & 19 & 0 \\
-6.5 & 0 & 0 & 0 & 16.5
\end{bmatrix} pF.
\end{aligned}
\tag{5.5}
$$

The last term in Equation 5.5 presents the values determined from measurements made on the model SC. It makes the simplifying assumption that the antenna-to-antenna mutual capacitances are negligible, and the validity of this assumption is provided below. The measurements were performed with the model SC installed into the vacuum chamber, that is, in the same conditions as the dust impact measurements. The measurements were conducted using a function generator and a $C_{test} = 10$ pF test capacitor. The function generator was configured to output a square wave with a $\Delta V = 50$ mV amplitude, and this signal was applied onto the SC or antenna elements through the test capacitor. The magnitude of the injected test charge was thus $Q_{test} = \Delta V\, C_{test} = 0.5$ pC. The response of the model SC's electronics to the test charge input was recorded using a fast-digitizing scope. The output signals then were fitted utilizing an industry standard SPICE (Simulation Program with Integrated Circuit Emphasis) software tool to calculate the net capacitance sensed on the input. Figure 5.8 illustrates one instance of the waveform generator output and the recorded signal in response to the injected test charge.

The first set of measurements were performed following the definition of the diagonal elements of the Maxwell capacitance matrix. In these measurements, all but one element of the system was grounded in order the calculate the net capacitance. The list below provides the results of these measurements:

$$\begin{aligned} SC: &\quad C_{test} + C_{SC} + 4C_x \cong 62.0pF \\ Antenna\#1: &\quad C_{test} + C_{ANT,1} + C_x \cong 26.0pF \\ Antenna\#2: &\quad C_{test} + C_{ANT,2} + C_x \cong 27.0pF \\ Antenna\#3: &\quad C_{test} + C_{ANT,3} + C_x \cong 29.0pF \\ Antenna\#4: &\quad C_{test} + C_{ANT,4} + C_x \cong 26.5pF. \end{aligned} \tag{5.6}$$

This set of equations already include the simplifying assumption that the mutual capacitances between the SC and the antennas are the same. Since there are six unknowns and only five equations, further measurements were necessary. Additional measurements were made, where the test charge was injected into one of the antennas while keeping the remaining three antennas

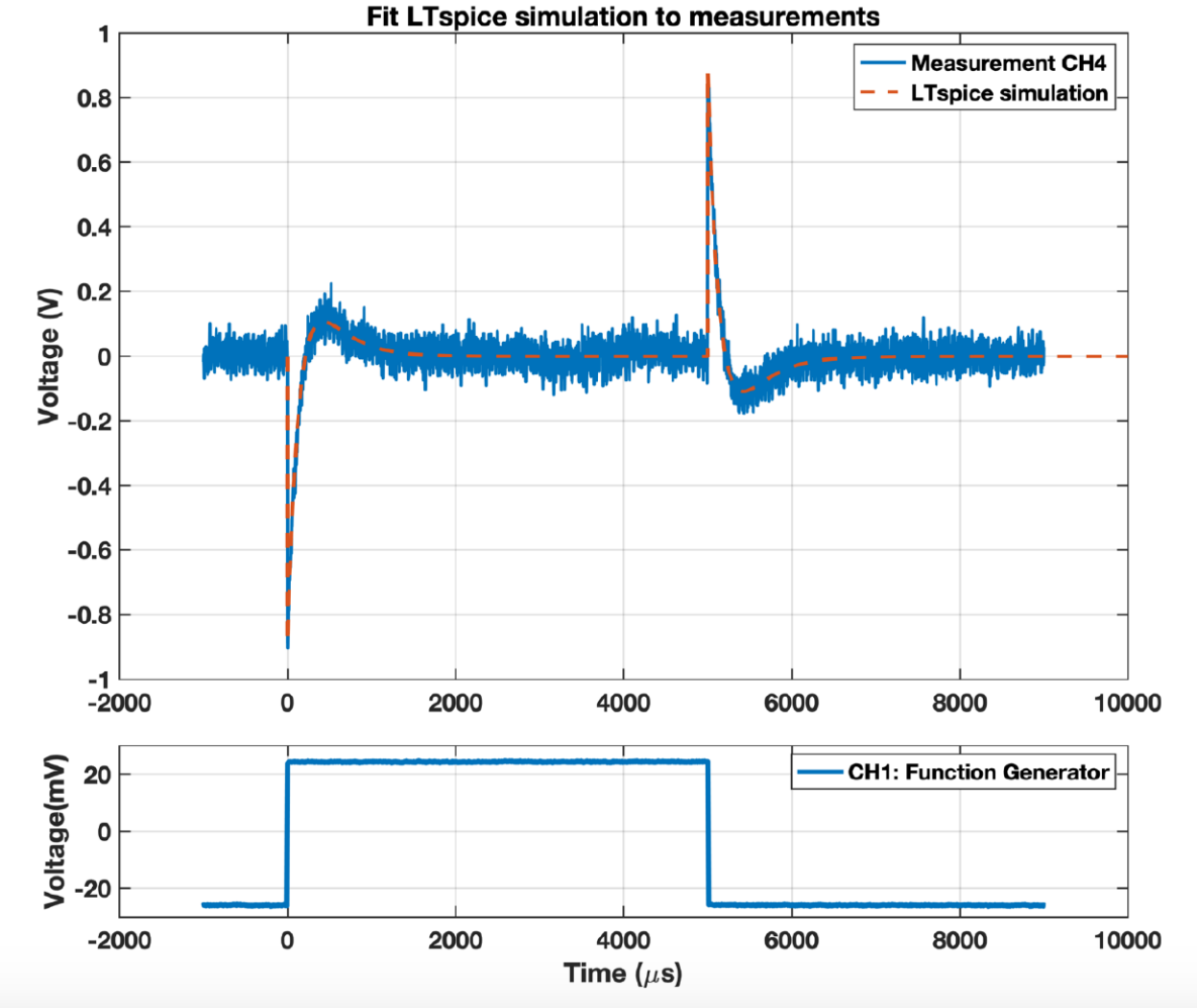

Figure 5.8: The example waveforms of the Function Generator output (bottom panel) and the recorded signal output from the model SC after injecting the test charge onto one of the antennas. See text for detail.

grounded but allowing the SC to float. The output signals of these measurements were recorded as well. And as a final step, in a numerical procedure, the value of C_x was varied between $4 - 8$ pF with steps of 0.5 pF in order to find the solution that provided the best fit for all measurements. This exercise resulted in $C_x = 6.5$ pF as the best value, which then provides the following physical capacitances of the elements of the system: $C_{SC} = 26$ pF, $C_{ANT,1} = 9.5$ pF, $C_{ANT,2} = 10.5$ pF, $C_{ANT,3} = 12.5$ pF, and $C_{ANT,4} = 10$ pF. These values are significantly higher than the capacitances of the elements based on their physical dimensions alone. There are several reasons for this. The model spacecraft is installed into a vacuum chamber with grounded walls. Further, the electronic boards mounted within the hollow spherical model SC are referenced to ground, which increases the capacitances of the SC, but also those of the antennas. In other words, for the case of the laboratory model SC, the parasitic capacitances C_{WP} from the cabling and preamplifier (see Section 4.5) contribute to the antennas' capacitances with respect to ground, rather than to the mutual capacitance towards the SC.

The capacitance matrix can also be calculated using standard numerical electrostatic solvers (e.g., commercial software like COMSOL Multiphysics, CST Studio Suite, or COULOMB). The simulated matrix for the model SC is the following:

$$[\boldsymbol{b}]^{sim} = \begin{bmatrix} +11.800 & -1.2100 & -1.2100 & -1.2100 & -1.2100 \\ -1.2100 & +3.1300 & -0.0728 & -0.0267 & -0.0728 \\ -1.2100 & -0.0728 & +3.1300 & -0.0728 & -0.0267 \\ -1.2100 & -0.0267 & -0.0728 & +3.1300 & -0.0728 \\ -1.2100 & -0.0728 & -0.0267 & -0.0728 & +3.1300 \end{bmatrix} pF. \tag{5.7}$$

The elements of $[\boldsymbol{b}]^{sim}$ are considerably different from those of $[\boldsymbol{b}]$ from Equation 5.5. This is because the simulation result can only include the geometry of the system. For example, the simulated physical capacitance of the first antenna is only $C_{ANT,1} = \sum_{j=0}^{4} b_{1,j} \cong 1.75$ pF, which is significantly lower than the ~ 10 pF capacitance as determined from the actual measurements. The difference is due to the contribution from cabling, electronics, etc. Similarly, the geometric contribution to the mutual capacitance between the SC and the antenna is only $C_G = 1.21$ pF.

The results in Equation 5.7 also demonstrate that the mutual capacitance between two adjacent antennas (~ 0.073 pF) is much smaller than that of the SC-to-antenna mutual capacitance and thus can be neglected for the model SC system, where the antennas are placed far from one another. On the other hand, the antennas on the Cassini or STEREO missions are mounted on the same base and thus their mutual capacitance will likely be significant (Gurnett et al., 2004, Bale et al., 2008).

5.4.2 Constructing the Capacitance Matrix for Space Applications

This thesis aims to provide the framework for the improved analysis of the dust impact signals measured by antenna instruments on space missions. This section provides the recommendation on how to estimate the capacitance matrix for any spacecraft with adequate accuracy. The first step is importing a reasonably detailed Computer-Aided Design (CAD) model of the SC with the antennas into the software tool and calculate the simulated capacitance matrix. This matrix can be deconstructed following the definitions provided in Equation 5.5 in order to determine the values of C_{SC}, the capacitances for each of the antennas, and the mutual capacitances between the elements. Alternatively, the antenna capacitances published by the instrument team may also be used. The mutual capacitances between the antennas may or may not be negligible, depending on their dimensions and arrangement. At this point, the mutual capacitance values include only the contributions from the geometry of the system (C_G). The contribution from the base capacitance (C_B) and the combined effect of cables and preamp input capacitance (C_{WP}) are typically provided by the instrument team. The combined value is called the stray capacitance, $C_{stray} = C_B + C_{WP}$ (e.g., Bale et al. (2008)). The mutual capacitance between the antennas and the SC is then given as $C_x = C_G + C_{stray}$. The stray capacitance may already include the effect of C_G, and in this case, it is simple $C_x = C_{stray}$. The capacitance matrix defined by Equation 5.5 can form here be reconstructed from the determined values.

5.5 Simulation of Induced Charging for the Model Spacecraft

Numerical solvers can provide the induced potential from a test point charge as described in Section 4.6. This section presents the calculated induced potentials for the three geometries investigated in the laboratory experiments, namely with the dust impact occurring in between antennas #1 and #2 at 10°, 30°, and 45° measured from antenna #1. Figure 5.9 shows the induced potentials on the elements for these three configurations. The point test charge has the value of $Q_{test} = 100$ pC and is moving on a radial trajectory, starting 0.3 mm from the surface of the SC. This setup is similar to that shown in Figure 4.8 for a simplified case, and the relevant capacitance matrix is $[\boldsymbol{b}]^{sim}$ from Equation 5.7. The corresponding simulated elastance matrix is $\left[\boldsymbol{a}^{sim}\right] = \left[\boldsymbol{b}^{sim}\right]^{-1}$.

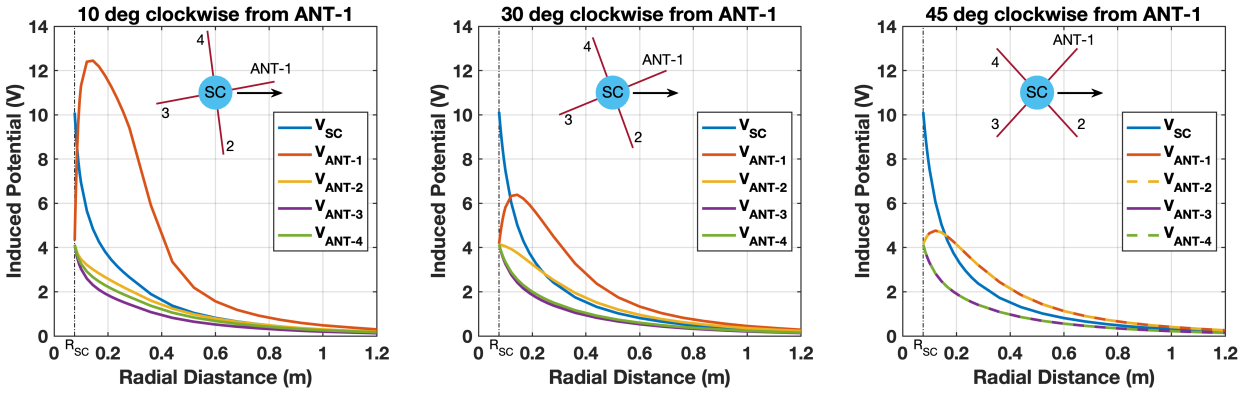

Figure 5.9: Induced potentials on the SC and the four antennas from a test charge moving on a radial trajectory for three different configurations relative to antenna #1 (10°, 30°, and 45°). The potentials are calculated numerically for a $Q_{test} = 100$ pF test charge and the geometry of the model SC used in the experiments. See text for more detail.

When the test charge is closest to the SC body, the induced charge on the antennas is negligible, and the SC potential is $\delta V_{SC} = a_{0,0}^{sim} Q_{test} = 10.18$ V, following Equation 4.10. The meaning of the first element of the elastance matrix is the inverse of the effective capacitance of the SC. For the same conditions, the potentials on all of the antennas are the same. For example, on antenna #1 the potential is $\delta V_{ANT,1} = a_{1,0}^{sim} Q_{test} = 4.17$ V, and this relation defined the physical

meaning of the corresponding element of $\left[\boldsymbol{a}^{sim}\right]$. The mutual capacitive coupling from the SC to the antenna is significant and will affect the measured voltage ($\delta V_{meas} = \delta V_{ANT,1} - \delta V_{SC}$).

The SC potential for all three cases decreases monotonically as the test charge is moving radially outward. For the 10° case, the induced potential on antenna #1 is increasing sharply due to the test charging getting in the close vicinity of this element. At its maximum of about $\delta V_{ANT,1} = 12.5$ V, the induced charge on this antenna is about 37% of Q_{test}, as it can be calculated from the $0.37\, a_{1,1}^{sim}\, Q_{test} \cong 12.5$ V relation. Antenna #1 has a pronounced, albeit lower maximum potential value for the 30° case as well. The values of the relevant coefficients from the elastance matrix are: $a_{0,0}^{sim} = 1.018 \times 10^{11} F^{-1}$, $a_{1,0}^{sim} = 0.4166 \times 10^{11} F^{-1}$, and $a_{1,1}^{sim} = 3.369 \times 10^{11} F^{-1}$.

The potential profiles on the antennas on the far side of the SC (#3 and #4) mostly follow that of the mutual coupling from the SC, with only a small contribution from direct induced charging from the point charge. The dipole signal between these antennas ($\delta V_{dipole} = \delta V_{ANT,3} - \delta V_{ANT,4}$) is small, albeit zero only for the symmetric 45° case. Were antennas #1 and #2 connected as a dipole, the measured signal ($\delta V_{ANT,1} - \delta V_{ANT,2}$) would be significant and a strong function of the impact location and the expansion of the plasma plumes with respect to the antenna geometry.

Chapter 6

Data Analyses and Interpretations

The physical model presented in Chapter 4 is used to fit the recorded waveforms, thus providing relevant parameters of the impact plasma. These include the geometric coefficient (κ), the electron and ion expansion speeds (v_e and v_i), their corresponding effective temperatures (T_e and T_i), the impact charge (Q_{IMP}), and the free fitting parameters of induced charging associated with impact locations (ζ_e and ζ_i). A comprehensive measurement campaign has been conducted to investigate the impact signal variations due to bias voltage (V_{SC}), impact location, antenna operation mode, impact speed (v_d), and dust composition. Hundreds of dust impact waveforms were recorded using both the Cassini and Spherical spacecraft models. These are roughly equally distributed under certain control variables for data analyses. The primary goals for laboratory measurements include: (1) Evaluate the validity of the proposed signal generation model and preserve the basic parameters of the impact plasma comparable over the whole set of measurements (Section 6.1 and 6.3). (2) Characterize dust detection in monopole configuration with respect to impact locations (Section 6.2). (3) Characterize dust detection in dipole configuration with respect to impact location (Section 6.4). (4) Characterize the signal variations that correspond to impact speed and dust composition (Section 6.5 and 6.6). In Section 6.7, we will further discuss the challenges and solutions of applying the proposed model to collected datasets in several space missions.

6.1 Signal Variations of Spacecraft Potential

6.1.1 Bias Potential $V_{SC} = 0\,V$

Figure 6.1 shows the waveforms of three typical impact events for the SC bias voltage set to $V_{SC} = 0\,V$. This condition allows examining the free expansion of the impact plasma from the impact location. The general shape of the signals is similar to those described in Section 4.4.2. The waveform starts with the negative-going preshoot due to the fast-escaping electrons. The expansion of electrons and ions from the impact plasma is over at around $t = 50\ \mu$s. The subsequent exponential decay is the discharge of the net collected charge on the SC with a characteristic time constant of $\tau_{dis,L} = R_{BIAS}\,C_{SC,eff}$. The first step in the data analysis is calculating the effective SC capacitance from this exponential decay, yielding the value of $C_{SC,eff} = (48 \pm 8)$ pF. This capacitance value can be used to convert the measured voltage signals into charge. It is noted that the calculated value of C_{SC} is lower than that found by Nouzák et al. (2018) by about a factor of 2.5 for a similar setup. The effective value of C_{SC} is the sum from the physical capacitance of the SC body, and contributions from the parasitic capacitances to the mount, the antennas, the vacuum chamber, electronics boards, etc. The discrepancy between the values may be due to updated electronics boards, the slightly modified mounting brackets, or the routing of the cables, for example. The physical capacitance of the SC can also be estimated as $C = \epsilon_0\sqrt{4\pi S} \cong 18.6$ pF, where $S \cong 0.35$ m^2 is the surface area of the convex envelope around the model (Chow and Yovanovich, 1982).

The next step in data analysis is finding the electron and ion expansion speeds. Following Equation 4.5, the induced charge varies with time as $\sim 1\,/\,(1 + \dfrac{v_x t}{R_{SC}})$, where x refers to electrons or ions. The SC model, however, is not spherical, therefore, the "effective" value of the SC radius is estimated to be $R_{SC} = 8$ cm (Figure 5.5 (a)). For this dimension, the ion expansion speed varies between $5 - 15$ km/s, with an average value of $v_i = (9.3 \pm 3.0)$ km/s. This ion expansion speed agrees well with values reported by Collette et al. (2016), Kellogg et al. (2016), and Lee et al. (2012). The expansion of the much faster electrons generates the steep slope of the preshoot signal

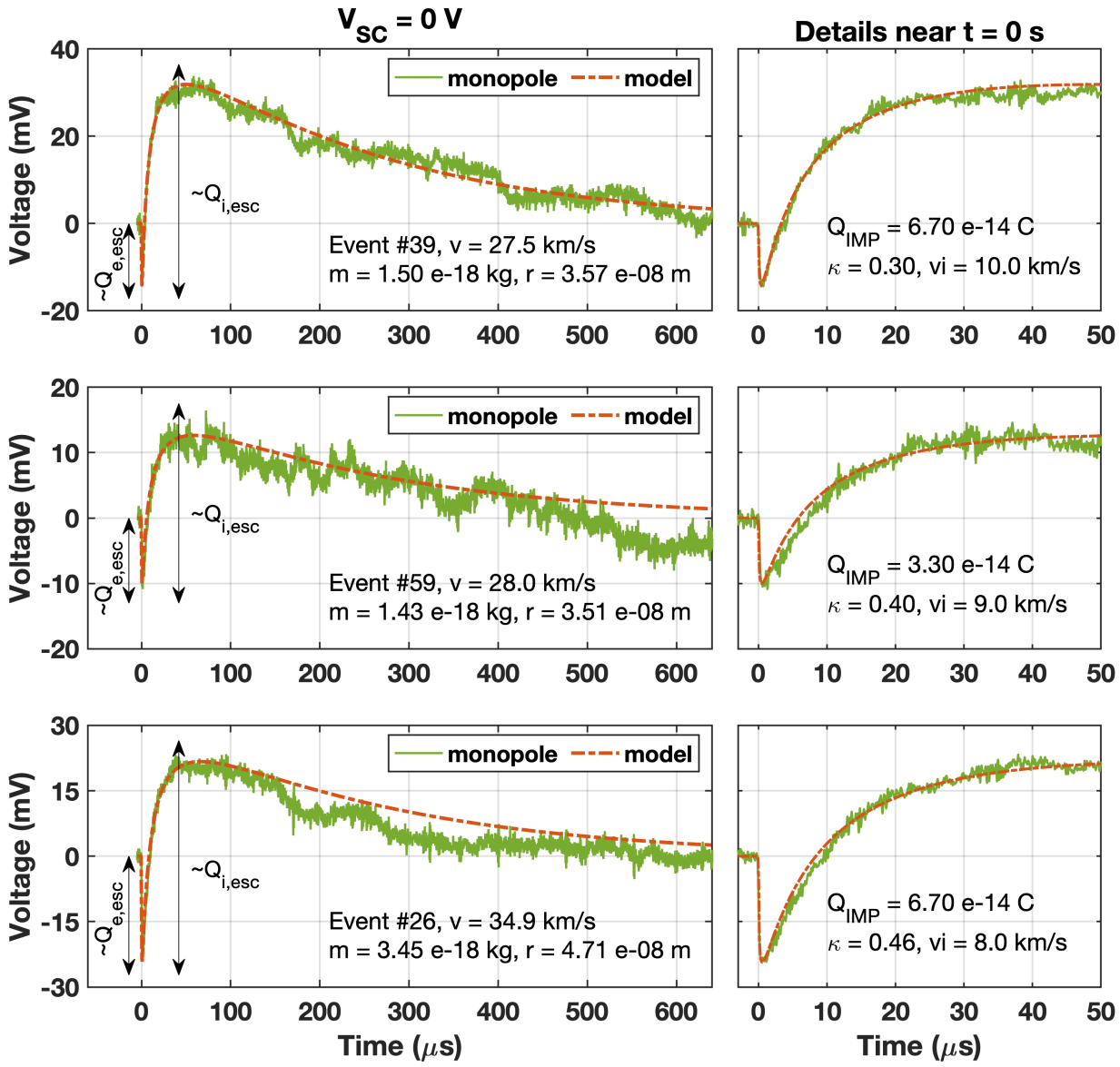

Figure 6.1: Three example waveforms measured by the monopole antenna for $V_{SC} = 0\,V$. The red dashed curves are from the model fitted to the data. The parameters of the particles are provided along with some of the parameters obtained from the fitting routine. The radius of the particle is provided as r. The approximate values of the escaping electron and ion charges are indicated. See text for more detail.

with a measured rise-time of about 0.4 μs that can be fully resolved by the updated fast electronics (Section 5.3). Nevertheless, finding a consistent value for v_e turned out to be difficult, possibly due to the simultaneous expansion of both the electrons and ions, a wide energy distribution of the electrons, or large impact−to−impact variations. The electron escape speed is set to $v_e \cong 10^6$ m/s, as this value provides good fits to the data. This speed corresponds to the thermal speed of electrons with about 2 eV temperature. Calculations using the model suggest that by changing v_e by a factor of 2, the change of the preshoot amplitude is limited to $< 15\%$. The uncertainty associated with the selection of the value for v_e is thus relatively small.

Figure 6.1 clearly indicates that the ratios of the escaping electron and ion charges are roughly equal to $Q_{e,esc} \,/\, Q_{i,esc} \approx 1 \,/\, 2$. Under the assumption that the number of electrons and ions generated by the impact is the same, this observation means that electrons are less likely to escape from the surface, even at zero bias potential. This observation is consistent with the physical picture of a stream of ions moving away from the impact location, while the faster electrons acquire an isotropic distribution. Once the expanding plasma cloud grows sufficiently large for the electrons and ions decouple from one another (typically within 1 mm from the surface in the lab measurements), half of the electrons are moving back toward the target, and half of the electrons away from the target. This physical picture is described in the model by the geometric coefficient κ in Equations 4.2 and 4.3. Fitting the data for $V_{SC} = 0\,V$ bias voltage allows determining κ independent of the electron temperature. The data analysis yielded a range of about $\kappa = 0.3 - 0.5$, with an average value of $\kappa = 0.405 \pm 0.078$. The fact that somewhat less than half of the electrons escape may be explained by the concave shape of the HGA, where the dust impacts occur (see Figure 5.5).

6.1.2 Bias Potential $V_{SC} = +5\,V$

The waveforms recorded for a spacecraft bias potential $V_{SC} = +5\,V$ (Figure 6.2) are generally similar to the zero-bias case. A notable difference is the reduced amplitude of the preshoot, as only a fraction of electrons is capable of overcoming the potential barrier from the applied positive bias

voltage. The effective temperature of the electrons is then determined from the fitting of the data while keeping the $\kappa = 0.405$ parameter constant. The meaning of the effective temperature T_e is defined by Equation 4.2; noting that the expansion away from the surface of the SC is a 3D process, while the model is simplified to a spherically symmetric 1D case. The fitting of the data set yielded $T_e = (7.8 \pm 1.3)$ eV. This value is significantly higher than the ~ 1 eV value reported by Collette et al. (2016) and Nouzák et al. (2020) for the same impact speed range and dust-target material combination. The authors in the former source calculated T_e from the statistical distribution of the retained charge on an impact plate as a function of the applied bias voltage. Nouzák et al. (2020) collected waveforms using a similar setup as presented in this thesis, and then statistically evaluated the reduction of the fraction of escaping electrons for 0 and +5 V bias potentials. In comparison, each waveform in this article has been fitted to the model from Section 4.3 in order to obtain a value for T_e. The measurements presented in this thesis are collected using electronics with an improved bandwidth that allowed fully resolving the preshoot part of the signals. This fact may at least partially describe the reason for the higher electron temperatures reported here. A recent study performed by Kočiščák et al. (2020) has measured the effective temperatures of the negative charge carriers in the impact plasma (assuming both free electrons and anions are present) for an olivine dust sample and tungsten target. The particles were coated with a conductive polymer in this study that enabled their acceleration. The temperature reported for an impact velocity range of $12 - 18$ km/s was 4.4 eV, which is closer to the value reported here.

The routine used for fitting the model to the measured waveforms treats the electron expansion speed (v_e) and electron temperature (T_e) as independent variables, while in reality they are naturally related. The selected expansion speed of $v_e = 10^6$ m/s corresponds to about 2 eV electron temperature, which is significantly lower than the 7.8 eV effective temperature determined above. This is not necessarily a contradiction, however, as in the assumed isotropic expansion of the electrons, the radial component of the velocity varies over a wide range depending on the elevation angle of the electrons with respect to the surface normal at the location of the impact. The v_e parameter thus describes the effective radial expansion speed of the electrons over their entire

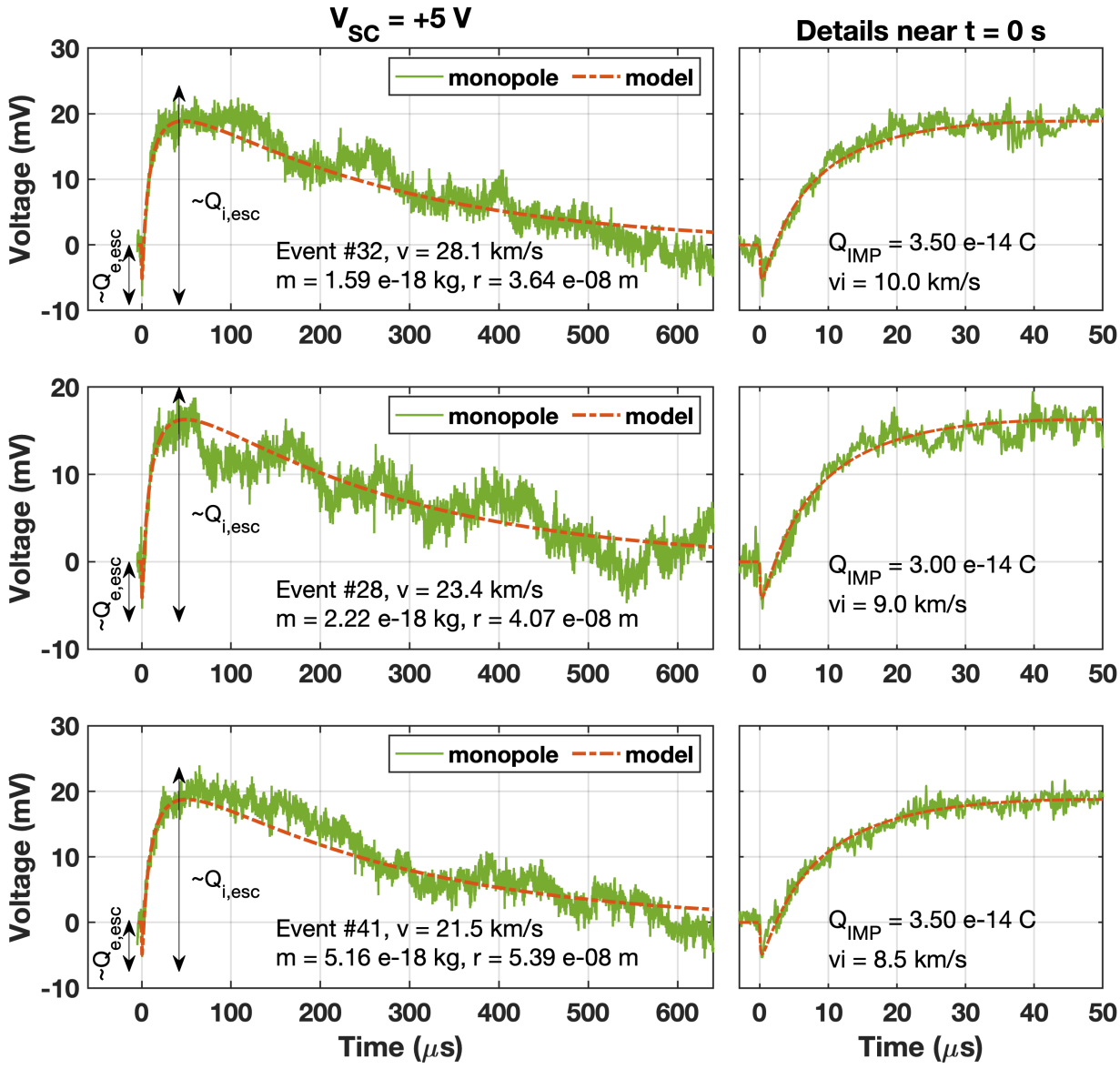

Figure 6.2: Three example waveforms measured by the monopole antenna for $V_{SC} = 5\,V$. The labeling is the same as in Figure 6.1.

distribution. As discussed in Section 4.4, the amplitude of the preshoot is also affected by the ratio of the electron and ion expansion speeds.

The ion expansion speed determined for the $V_{SC} = +5\,V$ case is $v_i = (9.3 \pm 2.3)$ km/s, that is, essentially the same as the zero-bias case. This makes sense, as the applied bias is small in comparison to the kinetic energy of the cations. Besides, the potential profile scales with a distance d from the surface of the SC as $\sim 1\,/\,(R_{SC} + d)$, and the ion speed is only weakly affected in the early phases of the expansion.

6.1.3 Bias Potential $V_{SC} = -5\,V$

Figure 6.3 shows waveforms for negative bias potential $V_{SC} = -5\,V$, where the preshoot component is again pronounced. Following the argument from the bottom of the previous section, the negative bias has little effect on the collected versus escaping electron fraction, and thus $\kappa = 0.405$ is assumed. The effective temperature of the ions can be calculated similarly to those of the electrons using Equation 4.3. The result is $T_i = (25.4 \pm 12.5)$ eV, noting that the confidence in this number is lower, given that the ion temperature is high compared to the applied bias potential. Nevertheless, it is pointed out that the effective ion temperature for this impact speed range is in good agreement with 23 eV value measured by Collette et al. (2016), while the value determined by Nouzák et al. (2020) was $10-15$ eV. The cation temperature measured for an impact speed range of $12-18$ km/s and polymer-coated olivine particles was approximately 7 eV (Kočiščák et al., 2020). The ion expansion speed is $v_i = (10.0 \pm 3.1)$ km/s that is similar to the two cases from above. Since the ion temperature is significantly larger than the bias potential, the ion expansion speed is not significantly affected. It is interesting to note that the expansion speed and ion temperature values are consistent with one another for an ion mass of Fe ($m = 55.8$ u). Iron ions are no doubt one of the most abundant cation species in the impact plasma at these impact velocities. There is one noticeable deviation in the waveforms collected for negative SC bias, when compared to the other two cases. The preshoot peak is wider at the bottom and there is a ledge and a change in the slope (Figure 6.3). This feature is likely due to an artifact by the commercial front-end amplifier.

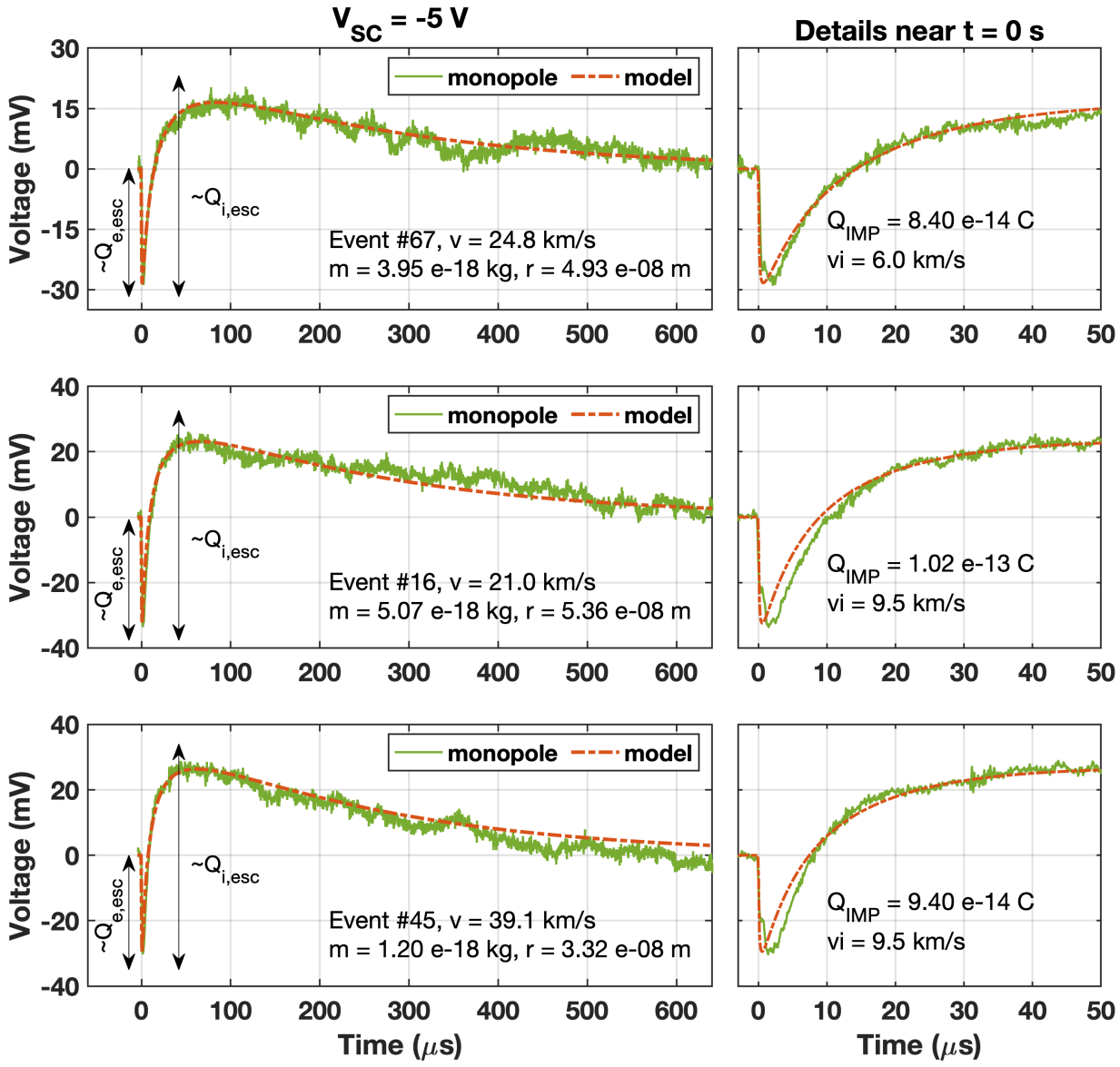

Figure 6.3: Three example waveforms measured by the monopole antenna for $V_{SC} = -5\,V$. The labeling is the same as in Figure 6.1.

6.2 Signal Variations of Impact Location

This section presents the analysis of the collected data with a goal to demonstrate the validity of the proposed electrostatic model. The main reason for this limitation is the incomplete understanding of the properties of the expanding impact plasma cloud. The model assumes that the expanding electrons have an isotropic velocity distribution; however, it is not obvious what the shape of the expanding plume of ions is. Section 5.5 above demonstrates that the voltages induced on the antennas are rather sensitive to how close the escaping charges get to the antennas. In other words, an ion plume in a shape of a narrow pencil beam would generate different induced voltages than an ion plume with a wider, conical shape, for example. In order to avoid the confusion between competing mechanisms and geometrical effects, a subset of the measurements was collected with antenna #2 connected to ground potential ($V_{ANT,2} = 0$). This means that the corresponding channel measures directly the inverted potential of the SC, i.e., $\delta V_{meas} = 0 - \delta V_{SC}$. Accounting for the duration and shape of the ion plume goes beyond the current capabilities of the signal fitting routine described below. Instead, we follow the simplification of spherical approximation presented in Section 4.3, and the escaping electrons and cations are modeled as point charges moving radially away with their respective escape velocities.

6.2.1 Fitting Routine

The numerical and simplified version of Equation 4.21 is used to fit the laboratory measurements to validate the electrostatic model and calculate some of the fundamental parameters of the escaping plasma plume. Since antenna #2 is grounded, there are only four active elements in the experimental system. The capacitance matrix with (4×4) elements is constructed following the description provided in Section 5.4, i.e.,

$$[\boldsymbol{b}^{exp}] \cong \begin{bmatrix} 52 & -6.5 & -6.5 & -6.5 \\ -6.5 & 16 & 0 & 0 \\ -6.5 & 0 & 19 & 0 \\ -6.5 & 0 & 0 & 16.5 \end{bmatrix} pF, \tag{6.1}$$

and the elastance matrix is calculated as $[\boldsymbol{a}^{exp}] = [\boldsymbol{b}^{exp}]^{-1}$. The geometric functions were calculated for radial trajectories for impact locations 10°, 30°, and 45° offset from antenna #1 (see Figure 5.9). The form of Equation 4.21 for numerical calculations is:

$$\begin{bmatrix} \delta V_{SC}(i) \\ \delta V_{ANT,1}(i) \\ \delta V_{ANT,3}(i) \\ \delta V_{ANT,4}(i) \end{bmatrix} = [\boldsymbol{a}^{exp}] \begin{bmatrix} \delta Q_{SC,col} + [\delta Q_{esc,e}\, g_{SC}(\vec{r_e}(i)) + \delta Q_{esc,i}\, g_{SC}(\vec{r_i}(i))] - \sum_{k=0}^{i-1} \frac{\delta V_{SC}(k)}{R_{base,SC}} \Delta t \\ \delta Q_{ANT,1,col} + [\zeta_e\, \delta Q_{esc,e}\, g_{ANT,1}(\vec{r_e}(i)) + \zeta_i\, \delta Q_{esc,i}\, g_{ANT,1}(\vec{r_i}(i))] - \sum_{k=0}^{i-1} \frac{\delta V_{ANT,1}(k)}{R_{base,A}} \Delta t \\ \delta Q_{ANT,3,col} + [\delta Q_{esc,e}\, g_{ANT,3}(\vec{r_e}(i)) + \delta Q_{esc,i}\, g_{ANT,3}(\vec{r_i}(i))] - \sum_{k=0}^{i-1} \frac{\delta V_{ANT,3}(k)}{R_{base,A}} \Delta t \\ \delta Q_{ANT,4,col} + [\delta Q_{esc,e}\, g_{ANT,4}(\vec{r_e}(i)) + \delta Q_{esc,i}\, g_{ANT,4}(\vec{r_i}(i))] - \sum_{k=0}^{i-1} \frac{\delta V_{ANT,4}(k)}{R_{base,A}} \Delta t \end{bmatrix}. \tag{6.2}$$

The numerical calculations are performed over discrete time steps Δt, and index (i) represents time $t(i) = i \times \Delta t$, where $t = 0$ marks to the instance of the impact. The dust impact plasma at this point is approximately the size of the impacting particle with net zero charge, and thus the initial conditions are:

$$\begin{bmatrix} \delta V_{SC}(0) \\ \delta V_{ANT,1}(0) \\ \delta V_{ANT,3}(0) \\ \delta V_{ANT,4}(0) \end{bmatrix} = \begin{bmatrix} 0 \\ 0 \\ 0 \\ 0 \end{bmatrix} V. \tag{6.3}$$

The term on the right-hand side of Equation 6.2 represents the time evolution of the charge balance on each of the elements, including both the collected and induced charges. The first term in the vector is the collected charge given by Equations 4.2 or 4.3 and is a constant. The second term is the sum of the induced charges from the escaping electrons and ions. These charges are weighted by the geometric function, where position vectors of the assumed point charges evolve over time.

The position vectors are $\vec{r_e}(i) = \vec{r}_{imp} + \hat{r}\, v_e\, i\Delta t$ for the escaping electrons, and $\vec{r_i}(i) = \vec{r}_{imp} + \hat{r}\, v_i\, i\Delta t$ for the escaping ions. Here $\vec{r}_{imp}$ is the location of the impact, $\hat{r}$ is the radial unit vector at the location of the impact, and v_e and v_i are the electron and ion escape speeds, respectively. Two new parameters, ζ_e and ζ_i, are introduced for the induced charge term for antenna #1, which is the closest to the dust impact locations. These function as free fitting parameters that allow accounting for the deviations of the shape of expanding plasma plume from a point charge moving radially outward with a constant speed.

The last term is the integral (or summation in the numerical form) of the discharge current. This term is somewhat different from that presented in Equation 4.21 as each element in the model SC can only discharge through its individual bias resistor, which is referenced to ground. This discharge current will drive the voltage perturbations on each of the elements to zero for $t \to \infty$. Equation 6.2 can be easily modified to be applicable for SC operating in the space environment. This requires implementing the discharge current from the ambient plasma (Section 4.8) and modifying the last term following Equation 6.2.

Solving Equation 6.2 provides the time evolution of the physical voltages on each of the elements. This equation, however, does not include the effects of the electronics, namely its gain and limited bandwidth. The actual waveforms measured by the antenna instrument can be calculated by convolving the physical voltages by the impulse response of the electronics. Figure 5.7 shows the impulse response of the electronics used in the model SC that was calculated using industry standard SPICE (Simulation Program with Integrated Circuit Emphasis) software from the schematics of the electronics and the parts used.

6.2.2 Impacts at 45°

Figure 6.4 shows a typical set of antenna signals measured for an impact location in between antennas #1 and #2, that is, at 45° off from antenna #1 (Figure 5.5 (b)). The bias voltage on all elements is set to $0V$. The two measured signals shown are $\delta V_{mono,1} = \delta V_{ANT,1} - \delta V_{SC}$, and $\delta V_{mono,2} = -\delta V_{SC}$, since $\delta V_{ANT,2} = 0$. The first thing to notice is that the two signals are sig-

nificantly different, with the maximum on $\delta V_{mono,1}$ occurring earlier in time. This indicates that induced charging from the escaping electrons contributes significantly to the waveforms measured by antenna #1. Once the escaping electrons and ions expanded beyond the length of the antenna, signal $\delta V_{mono,1}$) relaxes back to sensing only the charge that has been collected on the SC. This means $\delta V_{mono,1} \cong (a_{1,0}^{exp} - a_{0,0}^{exp})\,(\delta Q_{i,col} - \delta Q_{e,col})$, where the last term is the net collected charge. The values of the relevant elastance matrix are $a_{0,0}^{exp} = 2.24 \times 10^{10} F^{-1}$ and $a_{1,0}^{exp} = 0.91 \times 10^{10} F^{-1}$, which provide the estimate for the ratio of $\delta V_{mono,1} \,/\, \delta V_{mono,2} = (a_{0,0}^{exp} - a_{1,0}^{exp}) \,/\, a_{0,0}^{exp} \cong 0.6$. The measured ratio is somewhat larger for the particular example shown; nevertheless, the model explains why the signal measured by antenna #1 drops below the $\delta V_{mono,2}$ signal at around $t = 30\mu s$. It will be show below that this is roughly the time for the cations to expand beyond the length of the antennas. The feature of signal $\delta V_{mono,1}$ crossing and dropping below signal $\delta V_{mono,2}$ is typical for all measurements taken in this configuration.

The start of the waveforms is similar to those observed by Nouzák et al. (2018) or those demonstrated in Section 6.1. Briefly, the sharp negative drop is known as the preshoot, and is due to the fast-escaping electrons that leave a net positive charge near the SC, which temporarily drives the SC potential to $\delta V_{SC} > 0$. After reaching a minimum, the waveform signals increase due to the escape of the slower cations. The rate of the increase, however, is different for the two signals. This is because antenna #1 also senses the induced charges from the cloud of escaping cations, as indicated in Figure 5.9. This effect also drives $\delta V_{mono,1}$ to be more positive than $\delta V_{mono,2}$) for the duration of the cation expansion over the length of the antennas. Once the escape of the electrons and cations is complete, the SC is left with a net negative charge. This is due to the difference in the properties of electron and cation clouds emerging from the impact plasma. While the cations are expanding in the form of a plume that moves away from the impact location, the electrons have an isotropic distribution. The latter results in the recollection of about half of the electrons by the SC for the investigated case of no bias potential applied on the elements. The charge collected on the SC discharges through the bias resistor with a characteristic time constant, as described in Section 5.2.

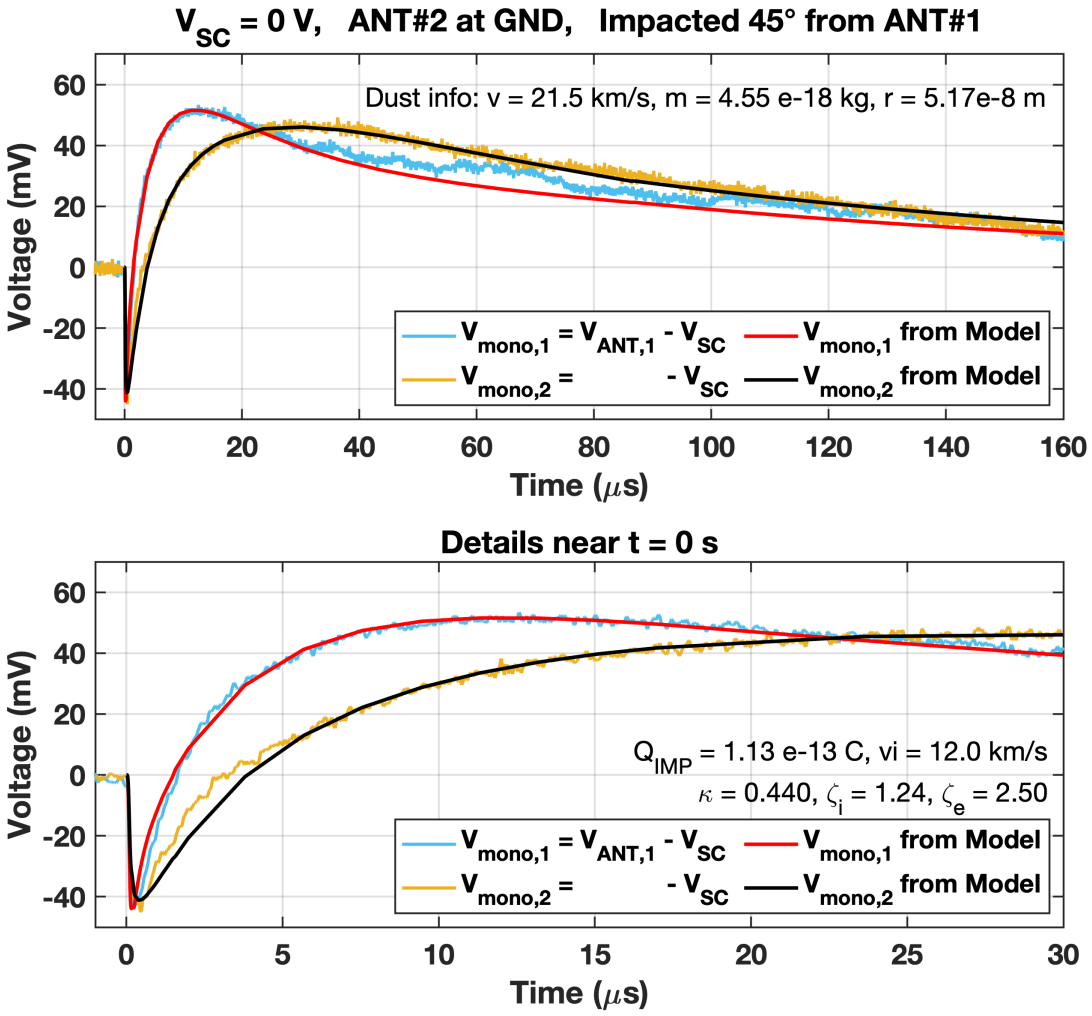

Figure 6.4: Typical waveforms measured in the laboratory for an impact location at 45° from antenna #1. The properties of the impacting dust particle are provided in the top panel. The bottom panel provides the details in the early phases of the impact plasma expansion. See text for more detail.

The model described above allows for fitting the waveforms and determining some of the key parameters of the impact plasma. For the data shown in Figure 6.4, these parameters are $Q_{IMP} = 1.13 \times 10^{-13}$ C, $\kappa = 0.44$, and $v_i = 12.0$ km/s. The latter two values are in good agreement with prior measurements, and electron expansion speed is set to $v_e \cong 10^3$ km/s (Shen et al., 2021a). The values of the two new parameters introduced in Equation 6.2 are $\zeta_e = 2.50$ and $\zeta_i = 1.24$. It would not be possible to properly match the negative and positive amplitudes of the $\delta V_{mono,1}$ waveform without these auxiliary parameters. The current numerical model allows treating the escaping electrons and cations as point charges only and are moving radially outward with constant velocities. This physical picture, however, is oversimplified. The electrons escaping from the plasma cloud have an isotropic distribution, and thus some fraction of the electrons will get in the close vicinity of the antenna. This results in a stronger induced charging signal than the model with the current geometric functions can reproduce. Similarly, parameter $\zeta_i > 1$ indicates that the cations also get closer to the antenna than they would from moving on a radial line. In other words, the fitting results indicate that the cations are expanding in form of a divergent plume rather than as a narrow pencil beam. The more detailed analysis of the data will require (1) having a solution for the geometric function fall all locations in the vicinity of the SC, and (2) employing realistic models for the expansion of the electrons and ions that would also allow calculating their charge densities as a function of time and location as presented in Equation 4.21.

6.2.3 Impacts at 10°

Figure 6.5 shows a set of typical waveforms for a dust impact location 10° offset from antenna #1. Many features are similar to the 45° case treated above. The obvious difference is the much more pronounced contribution from the induced charge signal on antenna #1, which is closest to the impact location, and so do the expanding plasma cloud. In addition, the model does not provide as good of an agreement with the data as in the 45° impact location. The impact location is in the close proximity of the antenna base (separated by about $1 - 1.5$ cm), and the diverging cation plume results in relatively large differences between the measurements and the simplified expansion

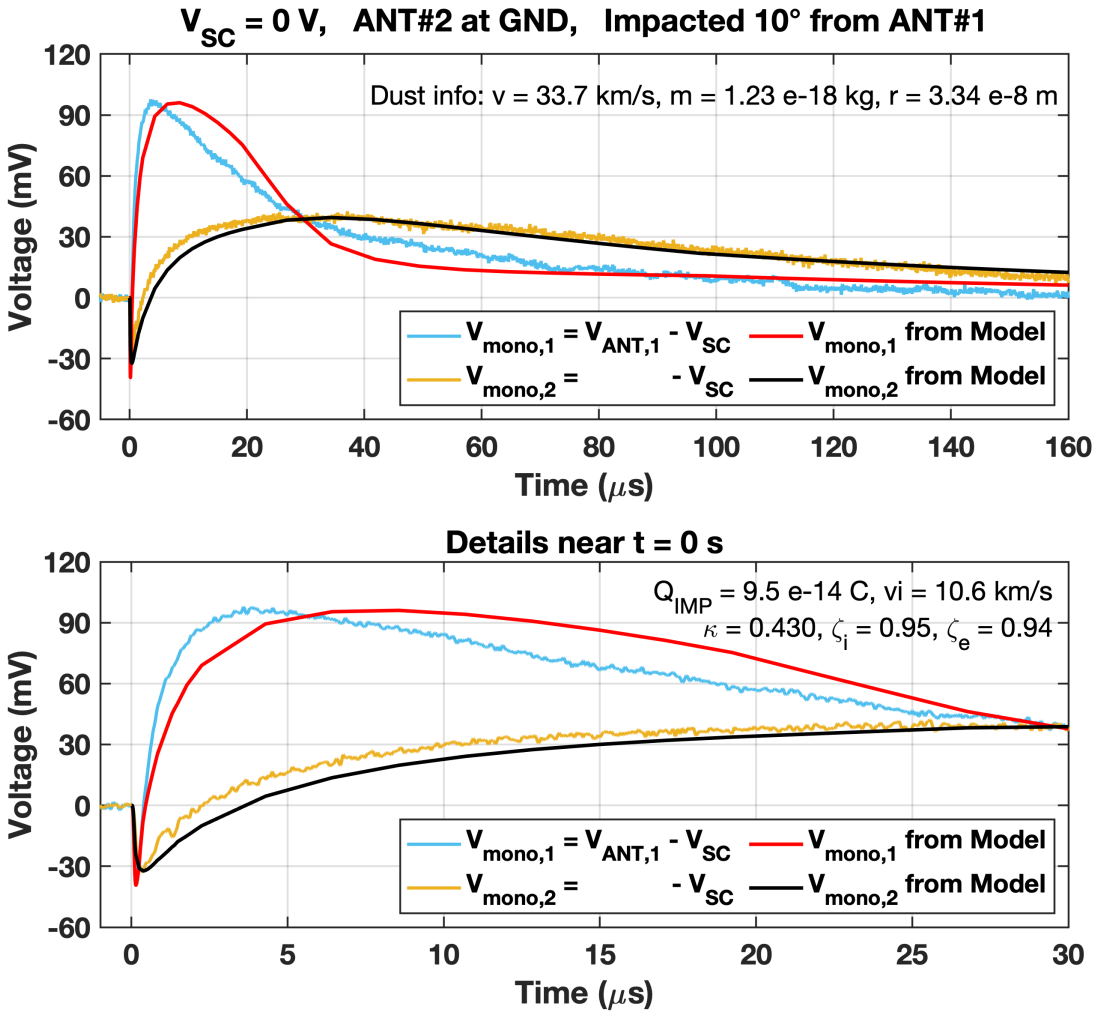

Figure 6.5: Typical waveforms measured in the laboratory for an impact location at 10° from antenna #1. The properties of the impacting dust particle are provided in the top panel. The bottom panel provides the details in the early phases of the impact plasma expansion. See text for more detail.

model. Cations in a conical expansion plume would get close to the antenna faster than in the case of a radial pencil beam that is moving close to parallel to the antenna. As a result, there is an ambiguity in determining the ion expansion speed from the fit. The "best" fit to the data in Figure 6.5 was guided by approximately matching the intersect point between the $\delta V_{mono,1}$ and $\delta V_{mono,2}$ signals at around $t = 30\,\mu s$.

The fitting parameters determined from the model are $Q_{IMP} = 9.5 \times 10^{-14}$ C, $v_i = 10.6$ km/s, and $\kappa = 0.43$, with the latter two in good agreement with the results for the 45° impact location. Both zeta parameters are close to unity, $\zeta_e = 0.94$ and $\zeta_i = 0.95$, meaning that the amplitudes of the waveforms are reproduced accurately by the model. Generally, the model provides a good match for the entire $\delta V_{mono,2}$ waveform and the beginning and the end of the $\delta V_{mono,1}$ waveform.

6.3 Impact Charge Yield Q_{IMP}

The impact charge, Q_{IMP}, is determined for each analyzed waveform. The impact charge is an important parameter as it is characteristic to the mass and speed of the dust particle, according to Equation 3.1. The amplitude of the main peak of the waveform is related to Q_{IMP}, but it is also affected by the effective temperatures of the positive and negative charge carriers (T_e and T_i), the geometric coefficient (κ), the fudge factors (ζ_e and ζ_i) as well as the discharge time constant (described in Section 4.4).

Figure 6.6 shows $Q_{IMP} \,/\, m$ as a function of impact speed for all waveforms analyzed in Section 6.1. These impact waveforms are collected using the Cassini SC model. Several observations ought to be made here. First, the $Q_{IMP} \,/\, m$ ratio scales with impact speed as $\sim v^{3.7}$, which is consistent with the $\sim v^{3.5 \pm 0.2}$ scaling from prior measurements over a wide impact speed range (Dietzel et al., 1973). The absolute value of the charge is about a factor of two lower, however. This can be explained by neglecting the coupling parameter Γ from Section 4.3. Since the potential developed on the SC from impact charge is also affecting the potential of the antenna through capacitive coupling, the measured signal $V_{meas}(t)$ is effectively reduced. The relatively large scatter of the $Q_{IMP} \,/\, m$ ratio is characteristic to impact ionization process (e.g., Horányi et al. (2014)).

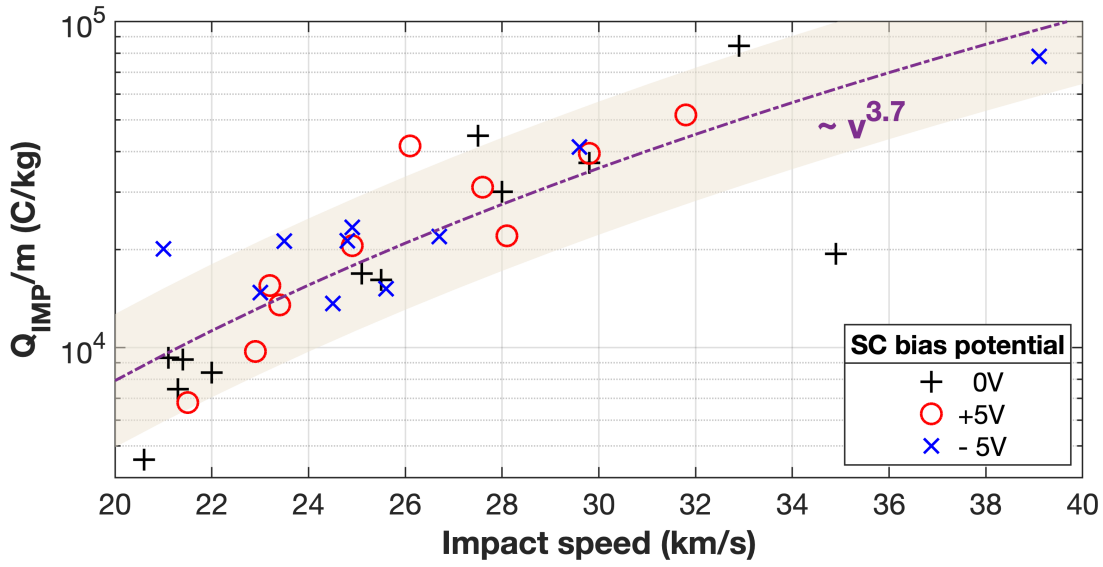

Figure 6.6: The normalized impact charge ($Q_{IMP}\,/\,m$) as a function of impact speed calculated for the three different spacecraft (SC) bias potentials. Colored background represents an error factor of 1.6 boundary for curve fitting.

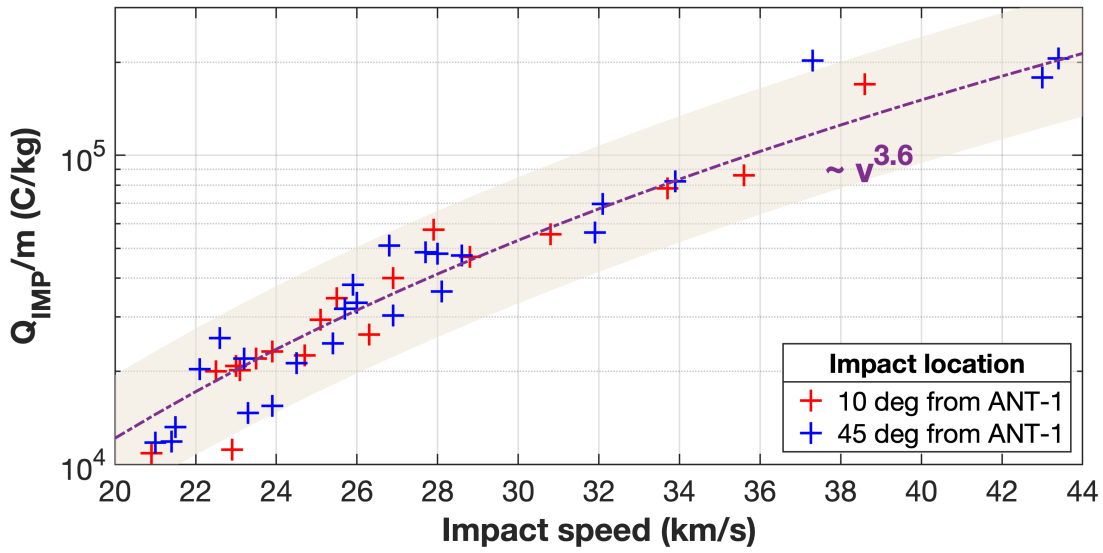

Figure 6.7: The normalized impact charge ($Q_{IMP}\,/\,m$) as a function of impact speed calculated for the two different impact locations on spacecraft with the spacecraft bias potentials at $V_{SC} = 0$ V. Colored background represents an error factor of 1.6 boundary for curve fitting.

An improved model fitting to waveforms collected in the spherical SC measurements have taken the capacitive coupling into account. Two sets of impact locations have been analyzed (10° and 45° offset from ANT−1 discussed in Section 6.2), as shown in Figure 6.7. The fitting result scales with impact velocity in the power of $\sim v^{3.6}$, which remains consistent with prior studies. The issue of the underestimated absolute value of the charge shown in Figure 6.6 has been resolved. It implies that the proposed electrostatic model allows obtaining preciser Q_{IMP} values, leading to a possibility for more reliable dust mass calculations. Note that the mass calculation of the dust particle with sufficient certainty remains a difficult task. Further charge yield measurements using the same W-target in this thesis may provide a reliable reference of scaling relation to link the fitted values of impact charge to dust mass calculations.

6.4 Dust Detection by Dipole Configuration

Figure 6.8 shows an overview of typical antenna signals measured for different impact locations between antennas #3 and #4. These antennas are configured as a dipole (Figure 5.5). Each column in Figure 6.8 correspond to the same impact location (10°, 30°, and 45°) that is measured from antenna #3. The applied bias voltages are 0 V, +5 V, and −5V in each row. In addition to the dipole signal, Figure 6.8 also shows the two monopole signals from antennas #1 and #2. All impact events shown are for speeds $\geq$ 20 km/s.

The monopole signals have the typical shapes dominated by the evolution of the voltages developed on the SC. Since the impact location is relatively far from antennas #1 and #2, the induced charging of these antennas is not significant (photo of spherical SC model in Figure 5.5). Bias voltage $V_{SC} = 0$ V allows the generated plasma cloud to expand freely upon impact. These monopole signals are similar to previous observations shown in Section 6.1 and 6.2. The monopole signal features are a preshoot and ion cloud expansion followed by SC discharging over hundreds of μs. Applying a bias voltage of $V_{SC} = 5$ V results in recollecting a larger fraction of electrons from the impact plasma and thus reduces the amplitude of the preshoot. Signal fitting allows estimating the effective electron temperature to be around $\sim$ 5.5 eV using Equation 4.2 and assuming $\kappa = 0.5$

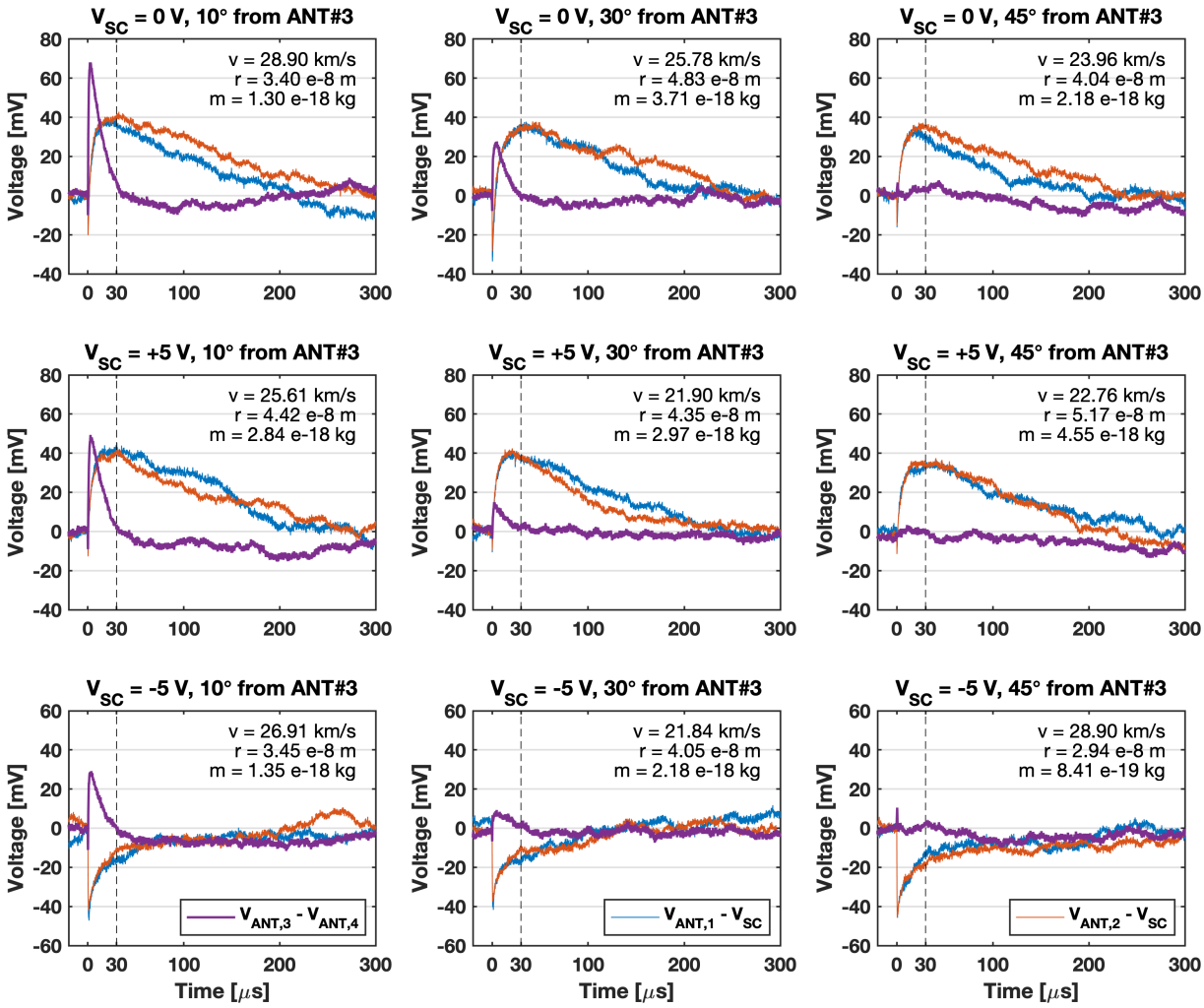

Figure 6.8: Dipole (purple) and monopole (blue and orange) antenna signals measured in the laboratory for three impact locations (10°, 30°, and 45°) and three different bias voltages (0 V, +5 V, and −5V). The impact speed, size and mass are provided for each particle. The vertical dashed line indicates 30 μs after the impact. See text for more detail.

as usual. This value is in reasonable agreement with that reported by Collette et al. (2016) and Nouzák et al. (2020). On the other hand, the $V_{SC} = -5$ V applied bias potential enhances the escape portion of electrons and decreases that of ions. The result shows a fast negative−going signal, followed by a slower recovery due to the escape of ion on time scales of a few tenths of μs. The effective ion temperature is estimated to be approximately ~ 5.1 eV using Equation 4.3 that is still in a reasonable agreement with the lower end values reported by Collette et al. (2016). A noteworthy feature in these events is that the net recollected charge is significantly reduced, thus suppressing the main amplitude of the waveform relative to the actual impact charge, Q_{IMP}.

On the other hand, the dipole antennas are not affected by the SC potential but are only sensitive to induced charging from the escaping electrons and ions. Hence, the shape of the dipole signal is also limited to the duration of the escape of slower species, i.e., the ions. In Figure 6.8, the vertical lines correspond to 30 μs. Given that the antennas are 30 cm in length and the ion expansion speed is approximately 10 km/s, these lines mark where the expanding plasma cloud passes by the antenna. The dipole measurements exhibit strong variation with impact location. At 10°, where the impact occurs in the closer vicinity of antenna #3, the dipole signal signals are pronounced and are larger than those monopole signals. At 30°, the dipole signals are still significant, while they are diminished at 45°. The latter is due to the symmetry of the system, where the induced charge signal is very similar on both antennas #3 and #4 (90° apart shown in Figure 5.5). Note that the amplitude of dipole signals at the same impact location will vary with the bias voltages on the SC. This is due to the induced charging on the antenna with respect to the charge amount of escaping ions. Hence, the negative bias potential will record the smaller amplitude of dipole measurements.

Overall, monopole measurements have an advantage in identifying the occurrence of dust impacts disregarding the variation of bias voltages on SC, while the dipole measurements can provide a good indication of impact locations. The former allows providing impact plasma parameters, for example, the impact charge, effective temperatures, and expansion speeds. The latter, however, would be limited by the development of ion cloud expansion. The suggestion is that an antenna in-

strument should take monopole measurements and do dipole processing later in order to obtain all essential parameters above to characterize the population information of dust particles (monopole) as well as the dynamics clue from impact locations (dipole) in space applications.

6.5 Characteristics of Low Speed Dust Impacts

Figure 6.9 shows the typical monopole signals measured for low-speed impacts ($\cong$ 5 km/s) with different bias voltages applied on the elements. In each case of bias voltages (0 V, +5 V, and −5 V), two individual impact events with larger amplitudes are provided. At the same time, the bottom row demonstrates the most common waveforms registered in the laboratory. The impact location is set to be 45° between two monopole antennas #1 and #2. From symmetry, it is expected that two monopole signals should be nearly identical. Statistically, about 5% of the waveforms in the investigated speed range generate large enough impact signals for unambiguous detection. Most of the waveforms would be challenging to identify on the noisy background without having the controlled laboratory settings that provide an expected time stamp of impact. The features of impact waveforms for low-speed impacts are qualitatively similar to high-speed impacts. The waveforms capture the preshoots, which means there are free electrons in the impact plasma. It is not immediately evident considering the kinetic energy difference is $\left(\frac{5\,\mathrm{km/s}}{20\,\mathrm{km/s}}\right)^2 = \frac{1}{16}$ with respect to the high-speed impacts ($\geq$ 20 km/s). In addition, at the bias potential of $V_{SC} = 0$ V, the escaping positive and negative charges are about the same. This implies that there is no main peak in the signal, resulting in the event become more difficult to identify as it does not have a characteristic shape. In other words, it represents that the geometric coefficient $\kappa = 0.5$ feature of the impact plasma is no longer valid. It is suggested that either $\kappa \simeq 1.0$ (i.e., no collected charges) or not all the ions will escape. Applying a bias voltage, especially +5 V, has a more significant effect in amplitudes on the waveforms than 20 km/s. It is unclear what this means in terms of effective temperatures, however.

Figure 6.10 shows the typical monopole signals measured on antenna #1 and #2 when the impact location is at 10° offset from the former. Two individual impact events are provided in

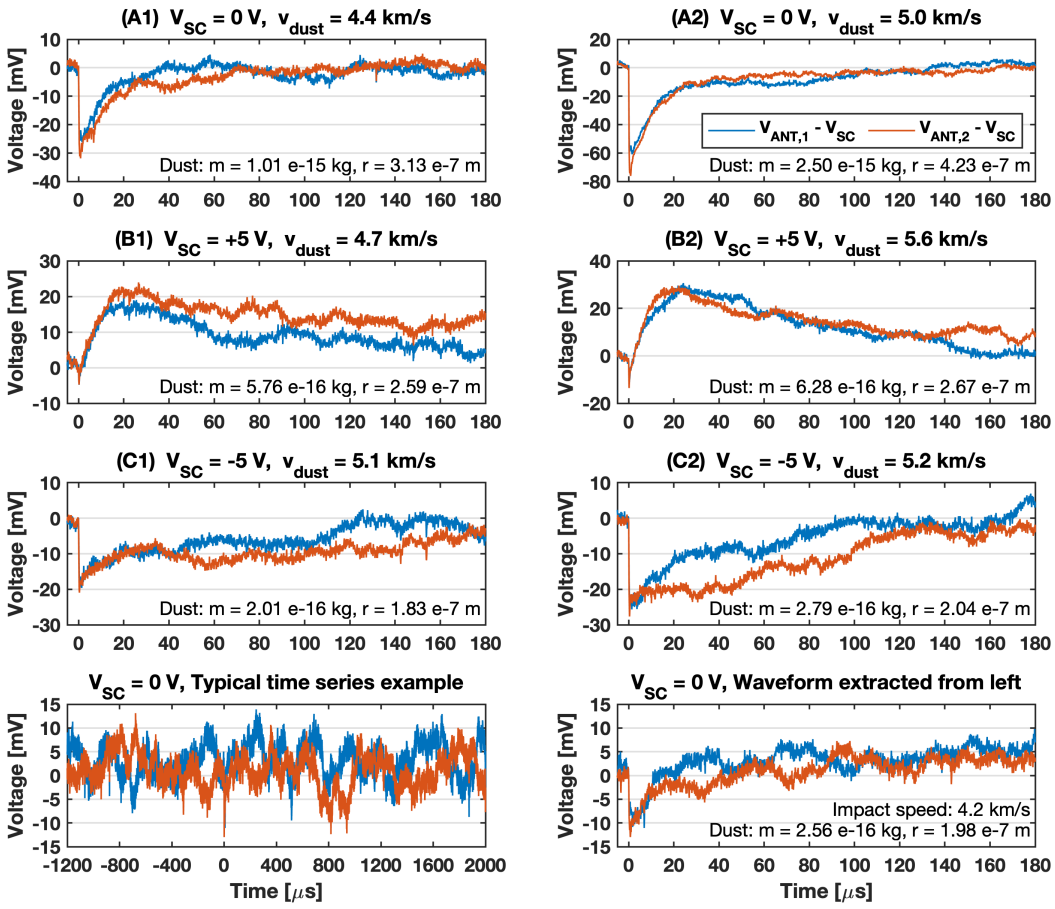

Figure 6.9: Typical monopole waveforms measured in the laboratory for low-speed particles ($\cong$ 5 km/s) at impact location at 45° between antenna #1 and #2 for three different bias voltages. The information of slow dust particles are provided. See text for more detail.

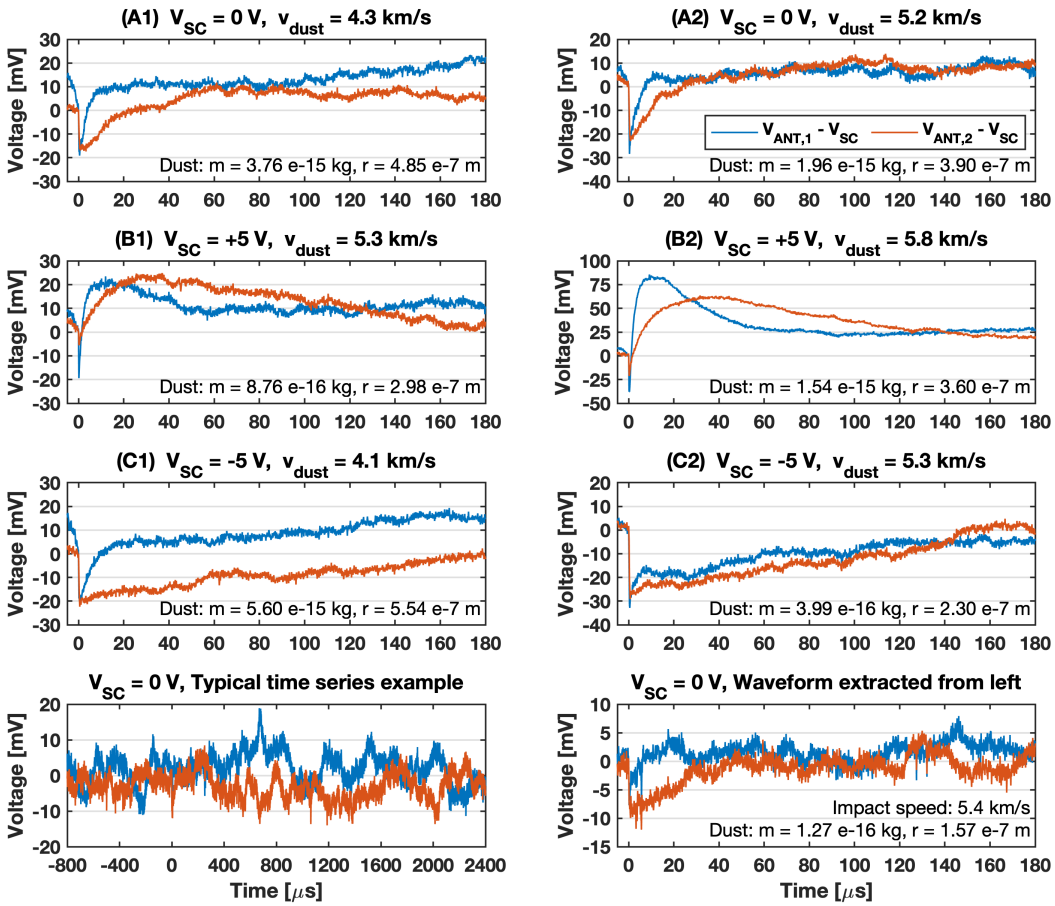

Figure 6.10: Typical monopole waveforms measured in the laboratory for 10° from antenna #1 for three different bias voltages. The information of slow dust particles (≅ 5km/s) are provided. See text for more detail.

each case of bias voltages (0 V, +5 V, and −5 V). It is expected to have more induced charging by escaping electrons and ions on monopole #1 signals than monopole #2 due to the geometry of antennas. Note that most of the impact waveforms are difficult to identify from the noisy background as the same situation described above.

In general, there are large variations between individual events, for example, comparing the three top left panels versus their right panels. First, the amplitudes of preshoot are different in two monopole signals due to the extra induced charging of electrons on antenna #1, as the same effect has been identified in Section 6.2. Second, each waveform shown in the top six panels registered the rise occurring earlier on monopole #1 than monopole #2. Besides, the induced charging from expanding ions seems to occur faster than 30 μs. Note that this 30 μs is denoted as a characteristic timescale for the expanding plasma cloud passes through by the antenna considering an ion expansion speed of approximately 10 km/s. However, it is unlikely that these ions generated upon low-speed impact may move $>$ 10 km/s. Instead, it implies that the angular distribution of the ion plume may behave more divergent than that generated in high-speed impacts.

6.6 Signal Variations of Dust Compositions

Figure 6.11 provides the typical monopole signals for aluminum dust impacting tungsten target registered by monopole #1 and #2. The presented waveforms provide the comparison of two impact locations (45° and 10° offset from antenna #1) and three bias voltages (0 V, +5 V, and −5 V). The impact speeds are limited to $\geq$ 20 km/s in order to be comparable to prior studies in Section 6.2 and Nouzák et al. (2018, 2020).

As previously observed, the features, including preshoot and ion cloud expansion followed by the SC discharging, occur as usual. And, the effective temperatures of electrons and ions can be fitted using the proposed electrostatic model and obtained $\sim$ 4.6 eV and $\sim$ 5.7 eV, respectively (by applying Equation (4.2) and (4.3)). These values are consistent with results from Collette et al. (2016). In general, the impact signals appear to show no significant variations depending on the dust composition. It is reconcilable to the works reported by Auer and Sitte (1968) and Adams

and Smith (1971) who found that the impact response mostly associates with the target material rather than the composition of dust particles.

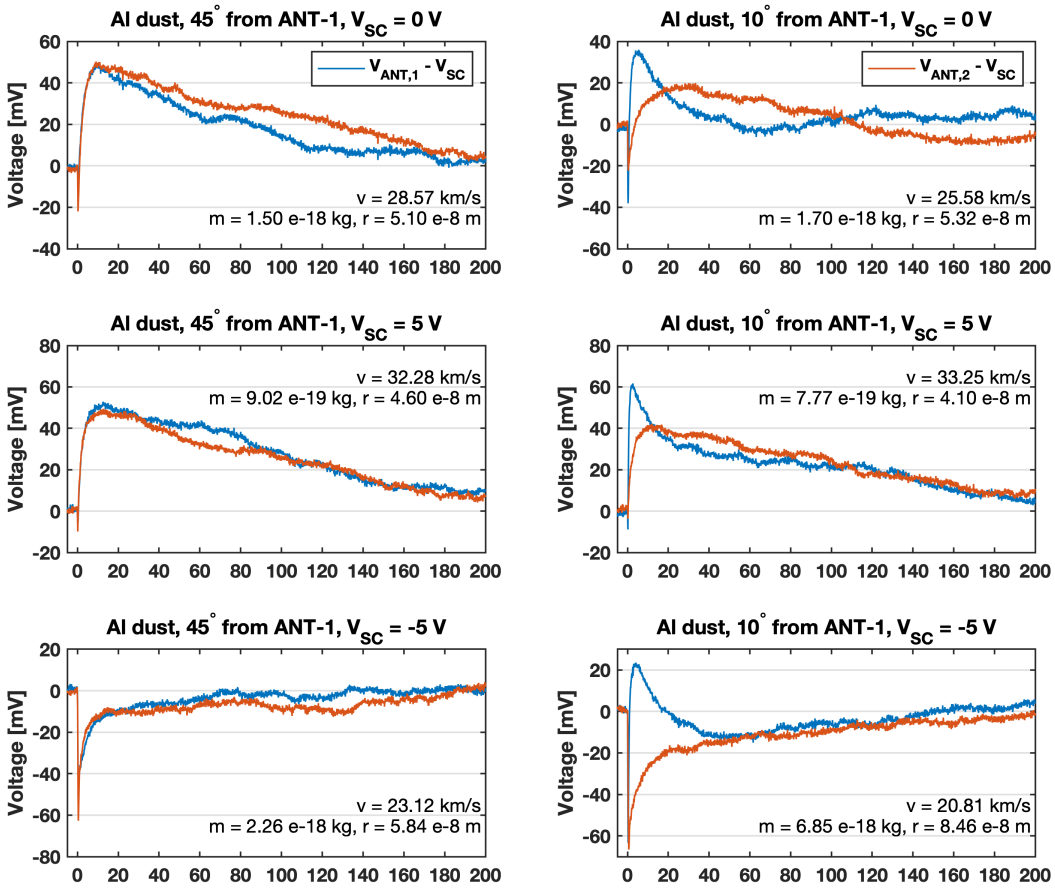

Figure 6.11: Typical monopole waveforms measured in the laboratory for 45° and 10° from antenna #1 under three different bias voltages. The dust-target combination is Aluminum to Tungsten (Al-W). The information of dust particles are provided.

6.7 In Space Applications

In applying the presented electrostatic model to dust impact signals from space missions, the ambient plasma environment is the crux that alters the spacecraft floating potential as well as the discharging time constant through the balance of charging currents. First of all, the capacitance matrix should be amended for space missions as discussed in Section 5.4.2. Note that unlike the laboratory measurements treating the vacuum chamber as a grounded wall, the chassis ground on spacecraft is considered the only electrical ground in space. This may affect the capacitance values of elements onboard. Nevertheless, an appropriate electrostatic simulation and detailed capacitance measurements before launch can provide critical information for examining the antenna signal waveforms. Conversely, fitting the measured signals with an electrostatic model provides an alternative way to obtain spacecraft potential and information of the ambient environment. The challenges and solutions of analyzing signals collected by various missions with antenna instruments onboard will be discussed.

Typical challenges in dust detection by antenna instruments include: (1) Signal coupling between elements in the SC−antenna system are not fully characterized. (2) Signal variations due to different impact locations were yet fully understood. (3) The calculation of the mass of the impacting particle with sufficient certainty. (4) The sampling rate of instrument may not fast enough to register the preshoot feature, a distinct indicator of impact. However, the proposed generalized model in this thesis have quantified the signal coupling of antenna instrument via employing a capacitance matrix and characterized the induced charging associated with impact locations through geometry analysis and electrostatic simulation. Being able to (a) distinguish various components contributing to the impact waveform and to (b) solve the capacitive coupling between the spacecraft and antennas (Chapter 4), the calculation of impact charge yield thus is improved (Section 6.3). Considering the bandwidth and sampling rate of electronics, modern antenna instruments carried by STEREO, Parker Solar Probe, and Solar Orbiter have reported the registration of preshoot features in the waveforms. Hence, the data from these missions are

first recommended to apply the proposed electrostatic model for validation and investigations. In addition, the Cassini mission had a dedicated dust instrument onboard, followed by the antenna instruments. For future application, Fitting the electrostatic model to waveforms collected by Radio and Plasma Wave Science instrument and comparing the results with dedicated Cosmic Dust Analyzer are expected to help reconcile the data analyses and our understanding of dust environment in the Saturnian system.

Chapter 7

Summary and Conclusions

The presented work has been developed in steps with increasing complexity. First, a simplified model was developed applicable to the case where the antenna is far from the impact location. This model was described as fully analytical and was verified against the laboratory data. The full model is then proposed to employ the geometric functions to account for the generation of induced charge signals on the antennas. The laboratory measurements have shown that the induced charge is significant even for impacts relatively far from the antenna base. This has several important consequences: (1) The model can be used to analyze the wide variety of expected waveforms from the dust impact signals as a function of impact location (and other parameters, e.g., those of the ambient plasma). Such analysis would be useful for recognizing valid dust impact events. (2) There is a promising outlook that the detailed analysis of the waveforms detected by multiple antennas can be used to constrain the impact location on the SC body, which in turn could provide useful information on the orbital elements of the impacting particle. The induced charge signal from a plasma plume is unique for each antenna and impact location. The variations between antenna waveforms could thus reveal the origin of dust particles. (3) The previous point can be turned around, and antenna waveforms for a known dust impact location can be used to characterize the properties of dust impact plasma plumes. Our understanding of dust impact plasmas is surprisingly limited, and antennas may provide an elegant way to learn about the expansion characteristics of the electrons and cations. This method would be applicable both for laboratory measurements and data collected by space missions. (4) It is found that dust impact detection for antennas

operating in dipole mode could be sensitive to impact locations but limited by the antenna sensing aperture and the angular characteristic of impact plasma cloud. The presented model could be employed to analyze the variety of impact waveforms expected in this mode, which are significantly different from those measured in the monopole mode. In additional measurements of low-speed dust impacts and dust composition, there are three major statements: (1) The surface ionization and partial-developed impact plasma cloud lead to a complex variety in measured waveforms. (2) The relatively small generated impact charge in low-speed impacts consequently make the amplitudes of measured waveforms small and challenging to identify from the noise level. (3) The impact charge and measured waveforms depend primarily on the target materials rather than the dust composition, as previous studies indicated. There are no significant signal variations between iron or aluminum dust in laboratory measurements.

This thesis provides a general electrostatic model for understanding the generation of the transient voltage perturbations detected by antenna instruments due to dust impacts. The analyses demonstrate agreements between the presented model and the data collected in the laboratory using spacecraft models and the dust accelerator facility. Fitting the model to the data allows for the determination of impact plasma parameters. The four key elements of this model are the following: First, the impact charge can be subdivided into fractions of escaping and collected charges for both the negative (electrons) and positive (cation) components. Second, the escaping/collected fractions of the impact cloud are determined by the energetics of the system and the nature of the impact plasma cloud. The energetics means that escaping/collected fractions are determined by the potential of the spacecraft and the effective temperatures of the charged species. Furthermore, the presented work implies that it is reasonable to think about the impact plasma as a plume of ions expanding away from the impact location while the electrons acquire an isotropic distribution during the expansion. Third, the voltages developing on the antenna and spacecraft elements can be understood based on electrostatics. This means that (a) direct charging due to collected fractions from the impact plasma and (b) induced charging due to escaping fractions of the impact plasma are identified as two primary mechanisms for antenna signal generation. The matrix form of the

model provides a convenient way to track the interaction between spacecraft and antennas, thus calculating the voltage differences therein. In addition, the elastance matrix offers a straightforward course of calculating the effective capacitances of the elements needed to convert the measured voltages to charge appropriately, or vice versa. And fourth, the restoration driven by photoelectron emission and the ambient plasma environment to equilibrium potential needs to be considered. The corresponding discharging currents may and likely will significantly limit the amplitude of the signal. Thus, detailed analysis is needed to convert the antenna signals to impact charge for obtaining the accurate mass of dust particles if impact speed is known. Overall, the presented model will improve data analysis fidelity and calculate the impact charge from the dust particle, which in turn allows for the determination of its mass. This is, of course, under the assumption that we know the impact speed, spacecraft potential, and the effective temperatures of the electrons and cations of the impact plasma. One of the fundamentals of the model is the recognition that the collected and induced charges can be treated similarly. If desired, the model can be easily augmented to include the charge collection by the antennas for even higher fidelity. This may be significant for dust impacts occurring in the close vicinity of an antenna base.

Bibliography

V. I. Abramov, D. R. Bandura, V. P. Ivanov, and A. A. Sysoev. Energy and Angular Characteristics of Ions Emitted under Accelerated Microparticle Collision with Targets. PISMA V ZHURNAL TEKHNICHESKOI FIZIKI, 17(6):1–4, MAR 26 1991. ISSN 0320-0116.

N. Adams and D. Smith. Studies of microparticle impact phenomena leading to the development of a highly sensitive micrometeoroid detector. Planetary and Space Science, 19(2):195–204, 1971. ISSN 0032-0633. doi: https://doi.org/10.1016/0032-0633(71)90199-1.

M. G. Aubier, N. Meyer-Vernet, and B. M. Pedersen. Shot noise from grain and particle impacts in saturn's ring plane. Geophysical Research Letters, 10(1):5–8, 1983. doi: https://doi.org/10.1029/GL010i001p00005.

A. Auer and K. Sitte. Detection technique for micrometeoroids using impact ionization. Earth and Planetary Science Letters, 4(2):178–183, 1968. ISSN 0012-821X. doi: https://doi.org/10.1016/0012-821X(68)90013-7.

S. Auer. Instrumentation, pages 385–444. Springer Berlin Heidelberg, Berlin, Heidelberg, 2001. ISBN 978-3-642-56428-4. doi: 10.1007/978-3-642-56428-4_9.

S. D. Bale, R. Ullrich, K. Goetz, N. Alster, B. Cecconi, M. Dekkali, N. R. Lingner, W. Macher, R. E. Manning, J. McCauley, S. J. Monson, T. H. Oswald, and M. Pulupa. The Electric Antennas for the STEREO/WAVES Experiment, pages 529–547. Springer New York, New York, NY, 2008. ISBN 978-0-387-09649-0. doi: 10.1007/978-0-387-09649-0_17.

S. D. Bale, K. Goetz, P. R. Harvey, P. Turin, J. W. Bonnell, T. Dudok de Wit, R. E. Ergun, R. J. MacDowall, M. Pulupa, M. Andre, M. Bolton, J.-L. Bougeret, T. A. Bowen, D. Burgess, C. A. Cattell, B. D. G. Chandran, C. C. Chaston, C. H. K. Chen, M. K. Choi, J. E. Connerney, S. Cranmer, M. Diaz-Aguado, W. Donakowski, J. F. Drake, W. M. Farrell, P. Fergeau, J. Fermin, J. Fischer, N. Fox, D. Glaser, M. Goldstein, D. Gordon, E. Hanson, S. E. Harris, L. M. Hayes, J. J. Hinze, J. V. Hollweg, T. S. Horbury, R. A. Howard, V. Hoxie, G. Jannet, M. Karlsson, J. C. Kasper, P. J. Kellogg, M. Kien, J. A. Klimchuk, V. V. Krasnoselskikh, S. Krucker, J. J. Lynch, M. Maksimovic, D. M. Malaspina, S. Marker, P. Martin, J. Martinez-Oliveros, J. McCauley, D. J. McComas, T. McDonald, N. Meyer-Vernet, M. Moncuquet, S. J. Monson, F. S. Mozer, S. D. Murphy, J. Odom, R. Oliverson, J. Olson, E. N. Parker, D. Pankow, T. Phan, E. Quataert, T. Quinn, S. W. Ruplin, C. Salem, D. Seitz, D. A. Sheppard, A. Siy, K. Stevens, D. Summers, A. Szabo, M. Timofeeva, A. Vaivads, M. Velli, A. Yehle, D. Werthimer, and J. R. Wygant. The fields instrument suite for solar probe plus. Space Science Reviews, 204(1):49–82, Dec 2016. ISSN 1572-9672. doi: 10.1007/s11214-016-0244-5.

R. E. Barrington, J. S. Belrose, and D. A. Keeley. Very-low-frequency noise bands observed by the alouette 1 satellite. Journal of Geophysical Research (1896-1977), 68(24):6539–6541, 1963. doi: https://doi.org/10.1029/JZ068i024p06539.

J. L. Bougeret, K. Goetz, M. L. Kaiser, S. D. Bale, P. J. Kellogg, M. Maksimovic, N. Monge, S. J. Monson, P. L. Astier, S. Davy, M. Dekkali, J. J. Hinze, R. E. Manning, E. Aguilar-Rodriguez, X. Bonnin, C. Briand, I. H. Cairns, C. A. Cattell, B. Cecconi, J. Eastwood, R. E. Ergun, J. Fainberg, S. Hoang, K. E. J. Huttunen, S. Krucker, A. Lecacheux, R. J. MacDowall, W. Macher, A. Mangeney, C. A. Meetre, X. Moussas, Q. N. Nguyen, T. H. Oswald, M. Pulupa, M. J. Reiner, P. A. Robinson, H. Rucker, C. Salem, O. Santolik, J. M. Silvis, R. Ullrich, P. Zarka, and I. Zouganelis. S/waves: The radio and plasma wave investigation on the stereo mission. Space Science Reviews, 136(1):487–528, Apr 2008. ISSN 1572-9672. doi: 10.1007/s11214-007-9298-8.

J. A. Burns, P. L. Lamy, and S. Soter. Radiation forces on small particles in the solar system. Icarus, 40:1–48, Oct. 1979. doi: 10.1016/0019-1035(79)90050-2.

J. A. Burns, D. P. Hamilton, and M. R. Showalter. Dusty Rings and Circumplanetary Dust: Observations and Simple Physics, pages 641–725. Springer Berlin Heidelberg, Berlin, Heidelberg, 2001. ISBN 978-3-642-56428-4. doi: 10.1007/978-3-642-56428-4_13.

Y. L. Chow and M. M. Yovanovich. The shape factor of the capacitance of a conductor. Journal of Applied Physics, 53(12):8470–8475, 1982. doi: 10.1063/1.330495.

A. Collette, E. Grün, D. Malaspina, and Z. Sternovsky. Micrometeoroid impact charge yield for common spacecraft materials. Journal of Geophysical Research: Space Physics, 119(8):6019–6026, 2014. ISSN 2169-9402. doi: 10.1002/2014ja020042.

A. Collette, G. Meyer, D. Malaspina, and Z. Sternovsky. Laboratory investigation of antenna signals from dust impacts on spacecraft. Journal of Geophysical Research: Space Physics, 120 (7):5298–5305, 2015. doi: https://doi.org/10.1002/2015JA021198.

A. Collette, D. M. Malaspina, and Z. Sternovsky. Characteristic temperatures of hypervelocity dust impact plasmas. Journal of Geophysical Research: Space Physics, 121(9):8182–8187, 2016. doi: https://doi.org/10.1002/2015JA022220.

A. C. M. de Queiroz. Capacitance calculations, 2012.

E. Di Lorenzo. The maxwell capacitance matrix. http//www. fastfieldsolver. com, 2011.

H. Dietzel, G. Eichhorn, H. Fechtig, E. Grun, H. J. Hoffmann, and J. Kissel. The HEOS 2 and HELIOS micrometeoroid experiments. Journal of Physics E: Scientific Instruments, 6(3):209–217, mar 1973. doi: 10.1088/0022-3735/6/3/008.

S. Drapatz and K. W. Michel. Theory of shock-wave ionization upon high-velocity impact of micrometeorites. Zeitschrift für Naturforschung A, 29(6):870–879, 1974. doi: 10.1515/zna-1974-0606.

M. Dubin. Meteoritic dust measured from explorer i. Planetary and Space Science, 2(2):121–129, 1960. ISSN 0032-0633. doi: https://doi.org/10.1016/0032-0633(60)90006-4.

R. E. Ergun, S. Tucker, J. Westfall, K. A. Goodrich, D. M. Malaspina, D. Summers, J. Wallace, M. Karlsson, J. Mack, N. Brennan, B. Pyke, P. Withnell, R. Torbert, J. Macri, D. Rau, I. Dors, J. Needell, P.-A. Lindqvist, G. Olsson, and C. M. Cully. The axial double probe and fields signal processing for the mms mission. Space Science Reviews, 199(1):167–188, Mar 2016. ISSN 1572-9672. doi: 10.1007/s11214-014-0115-x.

L. A. Fielding, J. K. Hillier, M. J. Burchell, and S. P. Armes. Space science applications for conducting polymer particles: synthetic mimics for cosmic dust and micrometeorites. Chem. Commun., 51:16886–16899, 2015. doi: 10.1039/C5CC07405C.

P. C. Frisch, J. M. Dorschner, J. Geiss, J. M. Greenberg, E. Grun, M. Landgraf, P. Hoppe, A. P. Jones, W. Kratschmer, T. J. Linde, G. E. Morfill, W. Reach, J. D. Slavin, J. Svestka, A. N. Witt, and G. P. Zank. Dust in the local interstellar wind. The Astrophysical Journal, 525(1):492–516, nov 1999. doi: 10.1086/307869.

E. Grün. Impact ionization from gold, aluminum and PCB-Z. In T. D. Guyenne, editor, ESA Special Publication, volume 224 of ESA Special Publication, pages 39–41, Jan. 1984.

E. Grün, H. Zook, H. Fechtig, and R. Giese. Collisional balance of the meteoritic complex. Icarus, 62(2):244–272, 1985. ISSN 0019-1035. doi: https://doi.org/10.1016/0019-1035(85)90121-6.

E. Grün, H. A. Zook, M. Baguhl, A. Balogh, S. J. Bame, H. Fechtig, R. Forsyth, M. S. Manner, M. Horanyi, J. Kissel, B.-A. Lindblad, D. Linkert, G. Linkert, I. Mann, J. A. M. McDonnell, G. E. Morfill, J. L. Phillips, C. Polanskey, G. Schwehm, N. Siddique, P. Staubach, J. Svestka, and A. Taylor. Discovery of jovian dust streams and interstellar grains by the ulysses spacecraft. Nature, 362(6419):428–430, Apr 1993. ISSN 1476-4687. doi: 10.1038/362428a0.

E. Grün, S. Pawlinka, and R. Srama. Dust accelerator tests with Cassini RPWS samples. Max-Planck-Institut für Kernphysik, 2007.

D. Gurnett, E. Grün, D. Gallagher, W. Kurth, and F. Scarf. Micron-sized particles detected near saturn by the voyager plasma wave instrument. Icarus, 53(2):236–254, 1983. ISSN 0019-1035. doi: https://doi.org/10.1016/0019-1035(83)90145-8.

D. A. Gurnett. Principles of Space Plasma Wave Instrument Design, pages 121–136. American Geophysical Union (AGU), 1998. ISBN 9781118664391. doi: https://doi.org/10.1002/9781118664391.ch14.

D. A. Gurnett, W. S. Kurth, F. L. Scarf, J. A. Burns, J. N. Cuzzi, and E. Grün. Micron-sized particle impacts detected near uranus by the voyager 2 plasma wave instrument. Journal of Geophysical Research: Space Physics, 92(A13):14959–14968, 1987. doi: https://doi.org/10.1029/JA092iA13p14959.

D. A. Gurnett, J. A. Ansher, W. S. Kurth, and L. J. Granroth. Micron-sized dust particles detected in the outer solar system by the voyager 1 and 2 plasma wave instruments. Geophysical Research Letters, 24(24):3125–3128, 1997. doi: https://doi.org/10.1029/97GL03228.

D. A. Gurnett, W. S. Kurth, D. L. Kirchner, G. B. Hospodarsky, T. F. Averkamp, P. Zarka, A. Lecacheux, R. Manning, A. Roux, P. Canu, and et al. The cassini radio and plasma wave investigation. Space Science Reviews, 114(1-4):395–463, 2004. doi: 10.1007/s11214-004-1434-0.

B. A. S. Gustafson. Physics of zodiacal dust. Annual Review of Earth and Planetary Sciences, 22 (1):553–595, 1994. doi: 10.1146/annurev.ea.22.050194.003005.

J. K. Hillier, Z. Sternovsky, S. P. Armes, L. A. Fielding, F. Postberg, S. Bugiel, K. Drake, R. Srama, A. T. Kearsley, and M. Trieloff. Impact ionisation mass spectrometry of polypyrrole-coated pyrrhotite microparticles. Planetary and Space Science, 97:9–22, 2014. ISSN 0032-0633. doi: https://doi.org/10.1016/j.pss.2014.04.008.

T. Hirai, H. Yano, M. Fujii, S. Hasegawa, N. Moriyama, C. Okamoto, and M. Tanaka. Data screening and reduction in interplanetary dust measurement by ikaros-aladdin. Advances in Space Research, 59(6):1450–1459, 2017. ISSN 0273-1177. doi: https://doi.org/10.1016/j.asr.2016.12.023.

K. Hornung and J. Kissel. On shock wave impact ionization of dust particles. Astronomy and Astrophysics, 291:324–336, Nov. 1994.

K. Hornung, Y. Malama, and K. Thoma. Modeling of the very high velocity impact process with respect to in-situ ionization measurements. Advances in Space Research, 17(12):77–86, 1996. ISSN 0273-1177. doi: https://doi.org/10.1016/0273-1177(95)00762-4.

M. Horányi. Charged dust dynamics in the solar system. Annual Review of Astronomy and Astrophysics, 34(1):383–418, 1996. doi: 10.1146/annurev.astro.34.1.383.

M. Horányi. Dust streams from jupiter and saturn. Physics of Plasmas, 7(10):3847–3850, 2000. doi: 10.1063/1.1288909.

M. Horányi, Z. Sternovsky, M. Lankton, C. Dumont, S. Gagnard, D. Gathright, E. Grün, D. Hansen, D. James, S. Kempf, and et al. The lunar dust experiment (ldex) onboard the lunar atmosphere and dust environment explorer (ladee) mission. Space Science Reviews, 185(1-4):93–113, 2014. doi: 10.1007/s11214-014-0118-7.

J. D. Jackson. Classical electrodynamics. Wiley, New York, NY, 3rd ed. edition, 1999. ISBN 9780471309321.

E. C. Jordan. Electromagnetic waves and radiating systems. American Journal of Physics, 19(8): 477–478, 1951. doi: 10.1119/1.1933056.

P. J. Kellogg, K. Goetz, and S. J. Monson. Dust impact signals on the wind spacecraft. Journal of Geophysical Research: Space Physics, 121(2):966–991, 2016. doi: https://doi.org/10.1002/2015JA021124.

P. J. Kellogg, K. Goetz, and S. J. Monson. Sign of the dust impact-antenna coupling cloud. Journal of Geophysical Research: Space Physics, 123(5):3273–3276, 2018a. doi: https://doi.org/10.1029/2017JA025173.

P. J. Kellogg, K. Goetz, and S. J. Monson. Are stereo single hits dust impacts? Journal of Geophysical Research: Space Physics, 123(9):7211–7219, 2018b. doi: https://doi.org/10.1029/2018JA025554.

S. Kempf, R. Srama, M. Horányi, M. Burton, S. Helfert, G. Moragas-Klostermeyer, M. Roy, and E. Grün. High-velocity streams of dust originating from saturn. Nature, 433(7023):289–291, Jan 2005. ISSN 1476-4687. doi: 10.1038/nature03218.

J. Kissel and F. R. Krueger. Ion formation by impact of fast dust particles and comparison with related techniques. Applied Physics A, 42(1):69–85, Jan 1987. ISSN 1432-0630. doi: 10.1007/BF00618161.

S. Kočiščák, A. Fredriksen, M. DeLuca, J. Pavlů, and Z. Sternovsky. Effective temperatures of olivine dust impact plasmas. IEEE Transactions on Plasma Science, 48(12):4298–4304, 2020. doi: 10.1109/TPS.2020.3033578.

F. Krueger. Ion formation by high- and medium-velocities dust impacts from laboratory measurements and halley results. Advances in Space Research, 17(12):71–75, 1996. ISSN 0273-1177. doi: https://doi.org/10.1016/0273-1177(95)00761-3.

H. Kruger, E. Grun, A. Heck, and S. Lammers. Analysis of the sensor characteristics of the galileo dust detector with collimated jovian dust stream particles. Planetary and Space Science, 47: 1015–1028, 1999.

W. Kurth, T. Averkamp, D. Gurnett, and Z. Wang. Cassini rpws observations of dust in saturn's e ring. Planetary and Space Science, 54(9):988–998, 2006. ISSN 0032-0633. doi: https://doi.org/10.1016/j.pss.2006.05.011. Physics of Dusty Rings.

N. Lee, S. Close, D. Lauben, I. Linscott, A. Goel, T. Johnson, J. Yee, A. Fletcher, R. Srama, S. Bugiel, A. Mocker, P. Colestock, and S. Green. Measurements of freely-expanding plasma from hypervelocity impacts. International Journal of Impact Engineering, 44:40–49, 2012. ISSN 0734-743X. doi: https://doi.org/10.1016/j.ijimpeng.2012.01.002.

C. Leinert, I. Richter, E. Pitz, and B. Planck. The zodiacal light from 1.0 to 0.3 au as observed by the helios space probes. Astronomy and Astrophysics, 103:177–188, 1981.

P.-A. Lindqvist, G. Olsson, R. B. Torbert, B. King, M. Granoff, D. Rau, G. Needell, S. Turco, I. Dors, P. Beckman, J. Macri, C. Frost, J. Salwen, A. Eriksson, L. Åhlén, Y. V. Khotyaintsev, J. Porter, K. Lappalainen, R. E. Ergun, W. Wermeer, and S. Tucker. The spin-plane double probe electric field instrument for mms. Space Science Reviews, 199(1):137–165, Mar 2016. ISSN 1572-9672. doi: 10.1007/s11214-014-0116-9.

D. M. Malaspina, M. Horányi, A. Zaslavsky, K. Goetz, L. B. Wilson III, and K. Kersten. Interplanetary and interstellar dust observed by the wind/waves electric field instrument. Geophysical Research Letters, 41(2):266–272, 2014. doi: https://doi.org/10.1002/2013GL058786.

D. M. Malaspina, J. R. Szalay, P. Pokorný, B. Page, S. D. Bale, J. W. Bonnell, T. D. de Wit, K. Goetz, K. Goodrich, P. R. Harvey, R. J. MacDowall, and M. Pulupa. In situ observations of interplanetary dust variability in the inner heliosphere. The Astrophysical Journal, 892(2):115, apr 2020. doi: 10.3847/1538-4357/ab799b.

I. Mann, M. Wilck, and E. Grün. Analysis of ulysses dust measurements within the asteroid belt. International Astronomical Union Colloquium, 150:19–22, 1996. doi: 10.1017/S0252921100501195.

I. Mann, H. Kimura, D. A. Biesecker, B. T. Tsurutani, E. GrÃŒn, R. B. McKibben, J.-C. Liou, R. M. MacQueen, T. Mukai, M. Guhathakurta, and P. Lamy. Dust near the sun. Space Science Reviews, 110(3):269–305, Jan 2004. ISSN 1572-9672. doi: 10.1023/B:SPAC.0000023440.82735.ba.

I. Mann, M. Köhler, H. Kimura, A. Cechowski, and T. Minato. Dust in the solar system and in extra-solar planetary systems. The Astronomy and Astrophysics Review, 13(3):159–228, Jun 2006. ISSN 1432-0754. doi: 10.1007/s00159-006-0028-0.

I. Mann, L. Nouzák, J. Vaverka, T. Antonsen, Å. Fredriksen, K. Issautier, D. Malaspina, N. Meyer-Vernet, J. Pavlů, Z. Sternovsky, J. Stude, S. Ye, and A. Zaslavsky. Dust observations with antenna measurements and its prospects for observations with parker solar probe and solar orbiter. Annales Geophysicae, 37(6):1121–1140, 2019. doi: 10.5194/angeo-37-1121-2019.

J. C. Maxwell. A treatise on electricity and magnetism, volume 1. Oxford: Clarendon Press, 1873.

N. McBride and J. McDonnell. Meteoroid impacts on spacecraft:: sporadics, streams, and the 1999 leonids. Planetary and Space Science, 47(8):1005–1013, 1999. ISSN 0032-0633. doi: https://doi.org/10.1016/S0032-0633(99)00023-9.

N. Meyer-Vernet, M. G. Aubier, and B. M. Pedersen. Voyager 2 at uranus: Grain impacts in the ring plane. Geophysical Research Letters, 13(7):617–620, 1986. doi: https://doi.org/10.1029/GL013i007p00617.

N. Meyer-Vernet, A. Lecacheux, M. L. Kaiser, and D. A. Gurnett. Detecting nanoparticles at radio frequencies: Jovian dust stream impacts on cassini/rpws. Geophysical Research Letters, 36(3), 2009. doi: https://doi.org/10.1029/2008GL036752.

N. Meyer-Vernet, M. Moncuquet, K. Issautier, and P. Schippers. Frequency range of dust detection in space with radio and plasma wave receivers: Theory and application to interplanetary nanodust impacts on cassini. Journal of Geophysical Research: Space Physics, 122(1):8–22, 2017. doi: https://doi.org/10.1002/2016JA023081.

A. Mocker, K. Hornung, E. Grün, S. Kempf, A. Collette, K. Drake, M. Horányi, T. Munsat, L. O'Brien, Z. Sternovsky, and R. Srama. On the application of a linear time-of-flight mass spectrometer for the investigation of hypervelocity impacts of micron and sub-micron sized dust particles. Planetary and Space Science, 89:47–57, 2013. ISSN 0032-0633. doi: https://doi.org/10.1016/j.pss.2013.07.013.

G. E. Morfill, E. Grün, and C. Leinert. The interaction of solid particles with the interplanetary medium. In R. G. Marsden, editor, The Sun and the Heliosphere in Three Dimensions, pages 455–474, Dordrecht, 1986. Springer Netherlands. ISBN 978-94-009-4612-5.

F. S. Mozer. Dc and low-frequency double probe electric field measurements in space. Journal of Geophysical Research: Space Physics, 121(11):10,942–10,953, 2016. doi: https://doi.org/10.1002/2016JA022952.

D. Nesvorný, P. Jenniskens, H. F. Levison, W. F. Bottke, D. Vokrouhlický, and M. Gounelle. Cometary origin of the zodiacal cloud and carbonaceous micrometeorites. The Astrophysical Journal, 713(2):816–836, mar 2010. doi: 10.1088/0004-637x/713/2/816.

L. Nouzák, S. Hsu, D. Malaspina, F. Thayer, S.-Y. Ye, J. Pavlů, Z. Němeček, J. Šafránková, and Z. Sternovsky. Laboratory modeling of dust impact detection by the cassini spacecraft. Planetary and Space Science, 156:85–91, 2018. ISSN 0032-0633. doi: https://doi.org/10.1016/j.pss.2017.11.014.

L. Nouzák, Z. Sternovsky, M. Horányi, S. Hsu, J. Pavlů, M.-H. Shen, and S.-Y. Ye. Magnetic field effect on antenna signals induced by dust particle impacts. Journal of Geophysical Research: Space Physics, 125(1):e2019JA027245, 2020. doi: https://doi.org/10.1029/2019JA027245.

P. Oberc. Electric antenna as a dust detector. Advances in Space Research, 17(12):105–110, 1996. ISSN 0273-1177. doi: https://doi.org/10.1016/0273-1177(95)00766-8.

E. O'Shea, Z. Sternovsky, and D. M. Malaspina. Interpreting dust impact signals detected by the stereo spacecraft. Journal of Geophysical Research: Space Physics, 122(12):11,864–11,873, 2017. doi: https://doi.org/10.1002/2017JA024786.

A. Poppe, D. James, B. Jacobsmeyer, and M. Horányi. First results from the venetia burney student dust counter on the new horizons mission. Geophysical Research Letters, 37(11), 2010. doi: https://doi.org/10.1029/2010GL043300.

A. R. Poppe. An improved model for interplanetary dust fluxes in the outer solar system. Icarus, 264:369–386, 2016. ISSN 0019-1035. doi: https://doi.org/10.1016/j.icarus.2015.10.001.

S. Robertson, Z. Sternovsky, and B. Walch. Reduction of asymmetry transport in the annular penning trap. Physics of Plasmas, 11(5):1753–1756, 2004. doi: 10.1063/1.1688337.

M. M. Shen, Z. Sternovsky, M. Horányi, H.-W. Hsu, and D. M. Malaspina. Laboratory study of antenna signals generated by dust impacts on spacecraft. Journal of Geophysical Research: Space Physics, 126(4):e2020JA028965, 2021a. doi: https://doi.org/10.1029/2020JA028965. e2020JA028965 2020JA028965.

M. M. Shen, Z. Sternovsky, A. Garzelli, and D. M. Malaspina. Electrostatic model for antenna signal generation from dust impacts. Earth and Space Science Open Archive, page 38, 2021b. doi: 10.1002/essoar.10507271.1.

A. Shu, A. Collette, K. Drake, E. Grün, M. Horányi, S. Kempf, A. Mocker, T. Munsat, P. Northway, R. Srama, Z. Sternovsky, and E. Thomas. 3 mv hypervelocity dust accelerator at the colorado center for lunar dust and atmospheric studies. Review of Scientific Instruments, 83(7):075108, 2012. doi: 10.1063/1.4732820.

R. Srama, T. J. Ahrens, N. Altobelli, S. Auer, J. Bradley, M. Burton, V. Dikarev, T. Economou, H. Fechtig, M. Gorlich, et al. The cassini cosmic dust analyzer. The Cassini-Huygens Mission, pages 465–518, 2004.

J. Szalay, M. Piquette, and M. Horányi. The student dust counter: Status report at 23 au. Earth, Planets and Space, 65:1145–1149, 2013.

J. R. Szalay and M. Horányi. The search for electrostatically lofted grains above the moon with the lunar dust experiment. Geophysical Research Letters, 42(13):5141–5146, 2015. doi: https://doi.org/10.1002/2015GL064324.

J. R. Szalay and M. Horányi. Lunar meteoritic gardening rate derived from in situ ladee/ldex measurements. Geophysical Research Letters, 43(10):4893–4898, 2016. doi: https://doi.org/10.1002/2016GL069148.

J. R. Szalay, A. R. Poppe, J. Agarwal, D. Britt, I. Belskaya, M. Horányi, T. Nakamura, M. Sachse, and F. Spahn. Dust phenomena relating to airless bodies. Space Science Reviews, 214(5):98, Aug 2018. ISSN 1572-9672. doi: 10.1007/s11214-018-0527-0.

J. R. Szalay, P. Pokorný, S. D. Bale, E. R. Christian, K. Goetz, K. Goodrich, M. E. Hill, M. Kuchner, R. Larsen, D. Malaspina, D. J. McComas, D. Mitchell, B. Page, and N. Schwadron. The near-sun dust environment: Initial observations from parker solar probe. The Astrophysical Journal Supplement Series, 246(2):27, feb 2020. doi: 10.3847/1538-4365/ab50c1.

F. M. Thayer, D. M. Malaspina, A. Collette, and Z. Sternovsky. Variation in relative dust impact charge recollection with antenna to spacecraft potential on stereo. Journal of Geophysical Research: Space Physics, 121(6):4998–5004, 2016. doi: https://doi.org/10.1002/2015JA021983.

R. B. Torbert, C. T. Russell, W. Magnes, R. E. Ergun, P.-A. Lindqvist, O. LeContel, H. Vaith, J. Macri, S. Myers, D. Rau, J. Needell, B. King, M. Granoff, M. Chutter, I. Dors, G. Olsson, Y. V. Khotyaintsev, A. Eriksson, C. A. Kletzing, S. Bounds, B. Anderson, W. Baumjohann, M. Steller, K. Bromund, G. Le, R. Nakamura, R. J. Strangeway, H. K. Leinweber, S. Tucker, J. Westfall, D. Fischer, F. Plaschke, J. Porter, and K. Lappalainen. The fields instrument suite on mms: Scientific objectives, measurements, and data products. Space Science Reviews, 199(1): 105–135, Mar 2016. ISSN 1572-9672. doi: 10.1007/s11214-014-0109-8.

J. Vaverka, T. Nakamura, J. Kero, I. Mann, A. De Spiegeleer, M. Hamrin, C. Norberg, P.-A. Lindqvist, and A. Pellinen-Wannberg. Comparison of dust impact and solitary wave signatures detected by multiple electric field antennas onboard the mms spacecraft. Journal of Geophysical Research: Space Physics, 123(8):6119–6129, 2018. doi: https://doi.org/10.1029/2018JA025380.

J. Vaverka, J. Pavlů, L. Nouzák, J. Šafránková, Z. Němeček, I. Mann, S. Ye, and P.-A. Lindqvist. One-year analysis of dust impact-like events onto the mms spacecraft. Journal of Geophysical Research: Space Physics, 124(11):8179–8190, 2019. doi: https://doi.org/10.1029/2019JA027035.

S.-Y. Ye, D. A. Gurnett, W. S. Kurth, T. F. Averkamp, S. Kempf, H.-W. Hsu, R. Srama, and E. Grün. Properties of dust particles near saturn inferred from voltage pulses induced by dust impacts on cassini spacecraft. Journal of Geophysical Research: Space Physics, 119(8):6294–6312, 2014. doi: https://doi.org/10.1002/2014JA020024.

S.-Y. Ye, D. A. Gurnett, and W. S. Kurth. In-situ measurements of saturn's dusty rings based on dust impact signals detected by cassini rpws. Icarus, 279:51–61, 2016a. ISSN 0019-1035. doi: https://doi.org/10.1016/j.icarus.2016.05.006. Planetary Rings.

S.-Y. Ye, W. S. Kurth, G. B. Hospodarsky, T. F. Averkamp, and D. A. Gurnett. Dust detection in space using the monopole and dipole electric field antennas. Journal of Geophysical Research: Space Physics, 121(12):11,964–11,972, 2016b. doi: https://doi.org/10.1002/2016JA023266.

S.-Y. Ye, W. S. Kurth, G. B. Hospodarsky, A. M. Persoon, A. H. Sulaiman, D. A. Gurnett, M. Morooka, J.-E. Wahlund, H.-W. Hsu, Z. Sternovsky, X. Wang, M. Horanyi, M. Seiß, and R. Srama. Dust observations by the radio and plasma wave science instrument during cassini's grand finale. Geophysical Research Letters, 45(19):10,101–10,109, 2018. doi: https://doi.org/10.1029/2018GL078059.

S.-Y. Ye, J. Vaverka, L. Nouzak, Z. Sternovsky, A. Zaslavsky, J. Pavlu, I. Mann, H.-W. Hsu, T. F. Averkamp, A. H. Sulaiman, D. Pisa, G. B. Hospodarsky, W. S. Kurth, and M. Horanyi.

Understanding cassini rpws antenna signals triggered by dust impacts. Geophysical Research Letters, 46(20):10941–10950, 2019. doi: https://doi.org/10.1029/2019GL084150.

S.-Y. Ye, T. F. Averkamp, W. S. Kurth, M. Brennan, S. Bolton, J. E. P. Connerney, and J. L. Joergensen. Juno waves detection of dust impacts near jupiter. Journal of Geophysical Research: Planets, 125(6):e2019JE006367, 2020. doi: https://doi.org/10.1029/2019JE006367.

A. Zaslavsky. Floating potential perturbations due to micrometeoroid impacts: Theory and application to s/waves data. Journal of Geophysical Research: Space Physics, 120(2):855–867, 2015. doi: https://doi.org/10.1002/2014JA020635.

A. Zaslavsky, N. Meyer-Vernet, I. Mann, A. Czechowski, K. Issautier, G. Le Chat, F. Pantellini, K. Goetz, M. Maksimovic, S. D. Bale, and J. C. Kasper. Interplanetary dust detection by radio antennas: Mass calibration and fluxes measured by stereo/waves. Journal of Geophysical Research: Space Physics, 117(A5), 2012. doi: https://doi.org/10.1029/2011JA017480.

H. A. Zook and O. E. Berg. A source for hyperbolic cosmic dust particles. Planetary and Space Science, 23(1):183–203, 1975. ISSN 0032-0633. doi: https://doi.org/10.1016/0032-0633(75)90078-1.